Spring 2002

Modeling and experimental verification of growth of an axisymmetric cylindrical rod by three-dimensional laser-induced chemical vapor deposition

Qing Chen
Louisiana Tech University

MODELING AND EXPERIMENTAL VERIFICATION OF GROWTH OF AN AXISYMMETRIC CYLINDRICAL ROD BY THREE DIMENSIONAL LASER INDUCED CHEMICAL VAPOR DEPOSITION

by

Qing Chen, M.S.

A Dissertation Presented in Partial Fulfillment
of the Requirements for the Degree
Doctor of Philosophy

COLLEGE OF ENGINEERING AND SCIENCE
LOUISIANA TECH UNIVERSITY

May 2002

ProQuest Information and Learning Company
300 North Zeeb Road
P.O. Box 1346
Ann Arbor, MI 48106-1346

LOUISIANA TECH UNIVERSITY

THE GRADUATE SCHOOL

3/19/2002
Date

We hereby recommend that the dissertation prepared under our supervision by Qing Chen entitled Modeling and Experimental Varification of Growth of an Axisymmetric Cylindrical Rod by Three Dimensional Laser Induced Chemical Vapor Deposition be accepted in partial fulfillment of the requirements for the Degree of Doctor of Philosophy

Raja Nassar
Supervisor of Dissertation Research

Richard L. Greechie
Head of Department

Department

Recommendation concurred in:

Weizhong Dai

A. Ed. Mohamed

Advisory Committee

Approved:
Bala Ramachandran
Director of Graduate Studies

Leslie K. Guice
Dean of the College

Approved:
Terry McConathy
Dean of the Graduate School

GS Form 13
(1/00)

ABSTRACT

Three-dimensional laser-induced chemical vapor deposition (3D-LCVD) is a recently developed micro-manufacturing process that holds great potential for the production of complex microstructures with high aspect ratio. A laser beam is focused through a vacuum chamber window onto a movable substrate. The heat from the laser at or near the focal spot on the substrate induces the decomposition reaction of precursor gas in the chamber. As a result, solid-phase reaction products are deposited on the substrate to form the microstructure. In this dissertation, a numerical model is developed for simulating kinetically-limited growth of an axisymmetric cylindrical rod by pre-specifying the surface temperature distribution required for growing the rod and then by solving for the laser power that satisfies the pre-specified temperature distribution.

The solution using least squares is obtained iteratively by minimizing the sum of square deviations between the pre-specified surface temperature distribution and the calculated temperature distribution from the heat conduction equation with a given laser power as a heat source. The optimum laser power is calculated layer by layer using the above method. Thus the optimum laser power over rod length or growth time can be obtained (to grow a cylindrical rod) from the model.

LCVD experiments were carried out to verify this model. The optimum laser power over time is inputted into the computer which can automatically control laser power during the LCVD process. Experimental results show that rods grown under the

predicted laser power from the numerical model were very close to being cylindrical in shape with a small deviation at the bottom of the rod. The reasons for this deviation are discussed and ways to further improve the model are recommended.

TABLE OF CONTENTS

LIST OF TABLES

LIST OF FIGURES

NOMENCLATURE

a	axis growth between two adjacent layers
A	coefficient matrix of a linear system
A_s	surface area
b	column vector of non-homogeneous terms or a linear system
c	speed of light, or a constant to determine the surface shape of the rod
c_d	heat capacity of deposit
c_s	heat capacity of substrate
D	gas diffusivity
E_a	activation energy
G_r	Grashoff number
h	distance between two adjacent grid points
h_{conv}	convective heat transfer coefficient
h_p	the height of the parabolic portion of the rod
I_o	laser power density
K_o	growth rate constant
k_d	thermal conductivity of deposit material
k_s	thermal conductivity of substrate material
k_{gas}	thermal conductivity of gas species
L	length of the rod
L_1	length of the straight portion of the rod

M the number of grid points on the parabolic portion of the rod, or the number of the parameters in the parameter vector **p**.

n precursor concentration

n(x) unit normal vector

N the number of grid points on the whole surface of the rod

N_u Nusselt number

P_o laser power

P_r Prandtl number

Q_{cond} heat loss rate due to conduction

Q_{conv} heat loss rate due to convection

Q_{in} heat input rate from laser absorption

Q_{rad} heat loss rate due to radiation

Q''_{in} heat flux due to the distributed heat source

Q''_{loss} heat flux due to the distributed heat sink

r_w reaction zone radius

R the radius of the rod, or the universal gas constant

R_n normal deposition rate

R_o axial deposition rate

R_v volumetric deposition rate

s_i slope of the normal line at grid point i

S_e Sum of squared errors

t processing time

T temperature

T_s surface temperature

$\mathbf{T_d}$ column vector containing temperatures distributed on the parabolic portion of the rod, calculated from heat conduct equation

$\mathbf{T_d}^r$ column vector containing temperatures distributed on the parabolic portion of the rod, required for the growth of a cylindrical rod

T_∞ ambient temperature

Δt time interval

ε_s surface emissivity

θ Temperature excess

Λ absorbance

λ wavelength of the laser light

σ Stephan-Boltzman constant

ω_o laser beam width at focus point

ϕ incident angle from the surface normal vector

∇ del operator

ACKNOWLEDGEMENTS

First of all, I would like to thank my family, who always encourage and support me in my studies. I would like to express my gratitude and sincere appreciation to my advisor Dr. Raja Nassar and Dr. Wenzhong Dai, for their excellent guidance and great patience. Without their help, I could not finish my research project at this time.

I would also like to thank Dr. Edwin Alexander, Dr. Zengcheng Zhong and Dr. Boman as my committee members, who helped me throughout my research. I would like to express my special thanks to my former committee member, Dr. James Maxwell, for his excellent advise in LCVD field and for his kindness and financial support which provided me the opportunity to study at Louisiana Tech University. I want to thank my friends and partners, Feng Gao and Yanjun Tang, who helped me run the experiments. I would like to thank Dr. Xu who helped me get the SEM pictures of grown rods at IFM.

Finally, I also want to express my appreciation to Dr. Greechie for his help at the beginning of my studies in this University.

CHAPTER ONE

INTRODUCTION

1.1 Overview of Three-Dimensional LCVD

Three-dimensional Laser induced chemical vapor deposition (3D-LCVD) is a recently developed micro-manufacturing technique for free-form fabrication of high aspect ratio microstructures. Current micro-manufacturing technologies involve three major topics of research, namely Rapid Prototyping, Micro-Electro-Mechanical Systems (MEMS) based applications, and microelectronics based thin film deposition techniques. Rapid prototyping is also known as solid freeform fabrication (SFF). The most successfully developed rapid prototyping techniques are micro-stereo lithography, selective laser sintering, and laminated object manufacturing.

MEMS deals with systems wherein different micro-components are assembled together to make a micro-device. Each component contributes either electrically, mechanically, or chemically to give a fully functional device such as pressure transducers, accelerometers, micro-turbine, and chemical sensors, etc. In short, MEMS refers to a broad class of micro-machined sensors, actuators, and systems that exploit thermal, electrical, mechanical, optical, magnetic, acoustic, and chemical phenomena. Developed processes for MEMS include photolithography, X-ray lithography (LIGA), electro-beam lithography, ion beam lithography, and focused ion beam (FIB). Thin film deposition, as an additive pattern

transfer technique, is an important process in both microelectronics and MEMS fabrication. It can be categorized into two major types, namely, physical vapor deposition (PVD) and chemical vapor deposition (CVD).

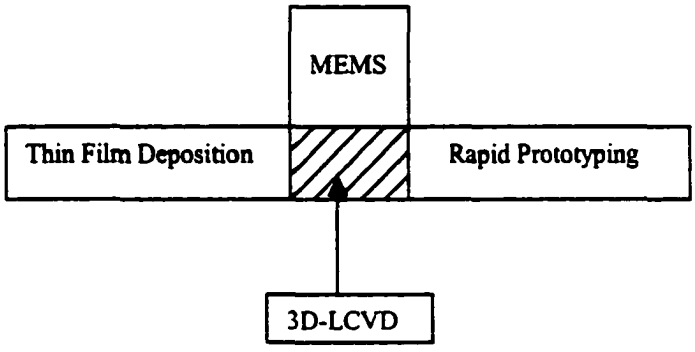

Figure 1-1 Role of 3D-LCVD in micro-manufacturing technologies.

Laser-induced Chemical Vapor Deposition is a technique for depositing a certain material of a certain shape on a substrate by inducing chemical reactions with a laser beam. LCVD can be considered to be an intersection of the above three research fields (Figure 1-1) in its attempt to rapid prototype micro-scale components for MEMS-based applications using thin film deposition techniques. LCVD can generate microstructures with sub-micron resolution by precisely controlling both the temperature at the reaction zone (by adjusting the laser power) and concentration (pressure) of the precursor gas over a surface, thereby generating a solid form of a desired shape and composition using computer control. Through LCVD, material is selectively deposited into useful mechanical forms directly from the vapor phase. LCVD can either be 2-dimensional (2D) or 3-dimensional (3D). 2D LCVD is also called laser direct writing. 3D LCVD is mainly used for prototyping microstructures.

A 3D-LCVD system usually consists of a laser beam as energy source, vacuum chamber, and a moveable target. The laser beam (usually of a Gaussian profile) is focused

through a chamber window onto a substrate target as shown in Figure 1-2. A reactive gas is introduced into the chamber, and it reacts at (or near) the focal spot on the substrate, leaving behind any solid-phase reaction product. The laser induces this decomposition by either thermal- or photo-excitation. Precursors are chosen so that the by-products of the reaction are volatile and easy to return to the surrounding gas mixture.

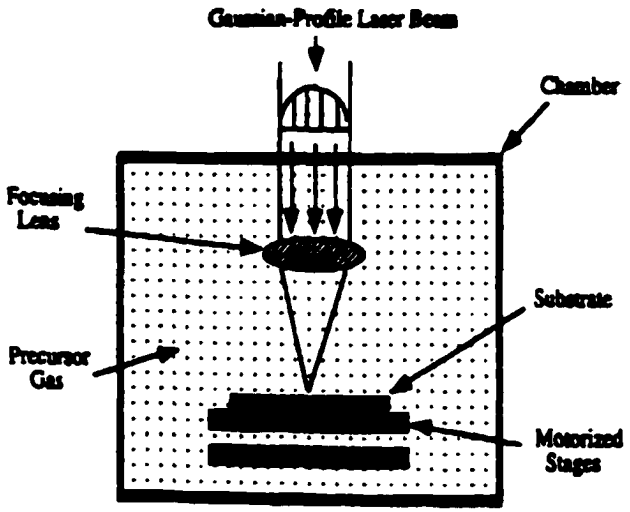

Figure 1-2 A schematic diagram of 3D-LCVD system.

1.2 Three-Dimensional LCVD Applications

Material processing with lasers takes advantage of the characteristics of laser light. The high energy density and directionality achieved with lasers permit localized heat- or photo-treatment of materials with a spatial resolution of better that 1 μm. The mono-chromaticity of laser light allows for control of the depth of heat treatment or for selective, non-thermal excitation – either within the surface of the material or within the molecules of the surrounding medium – simply by changing the laser wavelength. Because laser light is an essentially massless tool, there is no need for mechanical holders with all the problems these

pose in the case of either brittle or soft materials. With lasers, thermal and chemical treatment can be strongly localized, thereby leaving the material otherwise unaffected. Consequently, the laser technique allows one to process heat-sensitive materials such as compound semiconductors, high-temperature superconductors, piezoelectric ceramics, polymers, etc. For instance, in laser-induced CVD heating takes place only locally or not at all. Furthermore, laser processing avoids material damage from ion or electron bombardment.

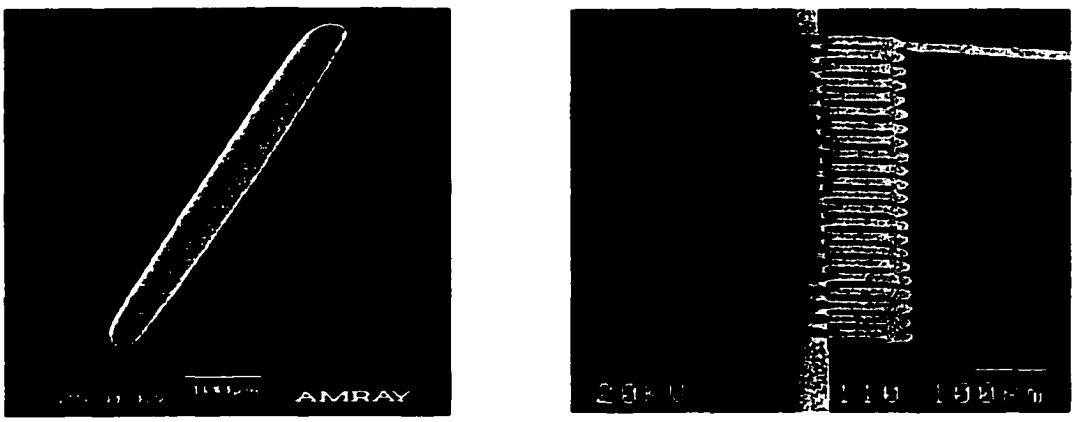

(a). (b).

Figure 1-3 Some applications of 3D-LCVD.

The most common and simple application of 3D-LCVD is fiber growth. Over the last 25 years, various researchers have improved upon this LCVD process. Bauerle[1] and Wallenberger[2] have reported on the growth of Si and C rods. Baum and Comita[3] reported the growth of Au rods. Maxwell[4] investigated the growth of Ni rods. Marcus[5] reported on the growth of Ti and C rods from various precursors, and Boman[6] reported the growth of B rods. Recently, some complex microstructures were grown by three-dimensional LCVD technique. Hanabusa *et al.* have grown micro-lenses[7], Pegna *et al.* are known for there active research in growing trussed structures[8], and micro-wall structures[9]. Helical carbon

fiber coils were also grown by Maxwell, yielding high elastic springs by simultaneously moving and rotating the substrate (Figure 1-3b)[10]. Freestanding conductive coils of polycrystalline tungsten and tungsten carbide were also grown[11], [12]. Figure 1-3a shows a carbon fiber with diameter 50 μm, grown by the author at the Institute for Micromanufacturing (IfM) at Louisiana Tech University.

The most serious limitations of laser processing are the total process rates and throughputs. This severe problem refers not only to laser-direct writing, but also to many cases of large-area laser processing. The local processing rates for deposition, etching, etc., can be extremely high, 100 μm/s and more. Nevertheless, the processed surface area per unit time is quite small. Many of the conventional large-area techniques permit fabrication of a large number of devices simultaneously. In the foreseeable future, laser direct writing of complete complex structures may be interesting for the design of prototypes, but not for mass production.

1.3 LCVD Modeling

Although a number of studies have been done on LCVD, its mechanism is not yet thoroughly understood. This is because of the great difficulty of measuring the temperature on the surface of the deposit during the LCVD process. It is essential to know the temperature distribution induced by the laser radiation in order to identify the type of the reaction mechanism and to be able to explain the morphology and properties of the deposited material and the shape of the deposit. Several methods[1] have been developed to measure, *in situ*, the temperature distribution. All of these methods exhibit lack of reliability because they depend on the emissivity of the irradiated material, which can differ substantially from that

of the unirradiated material. It is therefore useful to calculate the temperature distribution by means of mathematical models.

Modeling has been widely employed when solving applied problems in different branches of technology. In a wide context, modeling implies constructing a model which involves a simplification of the process being modeled.

In mathematical modeling, the analysis of mathematical models of an object complements experimental investigations of properties and characteristics of the object. Currently, computers are widely used for mathematical modeling as well as methods of numerical analysis.

Several authors have proposed analytical models based on Green's function[13], Bessel transforms[14] and Fourier series[15] approximations to the solution of the heat diffusion equation. Generally, analytic solutions can be obtained only for some simple physical problems with simple boundary conditions[16, 17]. For more complicated problems, numerical methods are needed. In the relevant literature, a number of numerical models were proposed to solve this problem. Several studies in the literature are related to numerical simulations of LCVD. Bauerle was the first to suggest LCVD for use in growing mechanical structure[18]. Arnold and Bauerle[19-20] simulated the growth of pyrolytic LCVD in one and two-dimensions assuming a semi-infinite substrate and the model was applied to the deposition of spots and the direct writing of lines. Allen and co-workers[21] used the finite difference method to model the temporal growth of nickel deposits by CO_2 laser pulses. Tonneau and Auvert[22] developed a computer simulation and presented laser induced temperatures in the case of laser direct writing. Leon and Perez-Amor[23] developed models to calculate the temperature distribution in spots as well as in lines by using the finite

difference method to solve the thermal diffusion equation. Weissaman and Hsu[24] used the finite element method to model laser sintered parts. A Monte Carlo technique was applied by Zeiri *et al*[25]. Maxwell[26] presented a mathematical model based on a stationary laser focal spot to predict the transport and thermal phenomena which underlie the 3D-LCVD process. Recently Dai and Nassar *et al*[27] have developed a numerical model for simulating axisymmetric rod growth at a stationary laser focal spot in an LCVD process. By this model a solution for the temperature distribution on the rod was obtained and the shape of the rod grown was predicted based on the temperature distribution. Figure 1-4 shows the simulation for the growth of the rod (in the case of deposition of nickel onto graphite where m is the mesh size) and the actual growth obtained experimentally. Results agreed well with experimental observations.

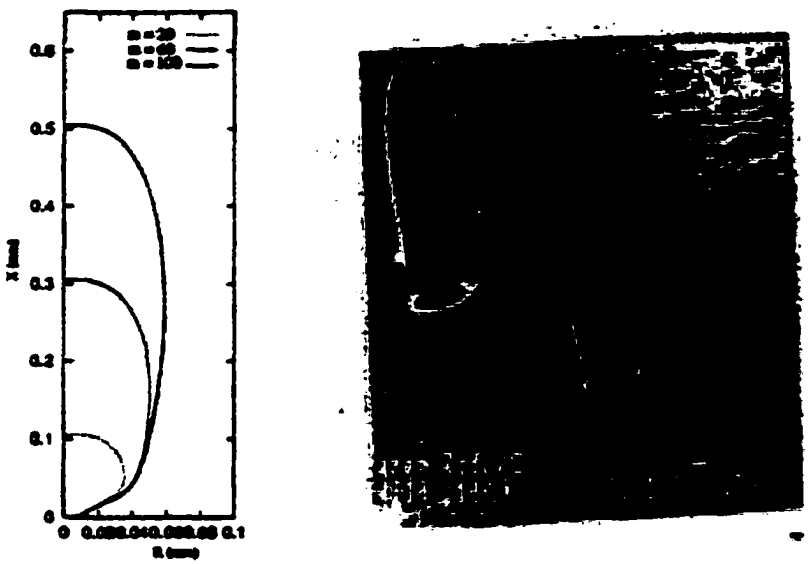

Figure 1-4 Simulation of rod growth (left) as compared to the actual experimental results (right).

1.4 Research Objectives

All the models mentioned above are based on the assumption that during the LCVD process, each process parameter (such as laser power output, laser beam width, surrounding temperature, etc.) is constant over time. As such the temperature distribution induced by the laser was calculated, then the growth and the shape of the rod was determined.

Under this assumption, it is of interest to observe the change in the diameter of the rod as a function of its length. As can be seen from the results in Figures 1-4b and 1-5, the diameter of the rod is rather small at the beginning of growth after which it increases in size until it reaches a fixed size.

Figure 1-5 The shape of the bottom of a rod grown under constant parameters.

This growth pattern can be explained by the fact that at the beginning of growth, the temperature at the surface is not high enough to cause a wide deposit. However, as the rod grows, the rate of heat flow from the tip to the bottom of the rod diminishes, causing an increase in temperature at the tip, which in turn induces an increase in surface deposition and hence an increase in rod diameter. When the process reaches steady state, heat losses (from

convection and radiation) are balanced by heat gains and the temperature profile on the top surface of the rod changes little, so the diameter of the rod remains almost constant. Obviously, the diameter at the bottom of the rod is determined by the conductivities of both substrate and deposit.

This phenomenon leads to the following question: Is one be able to predict LCVD process parameters (such as laser power, beam waist radius, etc.) to grow a rod with a pre-specified shape (such as a cylindrical rod)? An answer to this question is the objective of this dissertation.

It should be pointed out that this problem is an inverse problem because it is from the temperature distribution required for the pre-determined growth that one solves for the process parameters. None of the existing models in the relevant literature can accomplish this inverse project. In this dissertation an axisymmetric numerical model is developed to predict process parameters required to grow a cylindrical rod (ideally, the diameter of the rod remains constant from bottom to tip) by three-dimensional laser-induced chemical vapor deposition and to verify model results with experimental observations.

1.5 Organization of this Dissertation

Chapter one, as an introduction, describes the role of three-dimensional LCVD in the field of micro-manufacturing industry, introduces modeling on LCVD, and states the goals of this dissertation. Chapter two provides the necessary technical background for three-dimensional LCVD. Chapter three describes how to construct a model on direct heat conduction problems (DHCP) for LCVD. Chapter four describes how to construct a model on the inverse heat conduction problem (IHCP) by using least square method. This chapter

gives the solution to IHCP in general case. Chapter five gives an application of the model constructed in chapter four, based on the current experimental conditions. Also this chapter gives the specific solution to grow a cylindrical rod with adjustable laser power and fixed laser beam width. Chapter six is the experimental part of this dissertation. In this chapter, the solution obtained from chapter five is applied to the experiment. Chapter seven compares the experimental results and the results of the calculations from the model and analyzes the deviations of the experimental results from the expected results. The conclusion and future studies for this dissertation are also addressed in this chapter.

CHAPTER TWO

TECHNICAL REVIEW OF THREE-DIMENSIONAL LCVD

This chapter gives a general description of some basic theories of 3D-LCVD. First, laser as an energy source is discussed. Second, the LCVD mechanism is explored. Third, LCVD reaction rates, which can be classified into kinetic limited rate, mass transfer limited rate, and thermodynamic limited rate, is discussed and LCVD process parameters for each of these rates are presented.

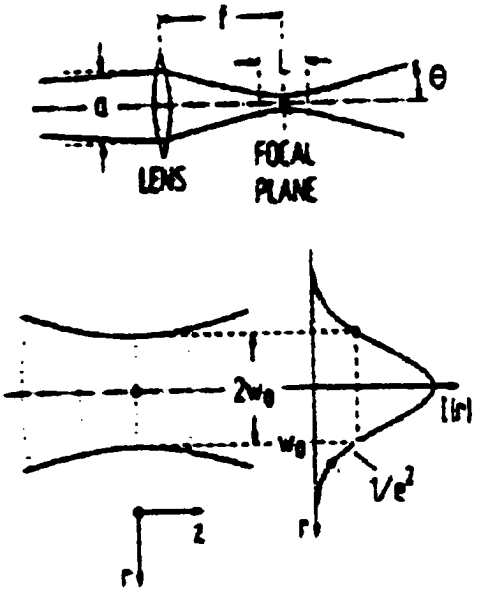

Figure 2.1 Gaussian profile of a laser beam[1].

2.1 Laser Source in Three-Dimensional LCVD

As the sole energy source, laser plays an important role in a 3D-LCVD process. The power delivered to a surface determines the local surface temperature, which in turn determines the growth rate and the shape of the deposit. In this section, the laser power density profile on the focal plane (Figure 2-1), which directly determines the temperature distribution on the surface of the substrate or deposit, is discussed. The wave function for the propagation of electromagnetic waves with time can be expressed as:

$$\nabla^2 U = \frac{1}{c^2}\frac{\partial^2 U}{\partial t^2} \tag{2.1}$$

Where U is a wave function, c is the speed of light, and t is time. If $U(r, t) = U(r)\cdot e^{i\omega t}$ is substituted in Equation (2.1), the Helmholtz equation for the propagation of paraxial waves, such as in a laser beam, is obtained [26].

$$\nabla^2 U(r)_{x,y} - 2i\frac{\omega^2}{c^2}\frac{\partial}{\partial z}U(r) = 0 \tag{2.2}$$

The unimodal solution to this equation for laser beams has the Gaussian form:

$$U(r) \equiv U_0 \frac{\omega_0}{\omega(z)}\left[e^{\frac{r^2}{\omega^2(z)}}\right]\cdot\left[e^{\frac{i\omega^2(z)}{2c^2\Gamma(z)}}\right]\cdot e^{-i\frac{\omega^2(z)z}{c^2}}\cdot e^{i\cdot\arctan\left(\frac{z}{z_0}\right)} \tag{2.3}$$

Where $\omega(z)$ is the $1/e^2$ beam waist radius at any axial position z, ω_0, is the $1/e^2$ spot radius at the focus (z = 0, see Figure 2.1), z_o is the Rayleigh range, and $\Gamma(z)$ is the wavefront radius of curvature. Here,

$$\omega_o \approx \frac{\lambda}{\pi\theta}\ , \tag{2.4}$$

$$z_o = \frac{\pi\omega_o^2}{\lambda}\ , \tag{2.5}$$

$$\omega(z) = \omega_o\left[1+\left(\frac{z}{z_o}\right)^2\right], \tag{2.6}$$

and

$$\Gamma(z) = z\left[1+\left(\frac{z}{z_o}\right)^2\right]. \tag{2.7}$$

Where θ is the convergence angle of the focused beam, and λ is the laser wavelength. Taking the time average of $U(r)$, i.e. $|U(r)|^2$, the spatially-dependent intensity of a laser beam can be defined as:

$$I(r,z) = I_o\left[\frac{\omega_o}{\omega(z)}\right]^2\left[e^{\frac{2r^2}{\omega^2(z)}}\right], \tag{2.8}$$

where $I_o = |U_o|^2$ is the peak beam intensity. In terms of the average laser power, P_o, the peak intensity becomes:

$$I_o = \frac{2P_o}{\pi\omega_o^2} \tag{2.9}$$

The spatially-dependent intensity at the focal plane can be written as:

$$I(r,0) = \frac{2P_o}{\pi\omega_o^2}\left[e^{\frac{2r^2}{\omega_o^2}}\right] \tag{2.10}$$

Integrating over r, the power delivered to a surface at the focal plane within a circle of radius r is:

$$P(r,0) = P_o\left[1-e^{\frac{2r^2}{\omega_o^2}}\right]. \tag{2.11}$$

Equation (2.10) is important and will be used in the numerical model to calculate the power intensity of each grid point on the focal plane.

2.2 LCVD Mechanisms

As mentioned in the first chapter, LCVD is a technique for depositing various materials on a substrate by inducing chemical reactions using a laser beam. LCVD is carried out through these following mechanisms: photolytic dissociation of the precursor, pyrolytic (thermal) dissociation of the precursor, or a combination of both.

Photolytic LCVD relies on the interactions of the laser beam with chemical reactants. The precursor molecules absorb the photons of the laser beam, which in the visible UV-region cause chemical bonds to break leading to the formation of highly reactive species. These species react in the gas phase and/or on the substrate surface where they form the deposit. Usually visible and UV lasers are used for photolytic LCVD because the photon energy is comparable to, or exceeds, the chemical bond energy of many chemical compounds.

In pyrolytic LCVD, on the other hand, the laser beam interacts mainly with the substrate to produce a hot spot where thermally assisted chemical reactions take place, resulting in the final product. The precursor is selected in such a way that chemical reactions occur at a temperature below the melting temperature of the deposit or the substrate. The precursor gas should be transparent to the incident laser beam in order to prevent absorption of the laser light. In this research, only pyrolytic LCVD is considered with the assumption that the energy from the laser beam is totally absorbed by the substrate (or deposit).

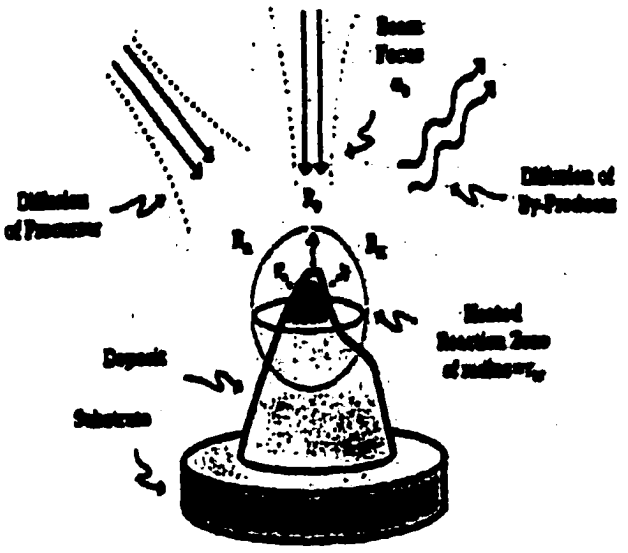

Figure 2-2 A sketch of pyrolytic growth of 3D-LCVD[26].

A typical pyrolytic LCVD process is shown in Figure 2-2, where a heated reaction zone, of radius, r_w is generated by an incident laser beam of waist radius, ω_o, focused at the substrate. The pyrolytic reaction occurs at the surface only within this reaction zone. Outside of this region, the surface temperature is assumed to be below the threshold temperature for deposition. The local deposition rate at each surface point is determined by the activation energy of the precursor deposition reaction and the local temperature at the reaction surface. The magnitude of this growth rate is known as the normal or local deposition rate R_n. Following the reaction, the by-product gases desorb from the growth surface and diffuse into the ambient medium.

2.3 LCVD Deposition Rates

In order to control the shape of the deposit, the deposition rate must be controlled during the LCVD process. Therefore, determination of the deposition rate is of utmost importance in evaluating the feasibility of any LCVD process. While the deposition rate of a pyrolytic reaction is driven by the surface temperature, the rate obtained depends on the reaction activation energy and the ability of the precursor reactants and by-products to transport to and from the surface. When the reaction rate is limited by the activation energy and surface temperature, the process is in the kinetically limited state or phase. When the reaction rate is limited by the precursor gas pressure and by-product diffusion, the process is in the mass transport limited phase. On the other hand, when the reaction rate is limited by the desorption of the precursor (or its intermediates), the process is in the thermodynamically limited phase. In this research, only kinetically limited deposition rate is considered.

2.3.1 Kinetically Limited Rates

Usually a process is kinetically limited at low temperatures and pressures. In this case, the reaction rate rises exponentially with an increase in temperature. The local deposition rate, R_n, can be expressed by the Arrhenius equation[17]:

$$R_n = K_o(p,T)\cdot e^{-\frac{Ea}{RT}} \tag{2.12}$$

Where K_o is a concentration-dependant rate constant, p is the pressure, T is the local surface temperature, and E_a and R are the activation energy and the Universal Gas Constant, respectively.

2.3.2 Mass Transport Limited Rates

For a pyrolytic LCVD, as the deposition rate becomes rapid and the relative conversion of reactants becomes large, the ability of the precursor to arrive at the surface of the reaction zone becomes insufficient to support the continued exponential increase with temperature, and the deposition rate levels off[26]. At this point, the process goes into the mass transport limited phase. In this phase, the deposition rate no longer depends on the Arrhenius equation, but rather on the precursor concentration, n, which is given by the diffusion equation:

$$D\nabla^2 n - \frac{\partial n}{\partial t} = 0, \tag{2.13}$$

where D is the diffusivity of the precursor gas, n is the concentration of the precursor gas, t is time. The solution to this partial differential equation depends on the geometry of the deposit and on the diffusivity D of the precursor gas.

2.3.3 Thermodynamically Limited Rates

For exothermic reactions at high temperatures, the free energy of the reaction becomes less negative with temperature, thereby slowing the deposition rate. This situation gives rise to the thermodynamically-limited phase. At high deposition temperature and low flow rate of the reaction gas mixture, the CVD reaction may rarely be limited by thermodynamics. This implies that all chemicals that have entered the reactor react directly to form the deposit. For instance, if the flow is doubled, the deposition rate will double. The deposition yield, or the fraction of the gas that reacts, is determined by the thermodynamics of the reaction. A process can become

thermodynamically limited as a result of an increase in the apparent activation energy due to greater desorption of the precursor with temperature, i.e. the precursor desorbs before it can react. In this case, the reaction rate can be described by the Langmuir-Hinshelwood equation.

$$R_n = \left(K_o p^2 e^{-\Delta Ea/RT}\right) \Big/ \left(K_{des} \cdot e^{-\Delta H_{des}/RT} + p\right)^2 \qquad (2.14)$$

where K_{des} and H_{des} are the rate constant and enthalpies of desorption, respectively, and p is pressure.

2.4 Expressions of Deposition Rates

For different situations, the deposition rate can be expressed by a local deposition rate, an axial deposition rate, or a volumetric deposition rate. The local deposition rate, R_n, is strictly defined as the magnitude of the rate at any given point on the growth surface, and the vector R_n lies along the normal to said surface. An axial deposition rate, R_o, is R_n along the laser beam axis, which is the maximum growth rate at the center of the beam. An axial deposition rate is a good measure of the chemical reactivity of the precursor used (if in the kinetically limited phase). The volumetric deposition rate takes into account the overall three-dimensional volumetric growth of the deposit. It is a measurement of the feasibility for growing microstructures in a reasonable time period.

Table 2-1 Classification of process parameters in 3D-LCVD[28].

<table>
<tr><th colspan="3">HEAT TRANSFER</th></tr>
<tr><td><u>Beam Conditions</u>
• Spot geometry
• Laser power
• Laser intensity profile
• Wavelength</td><td><u>Surface Properties</u>
• Optical absorption
• Reflectivity
• Emissivity
• Material thermal conductivities,
Surface geometry</td><td><u>Fluid Conditions</u>
• Nusselt number
• Reynold number
• Grashoff number
• Prantl number
• Thermal conductivities</td></tr>
<tr><th colspan="3">MASS TRANSPORT</th></tr>
<tr><td><u>Diffusion-Limited</u>
• Gas diffusivities
• Concentrations
• Size of reaction zone
• Gas temperature</td><td><u>Convection-Limited</u>
• Sherwood number
• Schmidt number
• Reynold number
• concentrations</td><td><u>Surface-Limited</u>
• Adsorption
• Nucleation</td></tr>
<tr><th colspan="3">CHEMISTRY</th></tr>
<tr><td colspan="3"><u>Thermodynamics</u>
Activation energy, E_a
Rate constant, K_o</td></tr>
</table>

2.5 LCVD Process Parameters

LCVD deposition rates are affected by various parameters, such as laser power, laser beam waist, vapor pressure of the precursor gas, local temperature, and the properties of substrate and deposit, etc. process. Table 2.1 (Maxwell, 1996) gives an outline of the key parameters that affect the LCVD process. Some of the important parameters are discussed below:

Laser power profile: The intensity distribution of a laser beam can vary spatially and temporally. These spatial and temporal variations in laser power determine the total amount of energy input in LCVD. For a Gaussian beam, the laser power varies radially. On the other hand, for a top hat beam (uniform beam distribution) the power remains unchanged along the radius of the laser beam.

Laser beam width (diameter): The laser beam width is usually defined as twice the radius of the beam where the power has dropped to $1/e^2$ of the power at the beam center. The beam width affects the laser intensity, or laser power density, which determines the heat flux to the substrate or deposit.

Laser wavelength: The absorption of laser light on the substrate surface and/or in the gas phase is to a large extent dependent on the wavelength. This means that the choice of wavelength will determine whether the process will be thermal or photolytic. The laser wavelength affects the reflectivity on the substrate surface and hence the fraction of the input laser energy utilized in the LCVD process, which in turn defines the laser-induced temperature. The laser wavelength also affects the size of beam waist ω_o on the focal plane, which is very important in numerical modeling.

Partial pressure of precursor gas or reactant concentration: The concentrations of the reactants usually influence the chemical reaction rate, which, in turn, affects the deposition rate. As the concentration increases, the collisions between molecules will increase, and more molecules will reach the activated state to eventually undergo chemical reaction. However, at high partial pressure, the complete adsorption to other atoms/molecules may lower the reaction rate.

Activation energy of decomposition of the precursor, E_a: This parameter directly determines the rate of rod growth and the threshold growth temperature.

Physicochemical properties of the reactants: These properties affect the laser induced heating of the reactants and determine whether the LCVD process will involve photolytic or thermal reactions for a given laser wavelength.

Thermophysical properties of the substrate: These properties control the flow of laser energy in the substrate and the temperature and size of the localized hot spot on the substrate surface.

CHAPTER THREE

MODELLING OF DIRECT HEAT CONDUCTION PROBLEM FOR THREE -DIMENSIONAL LCVD

In this work, models of 3D-LCVD are classified into two categories: direct heat conduction problems and inverse heat conduction problems. Direct heat conduction problems (DHCP) are concerned with the determination of the temperature-distribution in the interior of the solid when the boundary and initial conditions, the energy generation rate (such as laser power), and thermo-physical properties of the medium are specified. In contrast, inverse heat conduction problems (IHCP) are concerned with the determination of boundary condition, energy-generation rate, or thermo-physical properties by utilizing the measured (or estimated) temperature distribution at different locations (grid points) in the solid (substrate or deposit). In this chapter, the physical description of heat flow during 3D-LCVD will be introduced first, then a model of the direct heat conduction problem (DHCP) will be presented in detail. A model for the inverse heat conduction problem (IHCP) will be addressed in the next chapter.

3.1 Physical Description of Heat Flow in a Three-Dimensional LCVD Process

A physical description of heat flow in 3D-LCVD can be schematically expressed as in Figure 3-1. It is seen that within the reaction chamber there are four types of energy

dissociation: laser power, radiation, convection, and conduction. The laser beam incident on top of the deposit, and the heat absorbed at the deposit surface drive the reaction. On

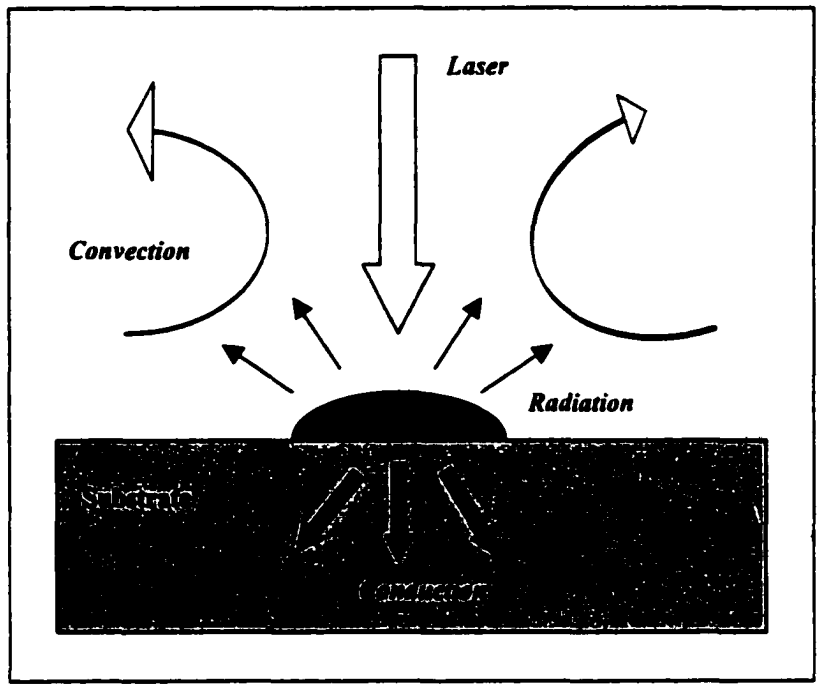

Figure 3-1 Energy source, conductive, radiative and convective heat losses[29].

the other hand, radiation, convection and conduction to the substrate contribute to heat losses. The balance of heat flow into and out of a deposit determines the surface temperature and hence the growth rate, which in turn determines the shape of the deposit.

3.1.1 Heat Conduction

Conduction is the transfer of energy on a molecular scale independent of net bulk flow of the material. For example, in a solid the molecules are held in a more or less rigid structure, so that there is no large amount of molecular translation from point to point. However, molecules vibrate as long as they have a significant amount of thermal energy.

These vibrations increase in amplitude with an increase in the thermal energy level. One of the ways in which heat conduction takes place is through transmission of vibrations from one layer of molecules to an adjacent layer of molecules which are at a lower thermal energy level. Another mechanism of heat conduction on a molecular level involves the so-called free electrons which are more abundant in metals than in other substances. These "free" electrons are very loosely bound to atoms and are therefore relatively free to move about in the solid. Sometimes these electrons are referred to as the "electron gas." Electrons are excellent carriers of both thermal energy and electrical energy and, therefore, substances which have large numbers of free electrons (such as silver or aluminum) are good conductors of heat as well as good conductors of electricity.

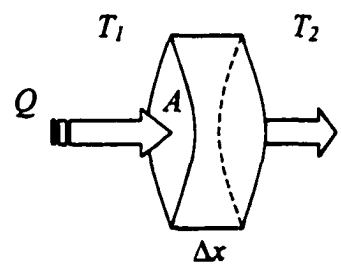

Figure 3-2 Heat transfer rate is proportional to the temperature gradient and the area.

Heat conduction in a medium is governed by **Fourier's Conduction Law**. Expression (3.1) provides the rate of heat flow across an area in a perpendicular direction in terms of the temperature gradient in that direction[30].

$$Q/\Delta t = kA(\Delta T/\Delta x), \tag{3.1}$$

where k is the thermal conductivity of the object.

In an LCVD process, heat conduction goes through two states: conduction from deposit to substrate at the initial stage of growth and conduction from one deposit layer to another. During the initial stages of rod growth, heat conduction to the substrate is the dominant mode because the deposit surface is small. Conduction to the substrate diminishes as the length of the rod increases (rod tip and the heat source become further removed from the substrate). As a result, conductivity of the substrate is a crucial factor in determining the growth rate and shape of the rod. However, when the rod grows long enough, the property of the substrate is no longer important.

3.1.2 Convection

Convection is the transfer of energy from place to place through bulk flow of matter from hotter to colder regions. Thermal energy is carried by the matter rather than being transmitted by it. Convection usually results from thermal gradients or concentration gradients. The rate at which heat is convected from a solid body into a surrounding medium can be described as:

$$Q_{conv} = A_s h_{conv}(T_s - T_\infty) \tag{3.2}$$

Where A_s is the surface area of a heated body, h_{conv} is the heat transfer coeffcient, and T_s T_∞ are the body surface temperature, and ambient temperature, respectively. The heat transfer coefficient, h_{conv}, can be determined from the dimensionless *Nusselt number*, *Nu*, and the thermal conductivity, k_{gas} , of the dominant gas species using the relation:

$$h_{conv} = Nu\frac{k_{gas}}{2r_s} \tag{3.3}$$

The Nusselt number represents the ratio of convection to conduction losses. The

length scale over which convection may develop is the rod diameter, $2r_s$. *Nu* is an empirical expression which depends on the dimensionless *Grashoff* and *Prandtl* numbers, *Gr* and *Pr*. The Grashoff number, *Gr*, is a measure of the ratio of buoyancy to viscous forces in the precursor gas. The Prandtl number, *Pr*, is the ratio of the kinematic viscosity to the thermal diffusivity. In general, for a given body geometry, the Nusselt number can be expressed as:

$$Nu = C + f(Gr, Pr) \tag{3.4}$$

Where C is a constant which depends on the body geometry. When natural convection occurs over a solid horizontal cylinder of uniform temperature, the Nusselt number can be expressed as[31]:

$$Nu = \{0.60 + \frac{0.387(Gr \cdot \mathrm{Pr})^{1/6}}{[1 + (0.599/\mathrm{Pr})^{9/16}]^{8/27}}\}^2 \tag{3.5}$$

for small Grashoff number,

$$Nu_{cylinder} \approx 0.36 \tag{3.6}$$

3.1.3 Radiation

Radiation is the transfer of energy by the emission and subsequent absorption of electromagnetic radiation. Radiation from a blackbody surface into a medium of refractive index, n_i, can be described by Planck's distribution, which gives the spectral emission vs. wavelength, λ, and surface temperature, T_s:

$$Q''_{rad}(\lambda, T_s) = \frac{2\pi \cdot n_i^2 hc}{\lambda^5 (e^{(hc)/(\lambda T_s)} - 1)} \tag{3.7}$$

Where, h is Planck's constant, and c is the speed of light in a vacuum. Integrating this equation over all wavelengths, one arrives at the Stephan-Boltzman equation for hemispherical total emissive power:

$$Q_{rad}^{\cdot}(T_s) = \varepsilon_s n_i^2 \sigma \cdot T_s^4 \tag{3.8}$$

Where, σ is the Stephan-Boltzman constant, ε_s is the emissivity of the deposit.

3.2 Modeling of Direct Heat Conduction Problems in 3D-LCVD

3.2.1 Governing Equations for 3D-LCVD

The governing equations that describe the heat flow through the deposit and substrate are the heat conduction equations[27]:

$$c_d \rho_d \frac{\partial T_d}{\partial t} = \nabla(k_d \nabla T_d) + Q_{in} - Q_{loss} \tag{3.9}$$

and

$$c_s \rho_s \frac{\partial T_s}{\partial t} = \nabla(k_s \nabla T_s) \tag{3.10}$$

Where T_d and T_s are the temperatures of the deposit and substrate, respectively. Q_{in} and Q_{loss} are distributed heat sources at or within the deposit boundaries (such as absorption of the laser light, or convective/radiative losses at the deposit surface). c_d, c_s, ρ_d, ρ_s, k_d and k_s are the specific heats, mass densities, and conductivities of the deposit and substrate, respectively. The interfacial equations between the deposit and substrate are

$$T_d = T_s, \quad k_d \frac{\partial T_d}{\partial n} = k_s \frac{\partial T_s}{\partial n} \tag{3.11}$$

For kinetically limited growth, the magnitude of the normal growth vector $\boldsymbol{R}_n$ may

be expressed by the Arrhenius relation as follows:

$$R_n = (K_0 e^{-E_a/RT_d})\,\mathbf{n} \tag{3.12}$$

Where K_0 is a concentration-dependent rate constant, T_d is the surface temperature of the deposit, and E_a and R are the activation energy and the universal gas constant, respectively. Here, $\mathbf{n}$ is the unit outward normal vector on the instantaneous surface of deposit.

3.2.2 Mathematical Model for an Axisymmetric Rod Growth

We will simplify the above governing equations and develop a mathematical model for simulating an axisymmetric rod growth. We consider an axisymmetric rod deposit as shown in Figure 3-3. The instantaneous surface of the deposit is defined by the vector function $\mathbf{R}(x, r, t)$, and the surface unit normal at each point is given by $\hat{n}(x, r, t)$, where x and r are the coordinates and t is time. If the radius of the surface r can be expressed as a single-valued function of x, i.e., $r(x)$, so that $\mathbf{R}(x, r, t) \rightarrow \mathbf{R}(x, t)$, etc.,

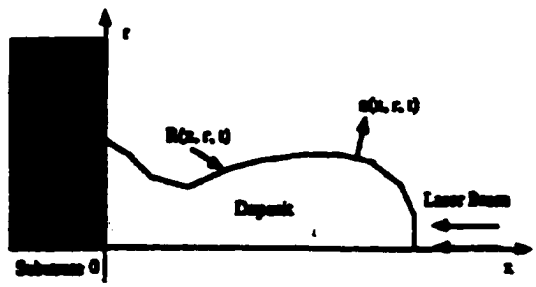

Figure 3-3 An axisymmetric rod.

then in this coordinate system, the instantaneous deposit surface and the unit normal vector at each point may be described by the vectors:

$$\mathbf{R}(x,t) = x(t)\cdot\hat{x} + r(x,t)\cdot\hat{r} \tag{3.13}$$

and

$$\hat{n}(x,t) = -\frac{1}{\psi}\left(\frac{dr(x,t)}{dx}\right)\cdot\hat{x} + \frac{1}{\psi}\cdot\hat{r}, \qquad \psi = \sqrt{1+\left(\frac{dr(x,t)}{dx}\right)^2} \tag{3.14}$$

If the temperature is expressed as $T_d(x,r(x),t)$ or simply, $T_d(x,t)$, then Equation (3.12) becomes

$$\mathbf{R}_n(x,t) = K_0 e^{-Ea/(RT_d)}\left[-\frac{1}{\psi}\left(\frac{dr(x,t)}{dx}\right)\cdot\hat{x} + \frac{1}{\psi}\cdot\hat{r}\right] \tag{3.15}$$

To solve for the shape of any axisymmetric deposit, the temperature profile along the deposit length $T_d(x,t)$ must be known. In principle, the temperature $T_d(x,t)$ can be obtained by solving Equations (3.9) and (3.10). However, we may simplify the equations further if we assume that (1) the heat flux into and out of the deposit is in equilibrium and the temperature distribution over the deposit is at steady state; (2) material properties are constants; and (3) the temperature gradient is largely one-dimensional along the axial x coordinate. Let γ be the deposit volume per unit surface area; then the heat sources and sinks, Q_{in} and Q_{loss}, are related to the heat fluxes, $Q_{in}^{"}$ and $Q_{loss}^{"}$, by $Q = Q^{"}/\gamma$. Given that the shape of the axisymmetric deposit is defined by *r(x)*, Equation (3.9) becomes

$$k_d \frac{d}{dx}\left(\pi r^2(x)\frac{d\theta}{dx}\right) + 2\pi r(x)Q_{in}^{"} - 2\pi r(x)Q_{loss}^{"} = 0 \tag{3.16}$$

where $\theta = T_d - T_\infty$, T_∞ is the surrounding temperature. For a Gaussian beam absorbed completely at a rod tip, and simultaneous convection and radiation from the rod surface, $Q_{in}^{"}$ and $Q_{loss}^{"}$ can be expressed as follows:

$$Q_{in}^{"}(x,r) = 2P_0 \frac{\Lambda}{\pi\omega^2(x-z)} e^{-2r^2/\omega^2(z)}\left[\hat{x}\cdot\hat{n}(x)\right] \tag{3.17}$$

and

$$Q_{loss}^{"}(x,r) = h_{conv}\theta + \varepsilon_s\sigma\theta^4, \tag{3.18}$$

where P_0 is the laser intensity, $\omega(z)$ is the laser beam waist radius at any axial position z, Λ is the absorption coefficient, z is the focal position relative to the rod tip, the term $h_{conv}\theta$ represents the energy loss due to convection, h_{conv} is the heat transfer coefficient, and the term $\varepsilon_s\sigma\theta^4$ represents the energy loss due to radiation.

The laser input flux may be treated as a boundary condition at the rod tip. Assuming that heat conduction within the rod averages the spatial dependence of the input power, the boundary condition for a flat rod tip may be expressed as:

$$\frac{d\theta}{dx} = \frac{1}{\pi r^2 k_d}(\lambda P_0 - h_{conv}\theta) \tag{3.19}$$

When x is at the tip, where for constant beam radius ω, $\lambda = 2\Lambda/\pi\omega^2$.

Conduction to the substrate at the base of the rod is represented by the boundary condition:

$$\frac{d\theta}{dx} = \frac{1}{\pi r^2 k_d} Q_{cond} \tag{3.20}$$

where x is at the base of the rod. The power passing into the substrate Q_{cond}, generates an average temperature T_b at the interface between the rod and the substrate. Carslaw and Jaeger[32] derived a solution to the problem of a uniformly heated circular disc on a semi-infinite solid. They expressed the average base temperature of the heat flow through such a disc as:

$$\theta = \frac{8r}{3\pi k_s} Q_{cond} \tag{3.21}$$

Hence the boundary condition in Equation (3.20) becomes:

$$\frac{d\theta}{dx} = \frac{3k_s\theta}{8k_d r^3} \tag{3.22}$$

If only kinetically limited reactions are considers and diffusion is ignored, K_0 in Equation (3.15) may be treated as a constant. Hence Equations (3.14)-(3.19) and (3.22), coupled with Equations (3.13)-(3.15), may be used to solve iteratively for the shape of an axisymmetric deposit over time.

3.2.3 Numerical Model

To develop a numerical model for simulating an axisymmetric rod growth based on the above mathematical model, one can consider a mesh on the current surface, **R**(x, r), of the rod, as shown in Figure 3-4. The grid points (x_i , r_i), i = 1, 2, ..., N+1, are

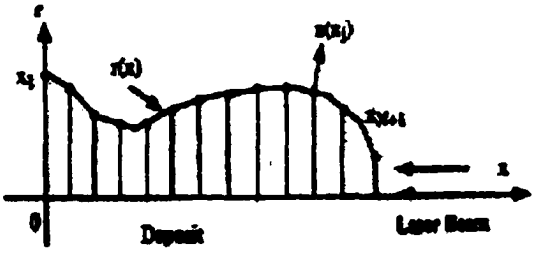

Figure 3-4 Mesh for the current surface of an axisymmetric rod[27].

chosen to be equidistant grid points in the x direction, i.e., $h = x_i - x_{i-1}$, with $x_1 = 0$ and x_{N+1} is at the tip of the rod. If the radiation term in Equation (3.18) is ignored, Eq. (3.16) can be discretized as follows:

$$-\frac{k_d r_{i-1/2}^2}{h^2}\theta_{i-1}+\frac{k_d(r_{i-1/2}^2+r_{i+1/2}^2)}{h^2}\theta_i-\frac{k_d r_{i+1/2}^2}{h^2}\theta_{i+1}=r_i[h_{conv}\theta_i-Q_{in}^*(x_i)] \tag{3.23}$$

where $i=2, 3,\ldots, N$, and

$$Q_{in}^*(x_i)=2P_o(\Lambda/\pi\omega^2)e^{-2r_i^2/\omega^2}[\hat{x}\cdot\hat{n}(x_i)] \tag{3.24}$$

The boundary conditions Equations (3.19) and (3.22) are discretized to be:

$$\frac{\theta_{N+1}-\theta_N}{h}=\frac{\lambda P_o-h_{conv}\theta_{N+1}}{\pi k_d r_{N+1}^2} \tag{3.25}$$

and

$$\frac{\theta_2-\theta_1}{h}=\frac{3k_s\theta_1}{8k_d r_1^3} \tag{3.26}$$

respectively. The unit normal vector $\mathbf{n}(x)$ in Equation (3.14) is discretized to be:

$$\hat{n}(x_i)=-\frac{1}{\psi}\left(\frac{r_{i+1}-r_i}{2h}\right)\cdot\hat{x}+\frac{1}{\psi}\cdot\hat{r},\qquad \psi_i=\sqrt{1+\left(\frac{r_{i+1}-r_i}{2h}\right)^2} \tag{3.27}$$

One can solve Equations (3.23) – (3.26) to obtain the temperature distribution on the rod with a constant laser power P_o and beam width ω. Once the surface temperature corresponding to each grid point $(T_d)_i$ is obtained, one may calculate the new growth of the rod in a small time increment Δt using Equation (3.15) as follow:

$$x_{N+1}^{new}=x_{N+1}+K_o e^{-E_a/R(T_d)_{N+1}}\Delta t,\qquad r_{N+1}^{new}=r_{N+1} \tag{3.28a}$$

$$x_1^{new}=x_1+K_o e^{-E_a/R(T_d)_1}\Delta t,\qquad r_1^{new}=r_1 \tag{3.28b}$$

$$x_i^{new}=x_i+K_o e^{-E_a/R(T_d)_i}\Delta t\frac{1}{\psi_i}\left(\frac{r_{i+1}-r_{i-1}}{2h}\right),\qquad i=2,\ldots,N \tag{3.28c}$$

$$r_i^{new}=r_i+K_o e^{-E_a/R(T_d)_i}\Delta t\frac{1}{\psi_i}$$

3.2.4 Algorithm to Solve DHCP

Finally, a numerical procedure for predicting axisymmetric rod growth can be written as follows[27]:

Step 1: Choose an initial surface. The initial surface could be arbitrary, but its height should be very small. Then choose $N+1$ equidistant grid points (x_i, r_i), with $x_1 = 0$ and x_{N+1} at the tip of the rod. Let m be the iterative number and set $m = 1$.

Step 2: Solve θ_i, using Equations (3.23)-(3.26), then calculate $(T_d)_i = \theta_i + T_\infty$.

Step 3: Assume that the tip of the rod grows Δx along the axial direction. The time increment is then calculated using

$$\Delta t = \frac{\Delta x}{K_o e^{-E_a / R(T_d)_{N+1}}} \quad . \tag{3.29}$$

Thus, the new growth of the current grid points can be obtained using Equations (3.28a)-(3.28c). Furthermore, the new surface of the rod is then approximated by a piecewise linear interpolation.

Step 4: Update $m = m+1$ and $N = mN$. Then determine the new equidistant grid points and repeat steps 2 to 4.

Thus, under constant laser power and constant beam waist (referred to as a direct heat conducted problem, DHCP), the model for axisymmetric rod growth can be constructed layer by layer through the above procedures. The distance between two adjacent layers at the center of the rod is Δx. Results from this model as shown in Figure 1-4 and Figure 3-5 (the rod in this figure was grown by the author) agree well with the experimental results. However, the objective in this work, as stated in chapter one, is to predict process parameters, such as laser power P_o or beam waist radius ω in order to

grow a rod with a desired shape, i.e., a straight rod. As mentioned in the beginning of this chapter, this is an inverse heat conducted problem (IHCP). Another mathematical model for IHCP, which is based on the DHCP model, is addressed in the next chapter.

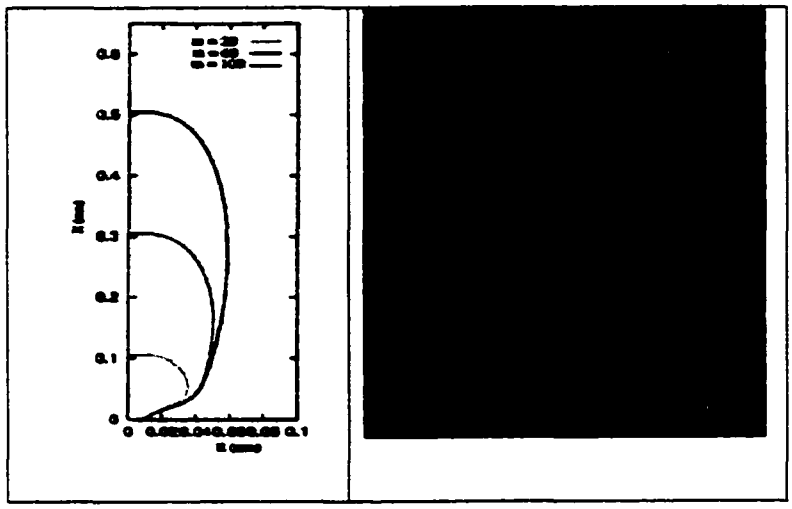

Figure 3-5 Numerical and experimental results from modeling for DHCP.

CHAPTER FOUR

MODELING OF THE INVERSE HEAT CONDUCTION PROBLEM FOR THREE DIMENSIONA LCVD

4.1 Inverse Heat Conduction Problems (IHCP)

As stated in chapter one, to achieve the objective of this work, IHCP technique must be employed. Inverse heat conduction problems are concerned with the determination of boundary conditions, energy-generation rates, or thermo-physical properties by utilizing the measured or estimated temperature history at one or more locations in the solid. Inverse problems are encountered in various branches of science and engineering. Mechanical, aerospace and chemical engineers, mathematicians, astrophysicists, geophysicists, statisticians and specialists of many other disciplines are all interested in inverse problems. In the field of heat transfer, the use of inverse analysis has been applied for estimation of surface conditions such as temperature and heat flux, or the determination of thermal properties such as thermal conductivity and heat capacity of solids by utilizing the transient temperature measurements taken within the medium.

Solutions for inverse heat conduction problems can be classified into function estimation and parameter estimation. If the problem involves the determination of an unknown function, such as the timewise variation of surface heat flux with no prior knowledge of the functional form of the unknown quantity, the problem is referred to as a

problem of function estimation. Function estimation is referred to as an infinite dimensional minimization problem. On the other hand, if some prior knowledge is available on the functional form, it can be parameterized and the inverse problem is called a problem of parameter estimation because only a limited number of parameters are to be estimated. In the idea case, it would be sufficient to have the number of temperature data (the number of grid points) equal to the number of unknown parameters to solve the inverse problem. However, more temperature measurements are needed than the number of unknown to correct the measurement errors. Thus, the system of equations to be solved becomes over-determined. One way of solving a system of over-determined equations is the use of the traditional least-squares approach coupled to an appropriate minimization procedure. In this work, a few number of parameters will be calculated based on the fact that the geometry of the deposit is pre-specified, which means the temperature distribution is pre-specified. Thus this work deals with parameter estimation.

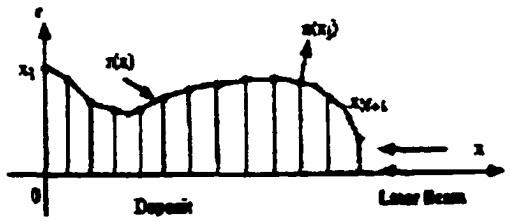

Figure 4-1 Mesh for an inverse heat conduction problem.

4.2 Transformation from IHCP to a Least Squares Problem

The inverse problem as stated above is mathematically ill-posed in a sense that its existence, uniqueness, and/or stability is not yet ensured [33, 34]. A successful solution of an inverse problem generally involves the transformation of the inverse problem into a

well posed-approximate -solution. A variety of techniques are used to achieve this goal [35-37]. In this work, the inverse problem is transformed to a least squares problem. The existence of the inverse solution is guaranteed by requiring that the inverse solution minimized the least squares norm. To demonstrate this method, a problem is presented as in Figure 4-1 (same as Figure 3-4). Suppose there are M unknown parameters affecting the temperature distribution on the surface of the deposit in the figure. The M unknown parameters can be expressed as a parameter vector $\mathbf{p}$, $\mathbf{p} = \{ p_1, p_2, ..., p_M \}$. Each element of $\mathbf{p}$ could be any of the parameters listed in table 2-1. Assume the temperature on the surface of deposit at each grid point can be measured as Y_i, $i=1, 2, ..., N$. The problem is how to compute the unknown parameter vector $\mathbf{p}$, assuming that elements of $\mathbf{p}$ are independent of each other.

To solve the inverse problem on such a basis, the estimated temperature $T_i(\mathbf{p})$ on each grid point is required. $T_i(\mathbf{p})$ can be computed from the solution of the direct problem by using the estimated values of p_j, $p_j \in \mathbf{p}$, $j = 1, 2, ..., M$. The estimated temperature distribution $T_i(\mathbf{p})$ should match the measured temperature distribution Y_i as closely as possible. One way to realize such a matching is to require that the traditional least squares norm is minimized with respect to each of the unknown parameter components p_j. Here the least squares norm is modified by the addition of a zeroth-order regularization term[38]. The least squares norm is set up as:

$$S(\hat{\mathbf{p}}) = \sum_{i=1}^{N} [Y_i - \hat{T}_i(\hat{\mathbf{p}})]^2 + \alpha^* \sum_{j=1}^{M} \hat{p}_j^2 , \qquad (4.1)$$

where

i = the index number of grid points, and N is the total number of grid points.

j = the index number of unknown parameters, and M is the total number of

unknown parameters to be predicted.

Y_i= measured temperatures for each grid point.

$T_i(\hat{\mathbf{p}})$= estimated temperature obtained from the solution of the direct problem by using the estimated values of the unknown parameters $\hat{\mathrm{p}} = \{\hat{p}_1, \hat{p}_2, ..., \hat{p}_M\}$.

$\hat{p}_j$ = element of the estimated parameter vector $\hat{\mathrm{p}} = \{\hat{p}_1, \hat{p}_2, ..., \hat{p}_M\}$.

α^* = the regularization parameter, $\alpha^* > 0$.

Here, the superscript ^ over T or p denotes the estimated values. In Equation (4.1), the first summation term on the right-hand side is the traditional least squares. The second summation is the zero-order regularization term which is added in order to reduce instability or oscillations that are inherent in the solution of ill-posed problems when a large number of parameters are to be estimated [39]. The coefficient α^* is called the regularization parameter. As $\alpha^* \to 0$, the solution exhibits oscillatory behavior and becomes unstable if a large number of parameters are to be estimated. However, for large values of α^*, the solution is damped and deviates from the exact results. By proper selection of α^*, instability can be alleviated [40, 41]. Thus, selection of α^* is critical when the number of parameters is large.

Equation (4.1) is minimized by differentiating it with respect to each of the unknown parameters p_j and then setting the resulting expression equal to zero.

$$\frac{\partial S}{\partial \hat{p}_j} = 2\sum_{i=1}^{N}\left(\frac{\partial \hat{T}_i(\hat{\mathbf{p}})}{\partial \hat{p}_j}\right)\cdot[\hat{T}_i(\hat{\mathbf{p}}) - Y_i] + 2\alpha^*\sum_{k=1}^{M}\hat{p}_k\frac{\partial \hat{p}_k}{\partial \hat{p}_j} = 0, \qquad (4.2)$$

where j, k = 1, 2, ..., M, since components of unknown parameter vector $\mathbf{p}$ are independent,

$$\frac{\partial \hat{p}_k}{\partial \hat{p}_j} = \begin{cases} 0 & \text{for} \quad k \neq j \\ 1 & \text{for} \quad k = j \end{cases} \tag{4.3a}$$

Here, the total number of grid points N should be larger than the number of unknown parameters M[42]. In addition, the number of grid points should also ensure uniqueness of the estimated thermal property parameters[43].

Equation (4.2) can be rearranged in the form

$$\sum_{i=1}^{N}\left(\frac{\partial \hat{T}_i(\hat{\mathbf{p}})}{\partial \hat{p}_j}\right)\cdot[Y_i - \hat{T}_i(\hat{\mathbf{p}})] = \alpha^{*}\sum_{k=1}^{M}\hat{p}_k\frac{\partial \hat{p}_k}{\partial \hat{p}_j} \tag{4.3b}$$

where $i = 1, 2, \ldots, N$ and $j, k = 1, 2, \ldots, M$ and

$$\frac{\partial \hat{T}_i(\hat{\mathbf{p}})}{\partial \hat{p}_j} = \frac{\partial \hat{T}_i(\hat{p}_1, \hat{p}_2, \ldots, \hat{p}_M)}{\partial \hat{p}_j} \equiv X_{ij} = \begin{array}{l}\text{sensitivity coefficients} \\ \text{with respect to } \hat{p}_j\end{array} \tag{4.3c}$$

Equation (4.3b) can be written in matrix form as:

$$\mathbf{X}^{t}(\mathbf{Y} - \mathbf{T}) = \alpha^{*}\mathbf{p} \tag{4.4a}$$

where

$$\mathbf{T} = \begin{bmatrix} \hat{T}_1 \\ \hat{T}_2 \\ \vdots \\ \hat{T}_N \end{bmatrix}, \qquad \mathbf{Y} = \begin{bmatrix} Y_1 \\ Y_2 \\ \vdots \\ Y_N \end{bmatrix}, \qquad \mathbf{p} = \begin{bmatrix} \hat{p}_1 \\ \hat{p}_2 \\ \vdots \\ \hat{p}_M \end{bmatrix} \tag{4.4b,c,d}$$

$$\mathbf{X} = \frac{\partial \mathbf{T}}{\partial \mathbf{p}^{t}} = \begin{bmatrix} \frac{\partial \hat{T}_1}{\partial \hat{p}_1} & \frac{\partial \hat{T}_1}{\partial \hat{p}_2} & \cdots & \frac{\partial \hat{T}_1}{\partial \hat{p}_M} \\ \frac{\partial \hat{T}_2}{\partial \hat{p}_1} & \frac{\partial \hat{T}_2}{\partial \hat{p}_2} & \cdots & \frac{\partial \hat{T}_2}{\partial \hat{p}_M} \\ \cdots & \cdots & \cdots & \cdots \\ \frac{\partial \hat{T}_N}{\partial \hat{p}_1} & \frac{\partial \hat{T}_N}{\partial \hat{p}_2} & \cdots & \frac{\partial \hat{T}_N}{\partial \hat{p}_M} \end{bmatrix}, \tag{4.4e}$$

Here, **X** is called the sensitivity coefficient matrix with respect to vector **p**, and the elements of this matrix are

$$X_{ij} \equiv \frac{\partial \hat{T}_i}{\partial \hat{p}_j}, \qquad i = 1, 2, \ldots, N \quad \text{and} \quad j = 1, 2, \ldots, M. \tag{4.5}$$

The sensitivity coefficient X_{ij} defined by Equations (4.3c), (4.4e) and (4.5) is the first derivative of the dependent variable (i.e., temperature) with respect to the unknown parameter (i.e., laser power, beam width, etc.). It represents the changes in T_i with respect to the changes in the unknown parameter p_j. A small value of X_{ij} indicates insensitivity of the dependent variable to changes in the value of the unknown parameter. For such cases the inverse analysis becomes very sensitive to measurement errors and the estimation process becomes difficult. Therefore, it is preferable to have large, uncorrelated values of the sensitivity coefficients X_{ij}.

Thus through the above derivations, the IHCP is reduced to that of solving the system of least-squares Equations (4.2) or (4.4) by a suitable algorithm.

4.3 Solution of the Least-Squares Equations

It is desirable to express Equation (4.2) in a more convenient form for the calculation of the parameter $\hat{p}_j$. This can be achieved by expanding $\hat{T}_i(\mathbf{p})$ in a Taylor series with respect to an arbitrary value of a parameter as

$$\hat{T}_i = \hat{T}_{0i} + \sum_{k=1}^{N} \frac{\partial \hat{T}_i}{\partial \hat{p}_k} (\hat{p}_k - \hat{p}_0) \tag{4.6a}$$

This result is expressed in the matrix form as

$$\mathbf{T} = \mathbf{T}_0 + \frac{\partial \mathbf{T}}{\partial \mathbf{p}^t}(\mathbf{p} - \mathbf{p}_0) \tag{4.6b}$$

If one chooses $\mathbf{T}_0 = \mathbf{0}$ and $\mathbf{p}_0 = \mathbf{0}$, Equations (4.6a) and (4.6b) reduce, respectively, to

$$\hat{T}_j = \sum_{h=1}^{N} \frac{\partial \hat{T}_i}{\partial \hat{p}_h} \hat{p}_h \tag{4.7a}$$

and

$$\mathbf{T} = \frac{\partial \mathbf{T}}{\partial \mathbf{p}^t}\mathbf{p} \equiv \mathbf{X}\mathbf{p} \tag{4.7b}$$

substituting Equation (4.7a) into Equation (4.2) gives

$$\sum_{i=1}^{N} \frac{\partial \hat{T}_i}{\partial \hat{p}_j}\left(Y_i - \sum_{h=1}^{N} \frac{\partial \hat{T}_i}{\partial \hat{p}_h} \hat{p}_h \right) = \alpha^* \sum_{k=1}^{M} \hat{p}_k \frac{\partial \hat{p}_k}{\partial \hat{p}_j} \tag{4.8a}$$

The matrix form of this equation is obtained by introducing Equation (4.7b) into Equation (4.4a)

$$\mathbf{X}^t(\mathbf{Y} - \mathbf{X}\mathbf{p}) = \alpha^* \mathbf{p} \tag{4.8b}$$

The solution for p_j or $\mathbf{p}$ of Equation (4.8a) or (4.8b) gives the estimated values of parameters based on the measured temperature $\mathbf{Y}$:

$$\mathbf{p} = (\mathbf{X}^t\mathbf{X} + \alpha^* \mathbf{I})^{-1}\mathbf{X}^t\mathbf{Y} \tag{4.9}$$

Based on Equation (4.9), an iterative algorithm, the Levenberg-Marquardt's algorithm[43], is developed to calculate the unknown parameter vector $\mathbf{p}$ iteratively:

$$\mathbf{p}^{k+1} = \mathbf{p}^k + (\mathbf{X}^t\mathbf{X} + \alpha^* \mathbf{I})^{-1}\mathbf{X}^t(\mathbf{Y} - \mathbf{T}) \tag{4.10}$$

This algorithm is a combination of the *Newton method* which converges fast but requires a good initial guess, and the *steepest descent method* which converges slowly but does not require a good initial guess. For $\alpha^* \to 0$, Equation (4.10) reduces to the *Newton's method* and for $\alpha^* \to \infty$, it becomes the *steepest descent method.*

4.4 Algorithm to Solve IHCP

The solution algorithm with the Levenberg-Marquardt method is as follows. Suppose the unknown parameter vector $\mathbf{p}^k$ at the kth iteration is available.

Step 1. Solve the direct problem from Equations (3.23)-(3.26) with a finite-difference scheme by using the estimated values of the parameters $\mathbf{p}^k = (p_1^k, p_2^k, \ldots, p_M^k)$ at the kth iteration and compute the temperature distribution $\mathbf{T}$.

Step 2. Since the problem involves M unknown parameters, solve the direct problem M more times, each time perturbing only one of the parameters by a small amount and compute.

$$\mathbf{T}(p_1+\Delta p_1, p_2, \ldots, p_M)$$

$$\mathbf{T}(p_1, p_2+\Delta p_2, \ldots, p_M)$$

$$\vdots$$

$$\mathbf{T}(p_1, p_2, \ldots, p_M+\Delta p_M)$$

Step 3. Compute the sensitivity coefficients defined by Equation (4.5) for each parameter. For example, with respect to parameter p_1,

$$\frac{\partial T_i}{\partial p_1} = \frac{T_i(p_1 + \Delta p_1, p_2, \ldots, p_M) - T_i(p_1, p_2, \ldots, p_M)}{\Delta p_1} \tag{4.11}$$

for $i = 1, 2, \ldots, N$ and determine the sensitivity matrix $\mathbf{X}$ defined by Equation (4.4).

Step 4. Compute $(\mathbf{X}^t\mathbf{X} + \alpha^*\mathbf{I})^{-1}\mathbf{X}^t(\mathbf{Y} - \mathbf{T})$ with a chosen α^*.

Step 5. Compute $\mathbf{p}^{k+1}$ by Equation (4.10).

Step 6. Repeat the calculations until the following convergence criterion is satisfied.

$$\frac{|S^{k+1} - S^k|}{S^{k+1}} < \varepsilon \tag{4.12}$$

Thus, theoretically the unknown parameter vector **p** can be calculated through above procedures if the temperature distribution on the surface is known. Hence the results of this chapter provide the theory to construct a model of growth of a cylindrical rod, which will be demonstrated in detail in the next chapter.

CHAPTER FIVE

MODEL APPLICATION: GROWTH OF A CYLINDRICAL ROD ON THREE DIMENSIONAL LCVD

5.1 Problem Description

The model constructed in chapter four is a general case for solving an inverse heat conduction problem. In chapter five, this model will be applied to grow a microstructure with a desired pre-specified geometry, i.e., a cylindrical rod, by three-dimensional LCVD. Assuming two parameters, laser power P_o and laser beam width ω, are used to control the LCVD process, then for this specified problem, the objective is to predict P_o and ω over time, in order to grow a cylindrical rod. It should be pointed out that this problem is an inverse problem because it is from the temperature field required for the pre-determined growth that one determines the parameters (laser power and beam width). None of the existing models in the literature can accomplish this inverse objective. The idea of a pre-specified geometry has been first used in a recent paper[29] for predicting the laser dwell times (or laser scanning pattern) on the surface scanned by the laser beam for obtaining a desired microstructure, such as a micro-lens.

In this chapter, an axisymmetric numerical model is developed for predicting laser power P_o over time and laser beam width ω over time, which are required for the growth of a cylindrical rod. To this end, one needs the following procedures: (1) Pre-

specify the geometry of the rod and the expected growth, (2) compute the required temperature distribution from the growth-rate Equation (3-12), (3) obtain the temperature profile based on the solution of the heat conduction equation, and then optimize the laser power and laser beam width by using the least squares method.

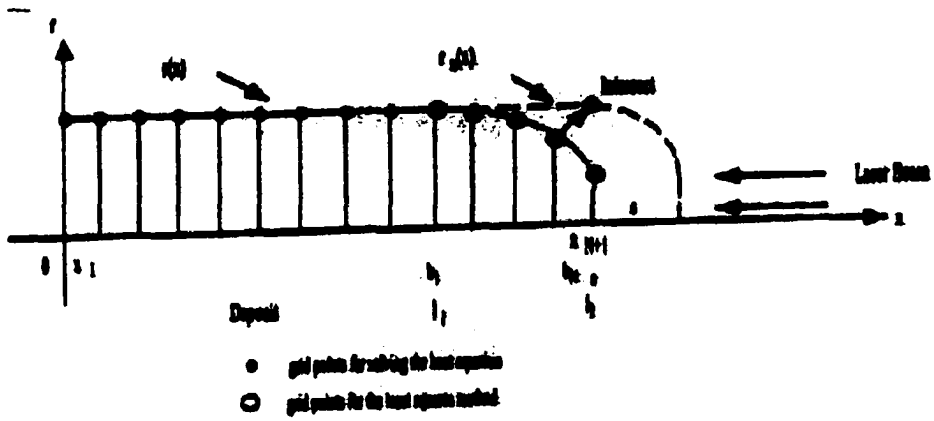

Figure 5-1 Schematic of cylindrical rod growth and a mesh for the current surface[44].

5.2 Specification of the Geometry of the Rod

Most SEM (scanning electronic micro-spectroscopy) photos of rods grown by LCVD show that the top of a rod is a parabolic-like curve. Thus the geometry of a cylindrical rod is specified as in Figure5-1. The surface *r(x)* is defined as:

$$r(x)=\begin{cases} R, & 0 \le x < L_1 \\ c\sqrt{A-x}, & L_1 \le x \le L \\ tipr, & x = L \end{cases} \tag{5.1}$$

In Equation (5.1), L is the total length of the rod. The rod consists of two portions: when $0 \le x < L_1$, the rod is straight with radius R and L_1 is the length of that portion; when $L_1 \le x \le L$, the curve is the portion of a parabola which is used to simulate the surface of

the rod near the tip. The intersect point of these two portions is known as the critical point which is at (L_1, R) in the x-r coordinate. Since the boundary condition (Equation 3.19) does not allow the radius of the rod tip to be zero, the tip of the rod is considered flat. The radius of the rod tip is *tipr*. A and c are constants to be calculated as the following.

From Figure 5-1, it is seen that when $x = L_1$, $r(x) = R$, and when $x = L$, $r(x) = tipr$. After substituting in Equation (5.1) and rearranging, one can reach the following equations:

$$L_1 = A - (R/c)^2 \tag{5.2a}$$

$$L = A - (tipr/c)^2 \tag{5.2b}$$

solving (5.2a) and (5.2b), A and c can be calculated by:

$$A = L + \frac{tipr^2(L - L_1)}{R^2 - tipr^2} \tag{5.3a}$$

$$c = \sqrt{\frac{R^2 - tipr^2}{L - L_1}} \tag{5.3b}$$

Once R, L, L_1 and *tipr* are specified, the geometry of the rod is pre-specified by Equation (5.1). Since the normal unit vector $\mathbf{n}(x)$ at the rod surface $r(x)$, $0 \leq x < L_1$, is perpendicular to the x-direction, there is no heat absorbed in the $[0, L_1)$ surface interval, based on Equation (3.17). In order to simulate growth so as to agree with the pre-specified cylindrical geometry, equidistant grid points in the x-direction on $[L_1, L]$ are chosen as follows: $(x_i, r(x_i))$, $i = 0, 1, 2, \ldots, M$, and $h = x_{i+1} - x_i$, with $x_o = L_1$ and $x_M = L$. Thus, $r_i(x_i)$ can be obtained at each grid point from Equation (5.1) as A and c are calculated form Equations (5.3a) and (5.3b), respectively.

5.3 Calculation of Required Temperature Distribution

For the model constructed in chapter four, growth is determined from the temperature distribution on the surface of the deposit. However, in this work the temperature distribution at each grid point is calculated base on the specified rod growth (Figure 5-1) from the current surface (solid line) to the new surface (dotted line). After the geometry of the cylindrical rod is pre-specified, the following steps are needed to calculate the required temperature distribution at each grid point.

5.3.1 Calculation of Growth on Each Grid Point

As seen in Figure 5-1, a certain grid point i (x_i, $r_i(x_i)$) on the surface of the deposit grows along its normal direction towards the new surface. The intersection of the normal line and the new surface is at point (x_i^{new}, r_i^{new}). Growth at this grid point is defined as the distance between this point (x_i, r_i) on the current surface and a point (x_i^{new}, r_i^{new}) on the grown new surface. To calculate the growth at each grid point, the following steps are needed.

Step 1. Determine the normal line through each grid point.

If the slope of the normal line through grid point i (x_i, r_i) is s_i, the s_i can be easily obtained from Equation (5.1) as:

$$s_i = c^2/2r_i\,, \tag{5.4a}$$

thus the normal line through point i can be obtained by:

$$x = s_i(r - r_i) + x_i \tag{5.4b}$$

Step 2. Determine the intersection (x_i^{new}, r_i^{new}) of the normal line and the new surface.

Assuming that growth along the x-axis is a, from the current surface layer

to the next layer, then the new surface is determined as:

$$r(x) = \begin{cases} R, & 0 \le x < L_1 + a \quad (5.5a) \\ c\sqrt{A + a - x}, & L_1 + a \le x \le L + a \quad (5.5b) \\ tipr, & x = L + a \quad (5.5c) \end{cases}$$

Solving Equations (5.4b) and (5.5), one can calculate the intersection point of the normal line and the new surface for each grid point. The solution should be on both the straight portion and parabolic portion of the rod.

On the straight portion of the rod,

$$\begin{aligned} x_i^{new} &= \frac{c^2}{2r_i}(R - r_i) + x_i \\ r_i^{new} &= R \end{aligned} \quad , \qquad (5.6)$$

on the parabolic portion of the rod,

$$\begin{aligned} r_i^{new} &= \frac{-s_i + \sqrt{s_i^2 - (4/c^2)(x_i - s_i r_i - a - A)}}{(2/c^2)} \\ x_i^{new} &= s_i(r_i^{new} - r_i) + x_i \end{aligned} \qquad (5.7)$$

Step 3. Calculate the growth distance at each grid point by:

$$\Delta x_i = \sqrt{(x_i^{new} - x_i)^2 + (r_i^{new} - r_i)^2} \qquad (5.8)$$

for $i = 1, 2, \ldots, M\text{-}1$ with $\Delta x_o = 0$, $\Delta x_M = a$.

5.3.2 Calculation of the Required Surface Temperature Distribution

Once the growth distance Δx_i is obtained from Equation (5.8), in a certain time period Δt, the required temperature for that much growth can be calculated from Equation (3.12) as follows:

$$(T_d)_i^r = -\frac{E_a}{R \ln \frac{\Delta x_i}{K_o \Delta t}}, \quad \text{for } i = 0, 1, 2, \ldots, M. \tag{5.9}$$

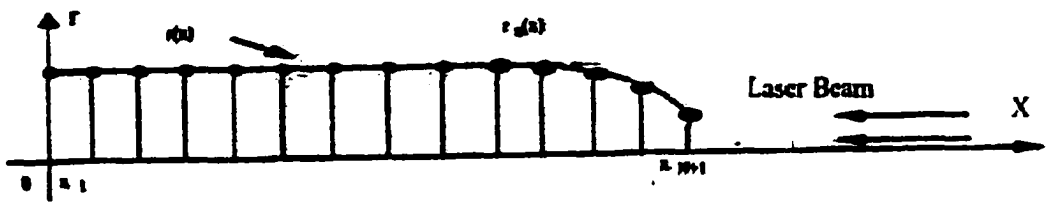

Figure 5-2 The mesh for surface of a cylindrical rod.

5.4 Calculation of the Temperature Distribution Based on the Heat Equations

It is mentioned in chapter four that an iterative method must be used to solve this inverse heat problem (Equation 4.10). The parameter vector **p** consists of two parameters, laser power P_o and beam width ω. Suppose at the kth iteration the estimated values of the laser power P_o and beam width ω are available; then one can calculate the temperature distribution $\mathbf{T}_d$ on the whole surface of the rod from Equations (3.23)-(3.26) which are Equations (5.10)-(5.13) in this section. To obtain the numerical solution of these heat equations, one can consider a mesh on the current surface, $\mathbf{R}(x, r)$, of the rod, as shown in Figure5-2. The grid points (x_i, r_i), $i = 1, 2, \ldots, N+1$, are chosen to be equidistant grid points in the x direction, i.e., $h = x_i - x_{i-1}$, with $x_1 = 0$ and x_{N+1} is at the tip of the rod. It is

necessary that the grid points on the interval $[L_1, L]$ must overlap with the grid points defined for the calculation of the required temperature distribution $\mathbf{T_d}^r$ in the last section, so that the least squares optimization can be used to minimize the difference between $\mathbf{T_d}^r$ and $\mathbf{T_d}$.

$$-\frac{k_d r_{i-1/2}^2}{h^2}\theta_{i-1} + \frac{k_d (r_{i-1/2}^2 + r_{i+1/2}^2)}{h^2}\theta_i - \frac{k_d r_{i+1/2}^2}{h^2}\theta_{i+1} = r_i[h_{conv}\theta_i - Q_{in}^{"}(x_i)] \tag{5.10}$$

where $i = 2, 3, \ldots, N$, $\theta_i = T_d - T_\infty$ with T_∞ being the surrounding temperature and

$$Q_{in}^{"}(x_i) = 2P_o(\Lambda / \pi\omega^2)e^{-2r_i^2/\omega^2}[\hat{x} \cdot \hat{n}(x_i)] \tag{5.11}$$

with boundary condition for the flat tip,

$$\frac{\theta_{N+1} - \theta_N}{h} = \frac{\lambda P_o e^{-2(\frac{tipr}{\omega})^2} - h_{conv}\theta_{N+1}}{\pi k_d \cdot tipr^2} \tag{5.12}$$

and with boundary condition at the bottom of the rod:

$$\frac{\theta_2 - \theta_1}{h} = \frac{3k_s\theta_1}{8k_d r_1^3} \tag{5.13}$$

Equations (5.10), (5.12) and (5.13) are linear systems with $N+1$ unknowns and $N+1$ linear equations. The matrix form for this system is:

$$\mathbf{A\theta = b} \tag{5.14}$$

where **A** is the coefficient matrix which is tri-diagonal with size $(N+1) \times (N+1)$,

$$\mathbf{A} = \begin{bmatrix} d_1 & u_1 & 0 & \cdots & \cdots & 0 \\ l_2 & d_2 & u_2 & \ddots & & \vdots \\ 0 & l_3 & d_3 & u_3 & \ddots & \vdots \\ \vdots & \ddots & \ddots & \ddots & \ddots & 0 \\ 0 & \cdots & 0 & l_{N+1} & d_{N+1} & \end{bmatrix} \tag{5.15a}$$

and $\boldsymbol{\theta}$ is a $N+1$ dimensional column vector of unknowns, $\mathbf{b}$ is also a $N+1$ dimensional column vector of non-homogeneous terms:

$$\boldsymbol{\theta} = \begin{bmatrix} \theta_1 \\ \theta_2 \\ \vdots \\ \theta_{N+1} \end{bmatrix}, \qquad \mathbf{b} = \begin{bmatrix} b_1 \\ b_2 \\ \vdots \\ b_{N+1} \end{bmatrix} \tag{5.15b,c}$$

In matrix **A**, $d_1, d_2, \ldots, d_{N+1}$ are diagonal elements, $u_1, u_2, \ldots, u_N$ are upper diagonal elements and $l_2, l_3, \ldots, l_{N+1}$ are lower diagonal elements. d_1, u_1, b_1 can be obtained from the boundary condition Equation (5.13) as:

$$d_1 = 3k_s / (8k_d R^3) + 1/h, \tag{5.16a}$$

$$u_1 = -1/h, \tag{5.16b}$$

$$b_1 = 0, \tag{5.16c}$$

and $l_{N+1}, d_{N+1}, b_{N+1}$ can be obtained from the boundary condition Equation (5.12) as:

$$l_{N+1} = -1/h, \tag{5.17a}$$

$$d_{N+1} = \frac{(h_{conv})_{N+1}}{\pi k_d tipr^2} + \frac{1}{h}, \tag{5.17b}$$

$$b_{N+1} = \frac{\lambda P_o}{\pi k_d tipr^2} e^{-2(\frac{tipr}{\omega})^2}, \tag{5.17c}$$

other entries of matrix **A** can be calculated as follows:

$$d_i = \frac{k_d (r_{i-1/2}^2 + r_{i+1/2}^2)}{h^2} - r_i h_{conv}, \text{ for } i = 2, 3, \ldots, N \tag{5.18a}$$

$$u_i = -\frac{k_d r_{i+1/2}^2}{h^2}, \text{ for } i = 2, 3, \ldots, N \tag{5.18b}$$

$$l_i = -\frac{k_d r_{i-1/2}^2}{h^2}, \text{ for } i = 2, 3, \ldots, N \tag{5.18c}$$

$$b_i = r_i \cdot Q_{in}^{''}(x_i) = 2P_o(\Lambda / \pi\omega^2) \cdot r_i e^{-2r_i^2/\omega^2} [\hat{x} \cdot \hat{n}(x_i)] \tag{5.18d}$$

In Equation (5.18d), an absorption coefficient $\Lambda = 1$, implies that all heat energy delivered by the laser beam is absorbed by the substrate or deposit. The term $[\hat{x} \cdot \hat{n}(x_i)]$ is the scalar product of vector **x** and the normal vector **n** at grid point i. If ϕ is the angle between these two vectors, this term can be calculated as:

$$[\hat{x} \cdot \hat{n}(x_i)] = x_i \cos\phi = \frac{x_i}{\sqrt{1+\tan^2\phi}} = \frac{x_i \tan\gamma}{\sqrt{1+\tan^2\gamma}} = \frac{x_i s_i}{\sqrt{1+s_i^2}} \tag{5.19}$$

In the above derivation, γ is the angle between the normal line and r-direction, and s_i is the slope of the normal line at grid point i, which can be calculated by Equation (5.4a).

The coefficient matrix **A** can be considered to be **strictly diagonally dominant**. Based on this condition, the *Thomas Algorithm* [45] can be applied to solve this linear system efficiently. The solution is the temperature distribution on the whole rod surface, from the bottom to tip of the rod. However, only the temperature distribution $(T_d)_i$, $i = 0, 1, \ldots, M$, on the parabolic portion of the rod is selected, in order to match the required temperature distribution $(T_d)_i^r$, with $i = 0, 1, \ldots, M$, again, M is the number of grid points on the parabolic portion of the rod.

5.5 Optimization by the Least Squares Method

In section 5.3, the expected temperature distribution $(T_d)_i^r$ required for the growth of a straight rod is obtained. In section 5.4, the temperature distribution $(T_d)_i$ is calculated based on the heat equation for given P_o and ω. In this section, least squares method is used to minimized the difference between the temperature distribution $(T_d)_i^r$ and the temperature distribution $(T_d)_i$, so that P_o and ω are optimized. Since the number of

unknown parameters are few (i.e., two only) the regularization term is not needed[43]. Thus, the least squares norm is set up as follows:

$$S(P_o,\omega)=\sum_{i=0}^{M}[(T_d)_i^r-(T_d)_i]\ ,\ i=0,\ 1,\ \ldots,\ M \tag{5.20}$$

In Equation (5.10), the temperature distribution $(T_d)_i^r$ is pre-defined by the pre-specified geometry of the rod and it does not depend on the parameters P_o and ω. On the other hand, the temperature distribution $(T_d)_i$ is calculated for a given P_o and ω and it does depend on P_o and ω. Minimizing $S(P_o, \omega)$ of Equation (5.20), one can obtain:

$$\frac{\partial}{\partial P_o}S(P_o,\omega)=2\sum_{i=1}^{M}\left(\frac{\partial(T_d)_i}{\partial P_o}\right)[(T_d)_i^r-(T_d)_i]=0 \tag{5.21a}$$

$$\frac{\partial}{\partial \omega}S(P_o,\omega)=2\sum_{i=1}^{M}\left(\frac{\partial(T_d)_i}{\partial \omega}\right)[(T_d)_i^r-(T_d)_i]=0 \tag{5.21b}$$

Expressing Equations (5.21a,b) in matrix form, gives

$$\mathbf{X}\,(\mathbf{T_d}^r-\mathbf{T_d})=\mathbf{0}, \tag{5.22}$$

where $\mathbf{X}$ is the sensitivity coefficient matrix, which is a $2\times(M+1)$ matrix:

$$\mathbf{X}=\begin{bmatrix}\dfrac{\partial(T_d)_0}{\partial P_o} & \dfrac{\partial(T_d)_1}{\partial P_o} & \cdots & \dfrac{\partial(T_d)_M}{\partial P_o}\\ \dfrac{\partial(T_d)_0}{\partial \omega} & \dfrac{\partial(T_d)_1}{\partial \omega} & \cdots & \dfrac{\partial(T_d)_M}{\partial \omega}\end{bmatrix}, \tag{5.23a}$$

$\mathbf{T_d}^r$ is the required temperature distribution, and $\mathbf{T_d}$ is the calculated temperature distribution from the heat equations:

$$\mathbf{T_d}^r=\begin{bmatrix}(T_d)_0^r\\ (T_d)_1^r\\ \vdots\\ (T_d)_M^r\end{bmatrix},\qquad \mathbf{T_d}=\begin{bmatrix}(T_d)_0\\ (T_d)_1\\ \vdots\\ (T_d)_M\end{bmatrix}. \tag{5.23b}$$

According to Equation (4.10), the solution of P_o and ω can be calculated iteratively by:

$$\begin{pmatrix} P_o^{(k+1)} \\ \omega^{(k+1)} \end{pmatrix} = \begin{pmatrix} P_o^{(k)} \\ \omega^{(k)} \end{pmatrix} + (\mathbf{X}^t\mathbf{X} + \alpha^*\mathbf{I})^{-1}\mathbf{X}^t(\mathbf{T_d}^r - \mathbf{T_d}^{(k)}) \qquad (5.24)$$

5.6 Algorithm for the Solution to Grow a Cylindrical Rod

The following algorithm is developed to calculate the laser power P_o over time and the beam width ω over time in order to grow cylindrical rods.

Step 1. Pre-specify the geometry of the rod surface $r(x)$ and choose grid points as in Figure 5-1. Find the normal straight line for each grid point from Equation (5.4). After specifying a, the growth length expected at the tip of the rod, calculate the expected growth surface $r_{new}(x)$ according to Equation (5.5).

Step 2. Find the intersection of the normal line on the expected growth curve $r_{new}(x)$ from Equation (5.6) and Equation (5.7) for each grid point. Then calculate the growth on each grid point from Equation (5.8). After specifying the time interval Δt, calculate the required temperature distribution $\mathbf{T_d}^r$ for growth of a cylindrical rod from Equation (5.9).

Step 3. Solve the direct problem from Equations (5.10)-(5.13) with finite-differences by using the estimated values of the parameters $\mathbf{p}^{(k)} = (P_o^{(k)}, \omega^{(k)})$ at the kth iteration and compute the temperature distribution on the whole rod surface. Select the temperature distribution on the parabolic portion as the $(T_d)_i$, $i = 0, 1, \ldots, M$, to be compared with the required temperature distribution.

Step 4. Since the problem involves two unknown parameters, P_o and ω, solve the direct problem two more times, each time perturbing only one of the parameters by a small amount and compute.

$$\mathbf{T}_d(P_o+\Delta P_o,\ \omega)$$

$$\mathbf{T}_d(P_o,\ \omega+\Delta\omega)$$

Step 5. Compute the sensitivity coefficients defined by Equation (4.5) for each parameter.

$$\frac{\partial(T_d)_i}{\partial P_o} = \frac{T_d(P_o+\Delta P_o,\omega)_i - T_d(P_o,\omega)_i}{\Delta P_o} \tag{5.25a}$$

$$\frac{\partial(T_d)_i}{\partial \omega} = \frac{T_d(P_o,\omega+\Delta\omega)_i - T_d(P_o,\omega)_i}{\Delta\omega} \tag{5.25b}$$

for $i = 0, 1, 2, \ldots, M$ and determine the sensitivity matrix $\mathbf{X}$ defined by Equation (5.23a).

Step 6. Compute $(\mathbf{X}^t\mathbf{X} + \alpha^*\mathbf{I})^{-1}\mathbf{X}^t(\mathbf{T}_d^r - \mathbf{T}_d^{(k)})$ for a chosen α^*.

Step 7. Compute $\mathbf{p}^{k+1}$ by Equation (5.24).

Step 8. Repeat the calculations until the following convergence criterion is satisfied.

$$\frac{|S(P_o^{(k+1)},\omega^{(k+1)}) - S(P_o^{(k)},\omega^{(k)})|}{S(P_o^{(k+1)},\omega^{(k+1)})} < \varepsilon \tag{5.26}$$

In this work, ε is chosen to be 10^{-6}.

Step 9. After the optimized P_o and ω is calculated by repeating steps 3 to 8, the new surface $\mathbf{R}(x, r_{new}(x))$ is grown using the optimum P_o and ω. The new surface is reset as the current surface, $\mathbf{R}(x, r(x))$, and the process continued by repeating the above eight steps layer by layer until the desired cylindrical rod is

obtained.

Step 10. As all steps above are completed, one can obtain the functions of P_o over rod length and ω over rod length. These functions must be transformed to those of P_o over time and ω over time. This transform is easily done by dividing those functions by the growth rate. The growth rate can be calculated by:

$$R = a/\Delta t \tag{5.27}$$

where a is the growth length at the tip and Δt is the time interval to grow a at the tip. Δt and a are specified in steps 1 and 2.

Through the above ten steps, theoretically, one can obtain P_o and ω over time, required for the growth of cylindrical rods. This will be verified in chapter six. However, under present laboratory set up, beam width cannot be adjusted automatically. Hence, in this study, beam width was fixed and a solution was obtained for P_o over time.

CHAPTER SIX

EXPERIMENTAL

In this chapter, the LCVD system designed, assembled, and used for the experiments will be described in detail.

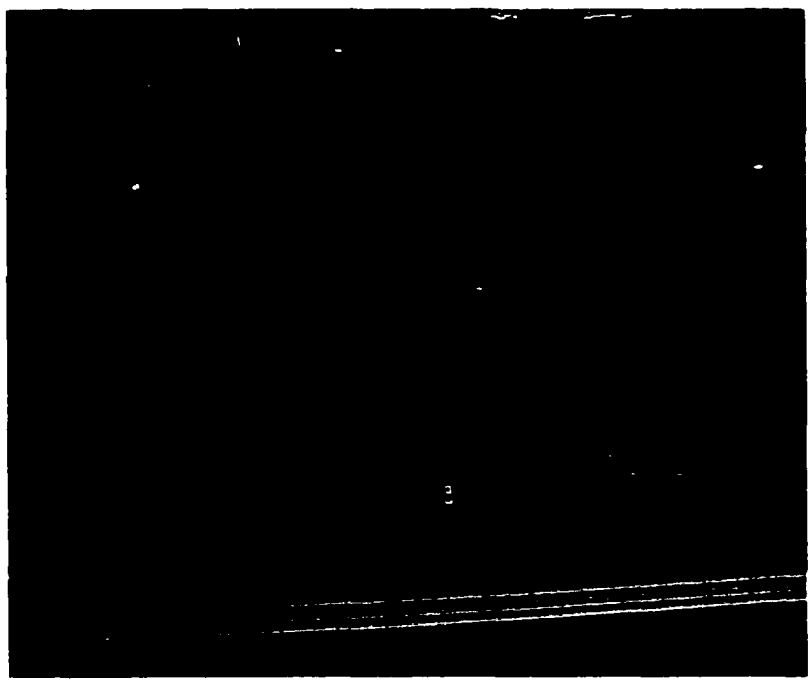

Figure 6-1 Experimental set up for the 3-D LCVD system.

6.1 Experimental Setup

In this work, the system of 3D-LCVD (Figure 6-1) consists of the following subsystems: optical system, reaction system, vacuum system, imaging system, and laser

control system. The optical system consists of a laser source, an optical lens which is used to focus the laser beam on the substrate, and a beam splitter with a beam retarder which is used to regulate the laser power delivered on the substrate. The reaction system consists of a reaction chamber, a gas source cylinder and a stage which can be moved in all **x, y, z,** directions. The vacuum system consists of a vacuum pump and a leak detector. The laser control system consists of a computer with control software, Labview. The imaging system consists of a CCD camera and a CRT monitor. The laser control system is the most critical component in the LCVD system.

6.1.1 Optical System

The optical system of 3D-LCVD includes a laser source, an optical lens and a beam splitter with a beam retarder.

Throughout the experiments, a Nd:YAG laser with a maximum output power of 10 W (TEM_{00}) was used at 1064 nm wavelength. The CW laser beam was focused by a best form laser lens, with 100-mm focal length and a diameter of one inch, yielding a spot size (beam width) on the substrate from 5 microns to 30 microns. The spot size can be calculated by the equation:

$$\omega_0 = \left(2\lambda / \pi\right) \cdot F,$$

where λ is the laser wavelength, which is 1064 nm, and F is the so-called F-number, which can be varied with the laser beam diameter. Therefore, the beam width (size of focused laser light spot) on the substrate can be adjusted by varying the F-number (i.e. varying the laser beam diameter).

Beam splitter with beam retarder are used to regulated the laser power output. With the help of these components, a computer with a control software (Labview) can easily control the laser power delivered to the reaction chamber. The function of the beam splitter and retarder will be discussed in the *Laser controlling system* part.

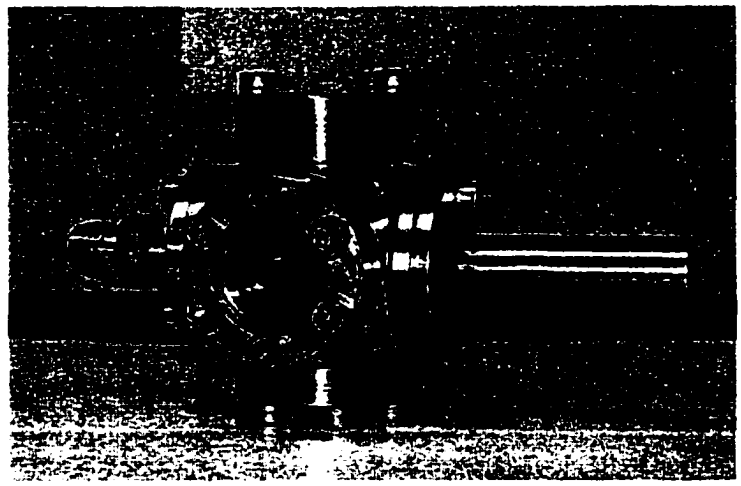

Figure 6-2 Reaction chamber for 3D-LCVD

6.1.2 Reaction System

The reaction system consists of a reaction chamber and a gas source cylinder. The reaction chamber is placed on a stage that can be moved freely in all **x, y, z** directions. The gas source cylinder is connected to the reaction chamber with a quarter-inch tubing.

The reaction chamber is the place where deposition reactions take place. It is connected to a gas source and an exhausting system (a vacuum pump) with stainless tubing. The reaction chamber (Figure 6-2) is a spherical cube, made of stainless steel that has six 1.33-inch CF ports: one port is used for observation through a CCD camera equipped with a 5x objective lens; the second port served as the laser beam entrance

window; the third port is dedicated for gas delivery from the precursor gas cylinder; the fourth port is connected to a vacuum pump in order to evacuate the chamber; the fifth port has a flange with a detachable substrate holder of aluminum; and the sixth port is closed with a blank flange, which could be used for future use. The inner surface of the reaction chamber is nickel-plated to prevent corrosion from the reaction gas mixture. Corrosion of the chamber would pollute the reaction, which would affect the experimental results. The reaction chamber is placed on a combined XY-stage, and a Z-jack stage. Thus, the reaction chamber can be moved freely in all **x**, **y**, **z** directions.

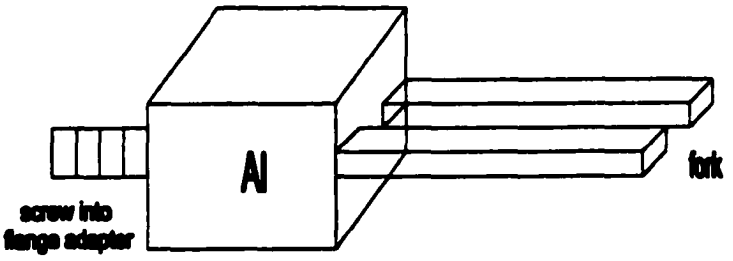

Figure 6-3 Substrate holder inside the reaction chamber.

The CF flanges are most widely used for high-vacuum and ultra-high-vacuum applications. Flange adapters are used to connect to the gas-handling system and vacuum system through a quarter-inch tubing. The view-ports, flanges, and flange adapters are mounted on the reactor using standard copper gaskets.

Inside the chamber, there is a substrate holder (Figure 6-3) made of aluminum, custom machined in the Institute for Micromanufacturing (IFM) workshop. During the

experiments the substrate, a piece of graphite or silicon, is attached to the forks of the substrate holder. Another end of the holder is screwed into a flange adapter.

The gas source cylinder (as shown in Figure 6-4), contains the precursor gas methane, CH_4, from *Scotty Special Gas* company. It has a valve with a gas regulator on its top. The cylinder is directly connected to the reaction chamber with a quarter-inch tubing.

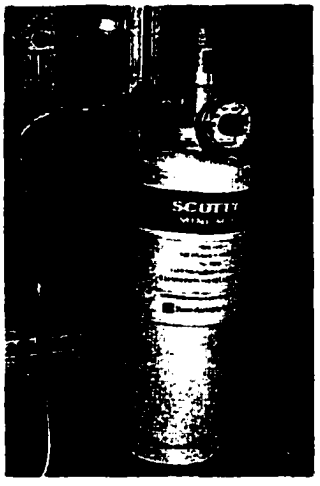

Figure 6-4 Gas source cylinder containing methane.

6.1.3 Vacuum System

There are two main functions for the vacuum system. Before the chemical reaction, the reaction chamber must be vacuumed to a certain degree to insure the pureness of the precursor gas introduced into the chamber. After the chemical reaction, the mixture of the by-product gas and the precursor gas must be exhausted by the vacuum system. The vacuum system includes a pump (Figure 6-5a), a pressure gauge that can read the pressure of the gas in the reaction chamber, and some valves and tubing for connection. The vacuum pump is a mechanical pump that could pump down the reaction chamber to about 10^{-5} torr. Before any experiment, the system is leak-checked by the

helium leak detector (Figure 6-5b). The vacuum system ensures a high vacuum level in the reactor before loading precursor gases. In this system, a leak rate less than 10^{-4} torr per minute is required. The reason for leak-check is to ensure that the system is leak-free in order to maintain the pressure of the gas in the chamber during LCVD reaction at a constant level, thus obtaining correct experimental results.

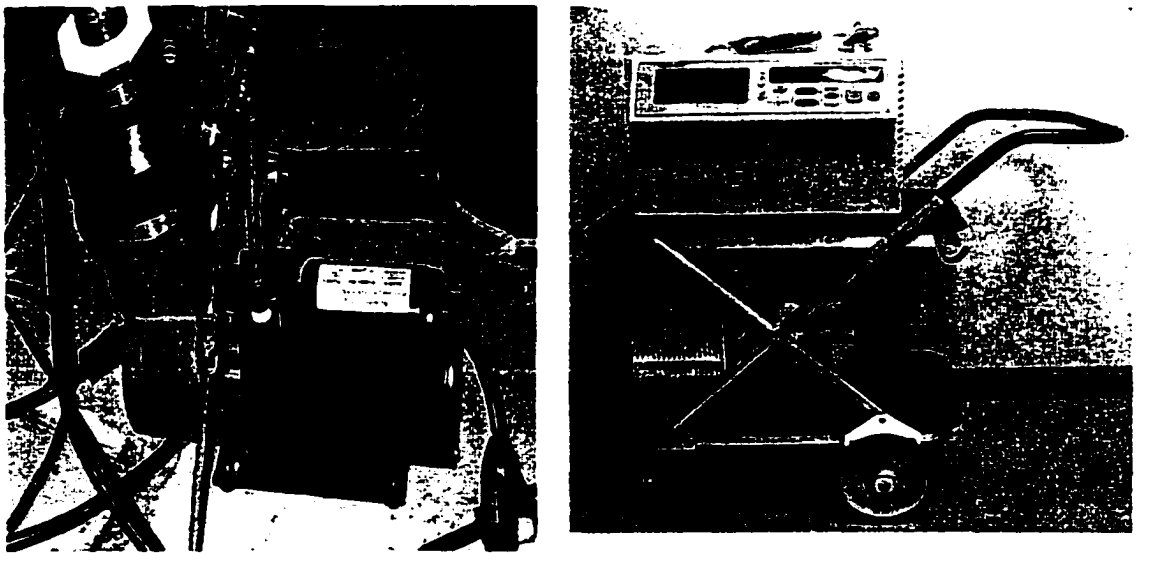

(a) (b)

Figure 6-5 Vacuum system for 3D-LCVD.
(a) vacuum pump, (b) leak detector.

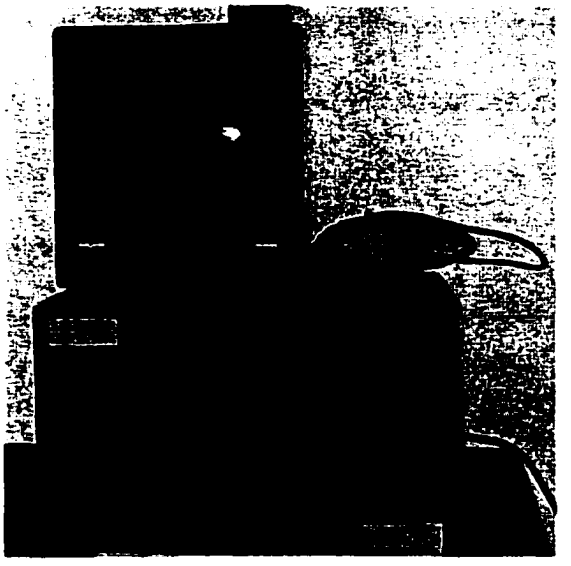

Figure 6-6 Imaging system for 3D-LCVD.

6.1.4 Imaging System

Imaging system (Figure 6-6) consists of a CCD camera, a CRT monitor and a VHS recorder. The CCD camera with a 5x objective lens is placed just above the reaction chamber. Through the glass port of the reaction chamber, the lens of the camera is pointed to the substrate. The CCD camera is connected to a monitor. During the experiment, the whole process of rod growth can be recorded and observed through the monitor. Another important function of the imaging system is used for accurate adjustment of the laser focus. By assembling all these components, one can obtain the whole LCVD system as shown in Figure 6-7.

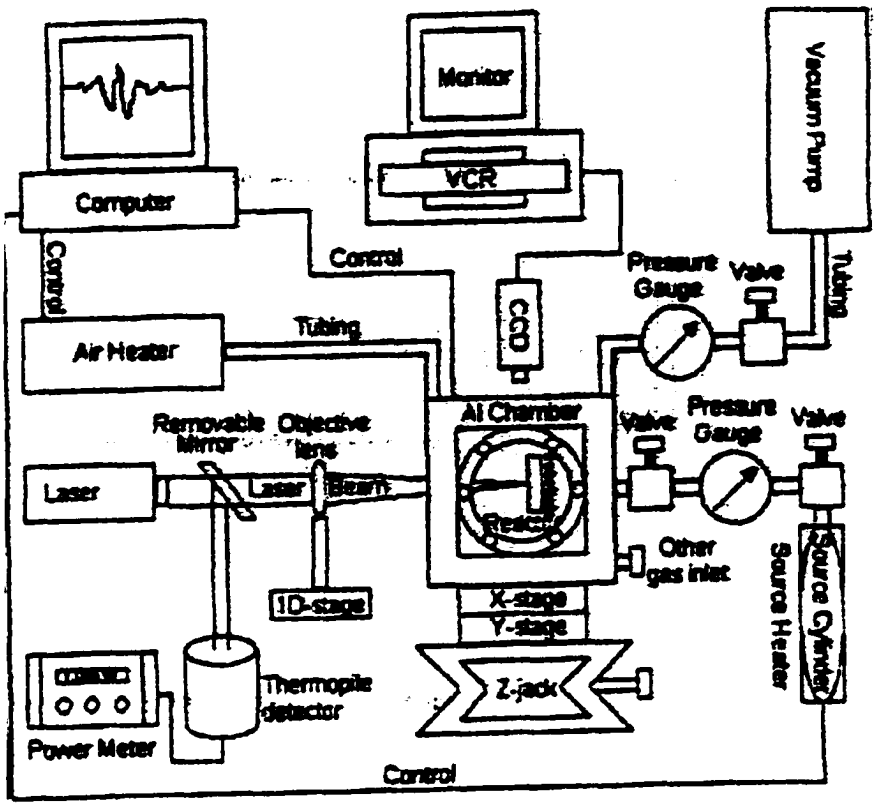

Figure 6-7 The 3D-LCVD system.

6.2 Laser Control System

In this work, laser power output and laser beam width on the substrate (or deposit) are to be controlled. Laser beam width can only be adjusted manually. Laser power output is adjusted through either the control panel of the laser source or the computer system. Using computer system to control the laser power is more accurate. More importantly, if one inputs the function of laser power versus time, then the computer can automatically regulate the laser power over time according to the function input. The calibration of laser output will be discussed in detail in the next section on *experimental procedures*.

The hardware of the laser control system consists of a laser power meter, a thermopile detector, a beam-splitter, LCD modulator (retarder or waveplate) and a computer with an interface card: PCI-1200 data acquisition card (from National Instruments). The software for the laser control system is LabView.

6.2.1 Software to Control Laser Power — LabView

LabView from National Instruments is a program development environment. Though other applications use text-based languages to create lines of code, LabView uses a graphical programming language, G, to create programs in block diagram form. LabView, like C or BASIC, is a general-purpose programming system with extensive libraries of functions for any program task. LabView includes libraries for data acquisition, GPIB and serial instrument control, data analysis, data presentation, and data storage. LabView uses the powerful graphical language, G, to create Virtual Instruments (VIs). A VI consists of an interactive user interface, a dataflow diagram that serves as the

Figure 6-8 Front panel to control laser power generated by Labview.

source code, and icon connections that allow the VI to be called from higher level VIs. The front panel (interactive user interface) displays numerical, string, array, graphical, or Boolean output values from the background graphical program. The front panel also displays control knobs, slides, dials, switches, and numerical, array, Boolean, or string input values. This setup allows a user to control values being used by the background program while also seeing outputted values manipulated by the program. A LabView programmer can move and resize any of these input/output visuals to his or her liking. This ability of LabView makes the Virtual Instrument designed by the programmer unique and ergonomic to the specific application it is intended for. The VI receives instructions from a block diagram, which a programmer constructs in language G. The block diagram is a pictorial solution to a programming problem. VIs are hierarchical and modular, and a programmer can use them as top-level programs, or as subprograms within other programs. A VI within another VI is called a sub VI. The icon and connector of a VI work like a graphical parameter list so that other VIs can pass data to a sub VI. In this work, the front panel made by LabView is shown as Figure 6-8. In this figure, the 'Amplitude' represents the value of the electrical voltage applied on the liquid crystal retarder. The retarder works with the beam splitter together to regulate the laser power. The value of the voltage is approximately proportional to the laser power applied to the reaction chamber. Thus after calibration of laser output, one can obtain the desired laser power applied to the reaction chamber by just dialing the knob on the front panel.

6.2.2 Hardware to Control Laser Power

The hardware of the laser control system consists of a laser power meter, a thermopile detector, a beam-splitter, a liquid crystal retarder or waveplate, and a computer with an interface card: PCI-1200 data acquisition card (from National Instruments).

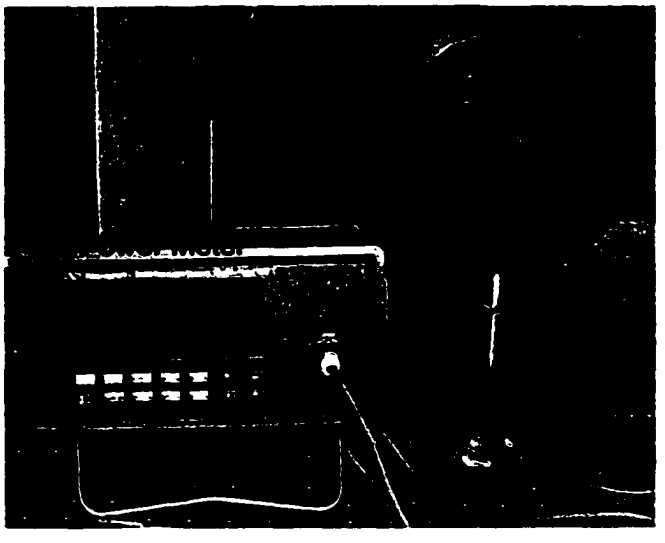

Figure 6-9 Thermopile detector and laser power meter.

The thermopile detector, as seen in Figure 6-9, is connected to the laser power meter. Both of them are used to measure the laser power. The thermopile detector is used to collect the laser light. The heat energy (per unit time) is then transformed to a certain signal. This signal then is passed to the laser power meter and is displayed digitally as the reading of laser power output. Thus, once a laser beam is incident on the thermopile detector, the exact laser power of that laser beam is displayed on the power meter. One can calculate the power density by dividing the laser power by the area of the cross section of the laser beam. In this work, thermopile detector and laser power meter

are used to calibrate the laser power. After calibration, one can obtain a desired laser power delivered to the substrate by dialing that value of the laser power on the knob as shown in Figure 6-8.

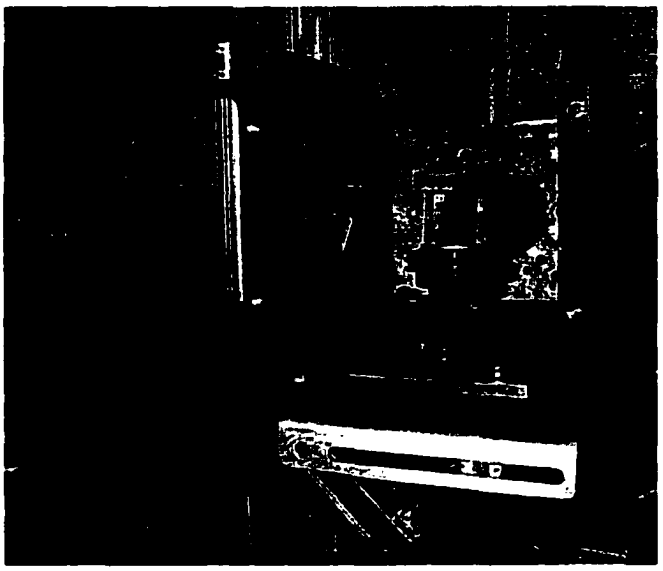

Figure 6-10 Beam splitter and liquid crystal retarder.

The beam-splitter and the retarder (Figure 6-10) are placed between the laser source and the laser beam focus lens. They are used to regulate the laser power. The beam-splitter is a perfect cube which consists of two right angle prisms carefully cemented together to minimize wavefront distortion. The hypotenuse of one of the prisms is coated with a multilayer dielectric polarizing beamsplitter coating optimized for a specific laser wavelength. In a polarizing cube beam-splitter, an unpolarized beam is split into two orthogonal linearly polarized components. P-polarized light is transmitted, and S-polarized light is reflected. The retarder is an optical device that resolves a light wave into two orthogonal linear polarization components and produces a phase shift between them. The retarder consists of a liquid crystal plate and can be considered as electrically

variable waveplates. Retardance is altered by applying a variable, low voltage waveform on the retarder. Thus, one can regulate the laser power by adjusting the voltage applied on the retarder.

A computer (Macintosh G3, made by Apple) with LabView installed is needed in this work. The interface card, PCI-1200 data acquisition card, is used to connect the computer and other hardwares listed above. With the interface card, the computer can communicate with other hardwares listed above. Through the computer, one can apply a laser beam with desired values of power incident on the substrate inside the reaction chamber.

6.3 Experimental Procedures

In this work, experiments are carried out at room temperature. Before LCVD processing, all experimental components should be connected as seen in Figure 6-7. During the process, the gas pressure inside the reactor should be maintained at 15 psi (pound per square inch) and the laser power applied on the substrate should be changed with time. The function of laser power versus time is obtained from the calculation of the numerical model in chapter five. The function is input into the computer and the computer automatically regulates the laser power applied on the substrate. The beam width ω_0 is adjusted manually when necessary. The experimental procedures involve the following: calibrating laser power, locating the focus point of the focused laser beam, loading the precursor gas, processing the LCVD reaction, taking pictures by SEM (AMRAY 1830) and collecting data from the pictures of rods. Each procedure is described in detail as follows.

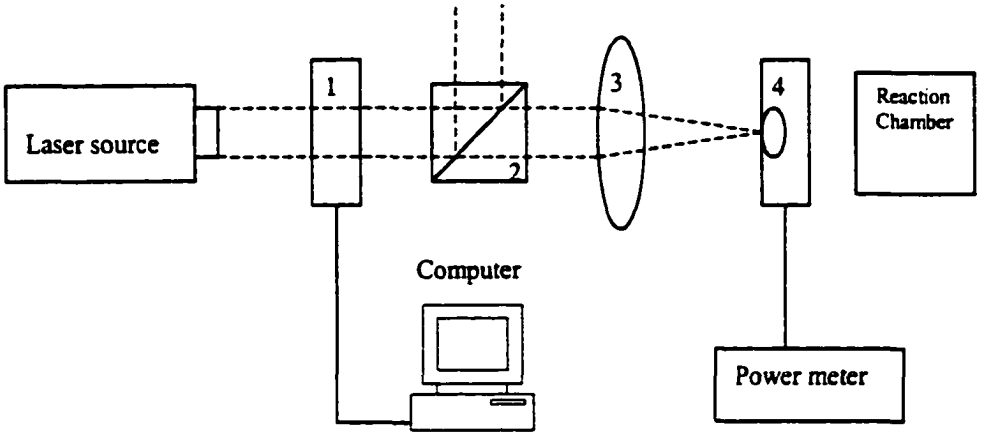

Figure 6-11 Experimental setup for calibration of laser power.
(1) LC retarder; (2) Beam splitter; (3) Focus lens;
(4) Thermopile detector.

6.3.1 Calibration of the Laser Power Output

The purpose of calibration of laser power is to match the value of the knob on the front panel on the computer with the actual laser power incident on the substrate inside the reaction chamber. Thus, after calibration, one can control the laser power of a laser beam delivered to the substrate through the computer.

Figure 6-11 shows the experimental setup for calibration of laser power. Laser beam from the laser source goes through the liquid crystal retarder, beam splitter. After it is focused by the optical lens, the laser beam is collected by the thermopile detector which is connected to a power meter. The power of the laser beam can be read from the power meter. The LC retarder is connected to the computer with Labview installed. The computer can change the laser power of the laser beam collected by the thermopile detector by varying the voltage applied on the LC retarder. The following steps are needed to calibrate the laser power.

(1). Connect each experimental component as in Figure 6-11.

(2). Turn the knob (Figure 6-8) to the maximum and turn the laser. The power meter displays the power of the laser beam. Adjust the laser power from the control panel of the laser source until the reading of the power meter is 2.00 W. Thus, the range of the laser power that can be regulated from the front panel on the computer is 0-2.00 Watt, which is the required range in this work.

(3). Turn the knob to the minimum. The power meter should display 0. Then turn the knob until the reading is 0.05W on the power meter, record the value on the knob. Adjust the knob to increment the power reading by 0.05 W until it reaches the maximum of 2.00 W. Record the value on the knob each time.

(4). Input the above data into the computer to obtain a calibration relationship between the laser power delivered to the thermopile detector Vs the values on the knob in the computer.

(5). The calibration relationship is recognized by the computer; then, the knob is rescaled so that the number dialed on the knob is exactly the number of laser power (in Watt) delivered to the thermopile detector.

(6). Remove the thermopile detector so that the laser beam can directly incident on the substrate inside the reaction chamber.

After going through the above steps, one can obtain the desired laser power (between 0-2.00 Watt) delivered to the substrate by just dialing the knob on the computer.

6.3.2 Locating the Focal Point of a Focused Laser Beam

Before the precursor gas methane is loaded into the reaction chamber, the focus point on the substrate must be located precisely to get accurate experimental results. If the laser beam is not focused exactly at the focus point on the substrate, a more intense laser power than necessary must be provided to obtain the threshold temperature on the substrate. In this case, inaccurate results are obtained.

As in system setup (Figure 6-1), when the laser beam is incident on the substrate, the reflected laser light by the substrate can be observed from the CRT monitor. One can move the XYZ-stage back and forth to find the focus point. Once the focus point is located, the temperature at that point increases rapidly until it reaches a certain level that makes that point glow. In this case, one can see an intense, glowing spot on the substrate through the monitor. To locate the focus point precisely, an optical filter must be placed between the CCD Camera and the observation window of the reactor. The glow releases radiation whose wavelength is much different from that of the reflected laser light. The filter filters out the reflected laser light and allows only the glowing radiation to pass through. Thus, once the focus point is located, one can clearly observe a small, glowing spot on the monitor. The following steps are needed to locate the focus point.

(1). Connect each experimental component as in Figure 6-7. Place the focus lens at about 100 mm away from the substrate.

(2). Turn on the laser. After calibration of the laser power, adjust the knob on the computer to get a laser beam with the desired power delivered to the substrate inside the reaction chamber.

(3). Adjust the XYZ-stage up and down until the reflected laser light can be observed on the monitor. Place the optical filter and move the XYZ-stage back and forth until an intense, clear glowing small spot appears on the substrate on the monitor.

In this work, the deposition reaction always takes place at the focus point, which requires adjusting the XYZ-stage backward as the rod grows. On the monitor, one must keep the same intensity and the same size of the spot as one moves the stage backward. This insures that the focus point is always at the tip of the rod as the rod grows.

6.3.3 Leak Checking and Loading of the Precursor Gas

Before the reactor is loaded with a precursor gas, the system is leak-checked by the helium leak detector (Figure 6-5b). In this system, a leak rate less than 10^{-4} torr is required. Leak-check ensures that the system is leak-free and maintains the pressure of the gas in the reactor during LCVD reaction.

The gas source used in this work is methane CH_4. Loading the precursor CH_4 requires going through the following steps:

(1). After calibrating the laser power, locating the focus point on the substrate and leak checking the system, turn the vacuum pump on to suck out air inside the reactor.

(2). Open the valve on top of the source cylinder to introduce methane into the reactor through the tube.

(3). Shut off the valve as the pressure in the reactor reaches 15 psi (pound per square inch). The pressure can be read from the pressure gauge.

6.3.4 LCVD Reaction Process

After the above procedures are completed, the laser is turned on and the laser beam is focused on the substrate in the reactor. The deposition reaction (expression 6.1)

$$CH_4 \Rightarrow C\downarrow + 2H_2\uparrow \qquad (6.1)$$

is induced by the laser. The carbon C is deposited as solid (rods) and the by-product gas hydrogen H_2 is exhausted from the system after the process. After procedure 6.3.3 is completed, processing the LCVD reaction requires the following steps.

(1). Input the function of laser power versus time into the computer. The function is calculated from the numerical model in chapter five. Turn on the laser, and at the same time press the 'run' button at the front panel on the computer. The desired laser power is applied on the substrate over time.

(2). Move the XYZ-stage backwards as the rod is growing to keep the focus point on the tip of the rod.

(3). When growth of the rod is completed, shut off the laser and turn the XYZ-state a bit in the X- or Y- direction to start growing another rod by repeating step (1) and (2).

(4). After a desired number of rods are grown, shut off the laser and vacuum the reactor to exhaust the left methane and the by-product gas H_2. Then, take out the substrate and take pictures of the rods using SEM (scanning electron microscopy).

6.3.5 Photography of Grown Rods by SEM

The rods grown in procedure 6.3.4 are sent to the SEM lab (Figure 6-12) to take SEM photos of each rod. These photos can provide accurate measures of the length, diameter and shape of a rod.

Figure 6-12 Lab for SEM (AMRAY 1830).

CHAPTER SEVEN

RESULTS AND DISCUSSION

In this chapter, both model results and experimental results are presented. By comparing these results, the model constructed in this work for growth of cylindrical rods is verified. Ways to further improve the model are investigated, based on the experimental results.

Table 7.1 Parameters for the deposition of amorphous carbon from CH_4 onto a graphite substrate[27, 46].

$E_a = 1.82004 \times 10^5$ (J / mole)
$R = 8.314$ (J / mole K)
$K_o = 2.37 \times 10^4$ (mm / s)
$k_d = 1.65$ (W / mm K)
$k_s = 1.7 \times 10^{-3}$ (W / mm K)
$T_\infty = 300$ (K)
$\omega = 0.01$ (mm)
$k_{gas} = 0.001$
$Nu = 0.36$
$\Lambda = 1$

7.1 Results From Model Calculations

In this work, all calculations are conducted by computer programs which are written by the author in *C++*. To demonstrate the applicability of this model and numerical procedure, a cylindrical rod growth is investigated by depositing amorphous

carbon, from methane CH_4, onto a graphite substrate. The material parameters used in the model are listed in Table 7.1[27, 46]. The geometry parameters for a cylindrical rod are pre-specified as in Table 7.2. These parameters are carefully selected to make calculation reasonable.

Table 7.2 The pre-specified geometry parameters for the calculations.

R = 0.04 (mm),	radius of cylindrical rod
$tipr$ = 0.015 (mm),	radius at the rod tip
h_p = 0.02 (mm),	the height of the parabolic portion of the rod
a = 0.002 (mm),	distance between adjacent layers
Δt = 0.002 (s),	time interval for growth of a

Based on the parameters listed in Table 7.1 and Table 7.2, numerical simulation was obtained for a cylindrical rod growth within the length of 0.6 mm. The required temperature distribution $\mathbf{T}_d^r$ for growth of a cylindrical rod is calculated from steps 1-2 in section 5.5 of chapter five. The results are shown in Table 7.3.

The temperature distribution in Table 7.3 is on the parabolic portion of the rod (top part of the rod). No matter how long the rod length is, the shape of the rod top is fixed. As such, the temperature distribution $\mathbf{T}_d^r$ is dependent on the geometry parameters listed in Table 7.2 and is independent of the rod length. Once those parameters are pre-specified, $\mathbf{T}_d^r$ is calculated and it is fixed. However, the temperature distribution $\mathbf{T}_d$ on the parabolic portion calculated from the heat equations is dependent on the rod length. At a certain layer with a certain rod length, $\mathbf{T}_d$ is calculated with the estimated laser

power and the least square method is applied to minimize the sum of squared errors between $\mathbf{T}_d^r$ and $\mathbf{T}_d$, so that the optimum laser power is obtained.

Table 7.3 The required temperature distribution $\mathbf{T}_d^r$ for growth of a cylindrical rod with $M = 10$.

i	$(T_d)_i$
1	1708.81
2	1712.17
3	1715.75
4	1719.55
5	1723.6
6	1727.94
7	1732.61
8	1737.66
9	1743.18
10	1749.23
11	1768.87

Table 7.4 (a)-(f) lists the temperatures at all grid points on the parabolic portion calculated from the heat equations for different rod lengths under their corresponding optimized laser power. Also, the sum of squares of error S_e at each length is listed. For comparison, the required temperatures at corresponding grid points are also listed in this table. One can see that the required temperature distribution is the same for each rod length.

Figure 7-1 (a)-(f) shows comparisons between the required temperature distribution and the calculated temperature distribution under optimum laser power intensity for different rod lengths. From these plots and Table 7.4, one can see that the longer the rod grows, the closer the temperature distribution (calculated from the heat

conduct equations) is to the required temperature distribution. One may also notice that the biggest temperature deviations occur at the last two grid points, the tenth and eleventh

Table 7.4 Temperature distribution calculated from the heat equations at different rod lengths.

	i	x_i	$(T_d')_i$	$(T_d)_i$
(a)	1	0.080	1708.81	1709.04
	2	0.082	1712.17	1711.81
L = 0.1 (mm)	3	0.084	1715.75	1714.84
	4	0.086	1719.55	1718.21
P_o= 0.9551 (W)	5	0.088	1723.60	1721.99
	6	0.090	1727.94	1726.31
S_e = 40.97	7	0.092	1732.61	1731.33
	8	0.094	1737.66	1737.32
	9	0.096	1743.18	1744.77
	10	0.098	1749.23	1754.59
	11	0.100	1768.87	1769.00
	i	x_i	$(T_d')_i$	$(T_d)_i$
(b)	1	0.180	1708.81	1710.58
	2	0.182	1712.17	1713.15
L = 0.2 (mm)	3	0.184	1715.75	1715.98
	4	0.186	1719.55	1719.11
P_o= 0.8971 (W)	5	0.188	1723.60	1722.63
	6	0.190	1727.94	1726.65
S_e = 29.78	7	0.192	1732.61	1731.31
	8	0.194	1737.66	1736.89
	9	0.196	1743.18	1743.81
	10	0.198	1749.23	1752.94
	11	0.200	1768.87	1766.35

Table 7.4 Continued.

	i	x_i	$(T_d')_i$	$(T_d)_i$
(c)	1	0.280	1708.81	1710.05
	2	0.282	1712.17	1712.69
L = 0.3 (mm)	3	0.284	1715.75	1715.59
	4	0.286	1719.55	1718.81
P_o= 0.8193 (W)	5	0.288	1723.60	1722.42
	6	0.290	1727.94	1726.53
S_e = 29.64	7	0.292	1732.61	1731.32
	8	0.294	1737.66	1737.04
	9	0.296	1743.18	1744.14
	10	0.298	1749.23	1753.51
	11	0.300	1768.87	1767.26
	i	x_i	$(T_d')_i$	$(T_d)_i$
(d)	1	0.380	1708.81	1710.26
	2	0.382	1712.17	1712.87
L = 0.4 (mm)	3	0.384	1715.75	1715.74
	4	0.386	1719.55	1718.93
P_o= 0.7524 (W)	5	0.388	1723.60	1722.50
	6	0.390	1727.94	1726.58
S_e = 29.34	7	0.392	1732.61	1731.32
	8	0.394	1737.66	1736.98
	9	0.396	1743.18	1744.02
	10	0.398	1749.23	1753.29
	11	0.400	1768.87	1766.90
	i	x_i	$(T_d')_i$	$(T_d)_i$
(e)	1	0.480	1708.81	1710.28
	2	0.482	1712.17	1712.89
L = 0.5 (mm)	3	0.484	1715.75	1715.76
	4	0.486	1719.55	1718.94
P_o= 0.6838 (W)	5	0.488	1723.60	1722.51
	6	0.490	1727.94	1726.58
S_e = 29.19	7	0.492	1732.61	1731.32
	8	0.494	1737.66	1736.98
	9	0.496	1743.18	1744.00
	10	0.498	1749.23	1753.26
	11	0.500	1768.87	1766.86

Table 7.4 Continued.

	i	x_i	$(T_d')_i$	$(T_d)_i$
(f)	1	0.580	1708.81	1710.31
	2	0.582	1712.17	1712.92
L = 0.6 (mm)	3	0.584	1715.75	1715.78
	4	0.586	1719.55	1718.96
P_o= 0.6153 (W)	5	0.588	1723.60	1722.53
	6	0.590	1727.94	1726.59
S_e = 29.18	7	0.592	1732.61	1731.32
	8	0.594	1737.66	1736.97
	9	0.596	1743.18	1743.98
	10	0.598	1749.23	1753.23
	11	0.600	1768.87	1766.81

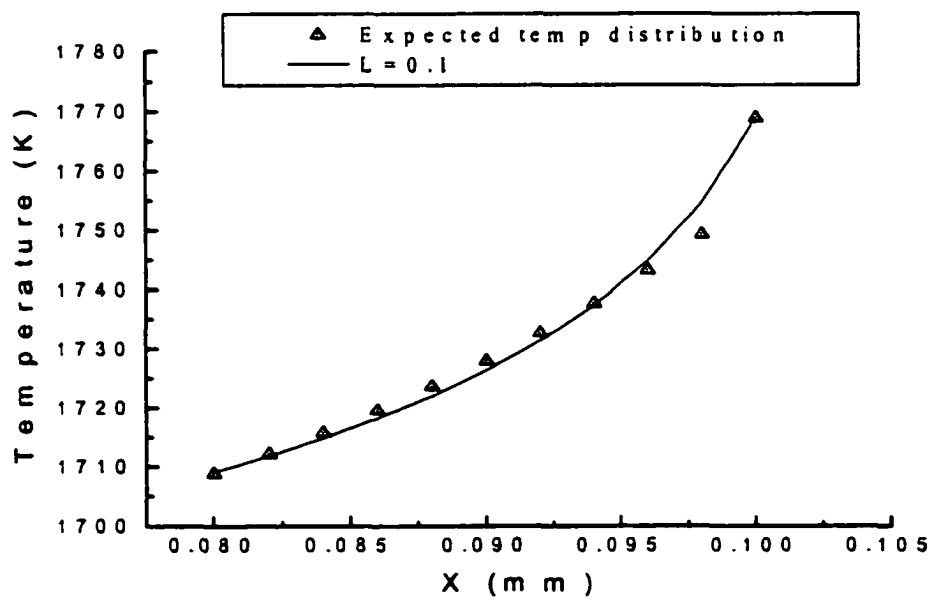

Figure 7-1(a) Comparison between the required and calculated (from the heat equations) temperature distribution on parabolic portion of the rod with L= 0.1 mm.

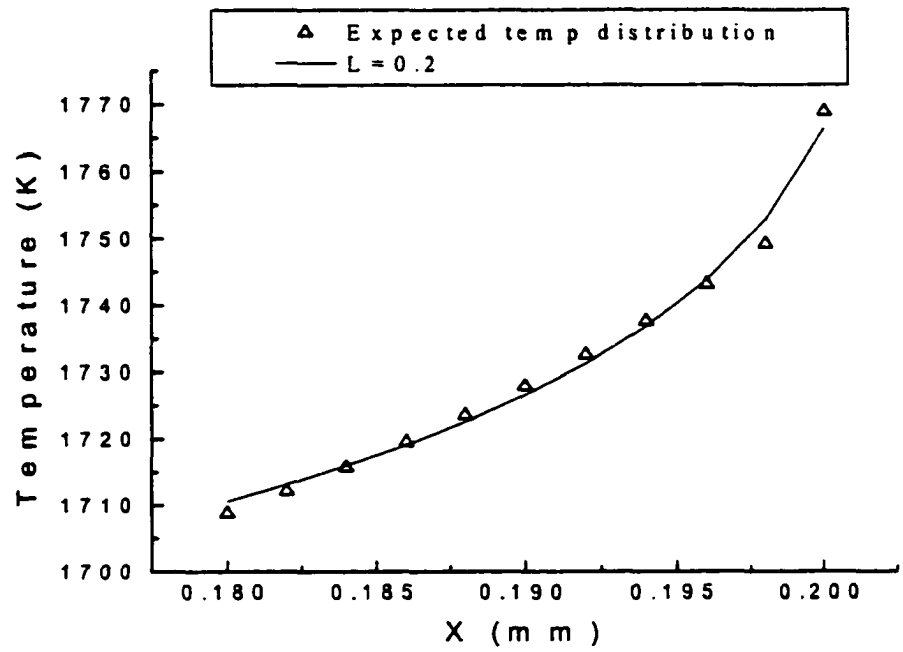

Figure 7.1(b) Comparison between the required and calculated (from the heat equations) temperature distribution on parabolic portion of the rod with L= 0.2 mm.

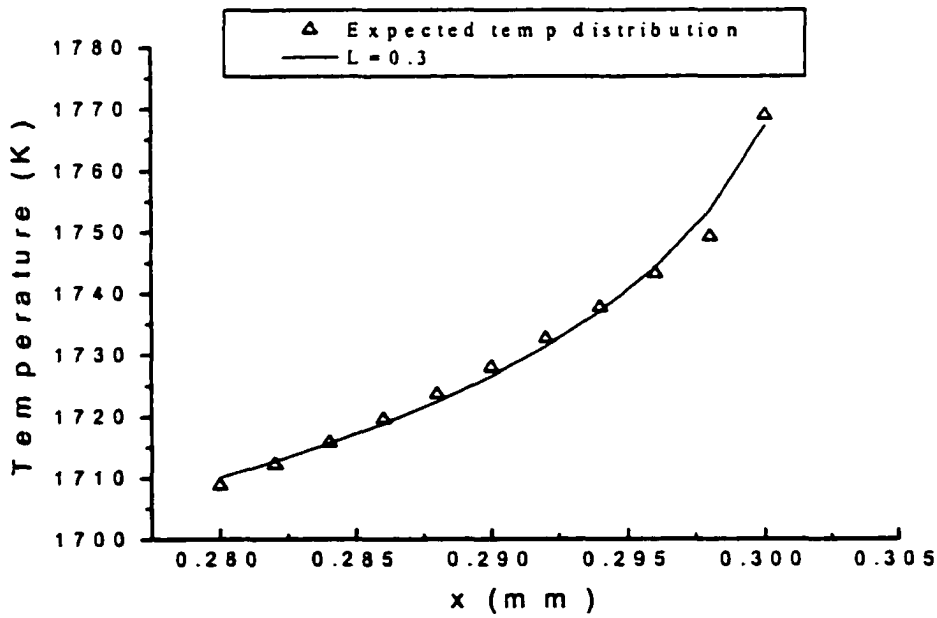

Figure 7.1(c) Comparison between the required and calculated (from the heat equations) temperature distribution on parabolic portion of the rod with L= 0.3 mm.

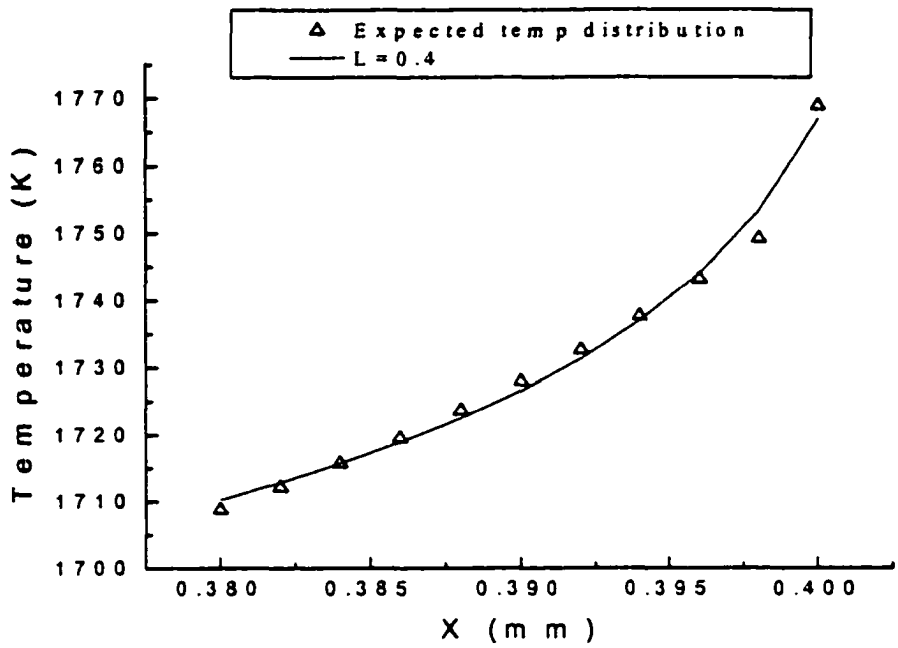

Figure 7.1(d) Comparison between the required and calculated (from the heat equations) temperature distribution on parabolic portion of the rod with L= 0.4 mm.

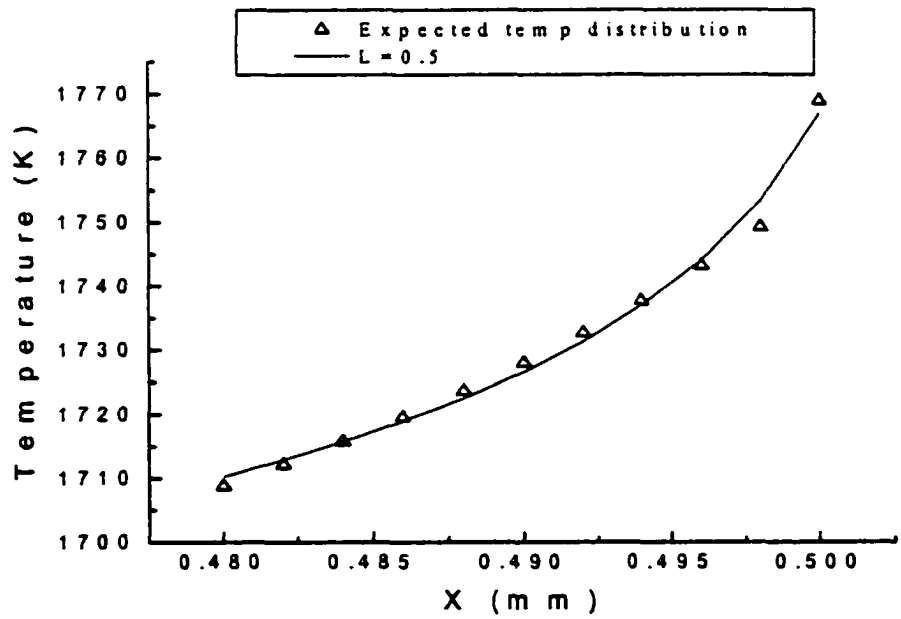

Figure 7.1(e) Comparison between the required and calculated (from the heat equations) temperature distribution on parabolic portion of the rod with L= 0.5 mm.

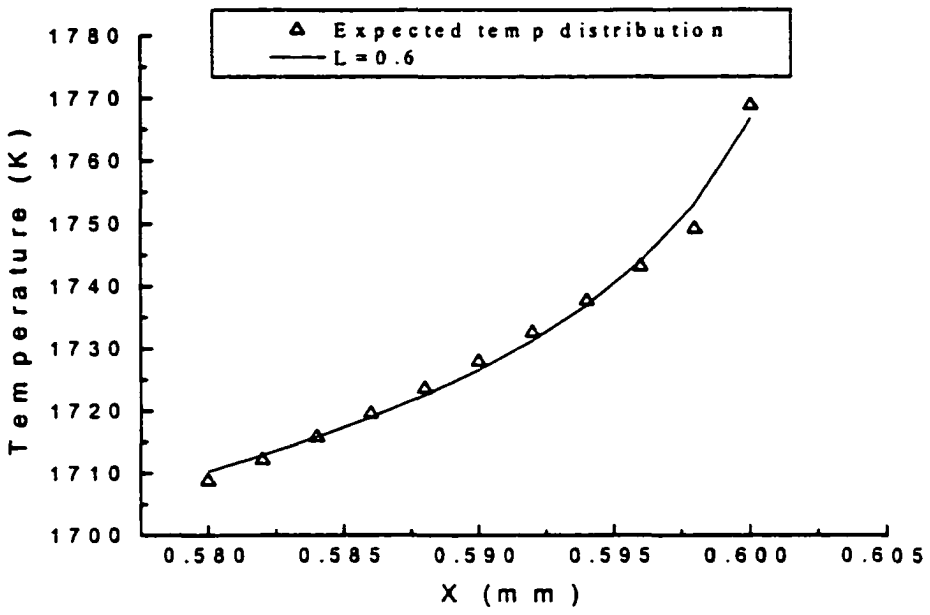

Figure 7.1(f) Comparison between the required and calculated (from the heat equations) temperature distribution on parabolic portion of the rod with L= 0.6 mm.

grid points. This is because the eleventh point is the critical point at which the rod shape turns from parabolic to flat.

It is worth mentioning that for a certain rod length, the heat equations give the temperature distribution on the whole surface of deposit, from the bottom to the tip of the rod, through step 3 in section 5.5 of chapter five. However, only the temperature distribution on the parabolic portion is chosen to compare with the required temperature distribution, and to apply the least square method in order to obtain the optimum laser power intensity by using step 4-8 in section 5.5 of chapter five.

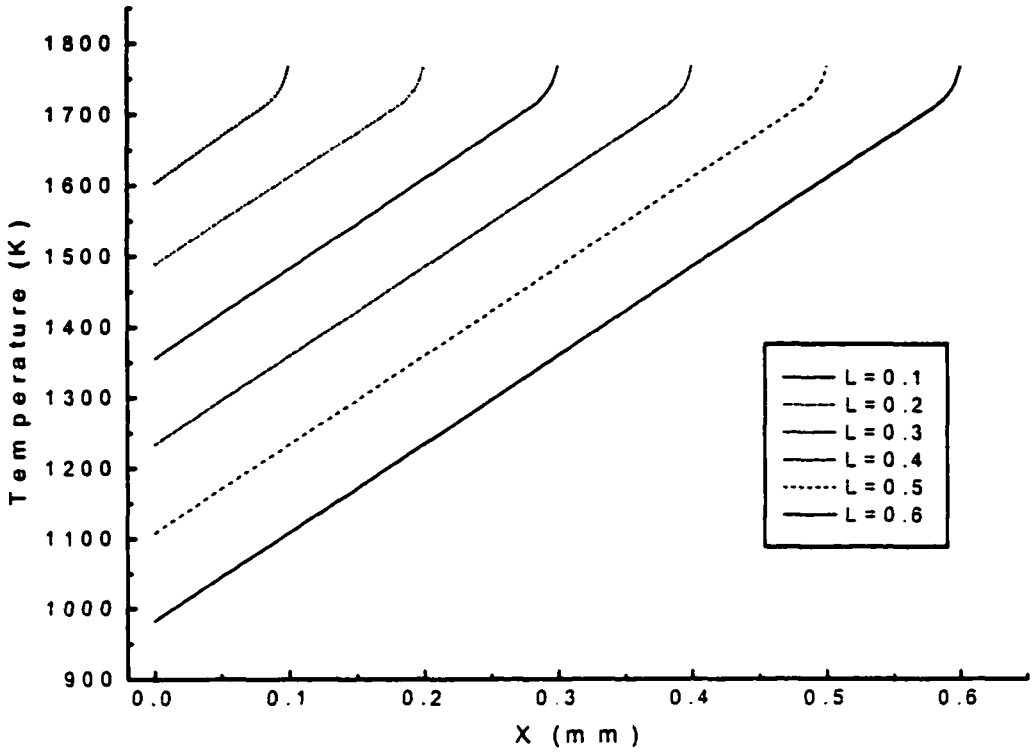

Figure 7-2 Temperature distributions for different rod lengths, calculated from the heat equations.

Figure 7-2 shows the temperature distributions for different rod lengths or heights (from 0.1-0.6 mm), calculated from the heat conduction equations under optimum laser powers. It is seen that short rods have higher base temperatures than long rods. This is because for short rods, the base of the rod is closer to the rod tip which has the highest temperature. Also, it is seen from Figure 7-2 that for a rod with a certain length, the temperature increases with an increase of the height of the rod. It is noticed that each curve in this figure consists of a linear section and non-linear section. The linear section is related to the straight portion of the rod and the non-linear section is related to the parabolic portion of the rod.

is related to the straight portion of the rod and the non-linear section is related to the parabolic portion of the rod.

The optimum laser power over rod length and over time is obtained by step 9 and step 10 in section 5.5 of chapter five. Results are shown in Figure 7-3 and Figure 7-4. Data for the two plots can be found in the appendix part of this dissertation. In Figure 7-3, it is seen that in order to grow a cylindrical rod, the laser power must be decreased (almost linearly) as the rod grows. At the early stage of growth (the rod is short), the heat flux flows readily from the tip to the bottom of the rod and then to the conductive sink (substrate). Thus, the laser power needs to be large enough in order to maintain close agreement between rod temperature $(T_d)_i$ and the required growth temperature, $(T_d^r)_i$ as seen in Table 7.3. As the rod grows, it becomes harder for the heat to flow from the tip to the sink, causing the temperature at the top of the rod to increase. As such, less laser power is needed to keep the temperature in agreement with the required temperature, $(T_d^r)_i$. It is interesting to note that the optimum laser power increases with the rod length at the beginning of growth. This phenomenon may be attributed to the relatively high errors at the beginning of growth. This point will be discussed in more details later in this chapter. For Figure 7-4, since there is a linear relationship between the rod length and the process time, the contour of the curve should be the same as the one in Figure 7-3.

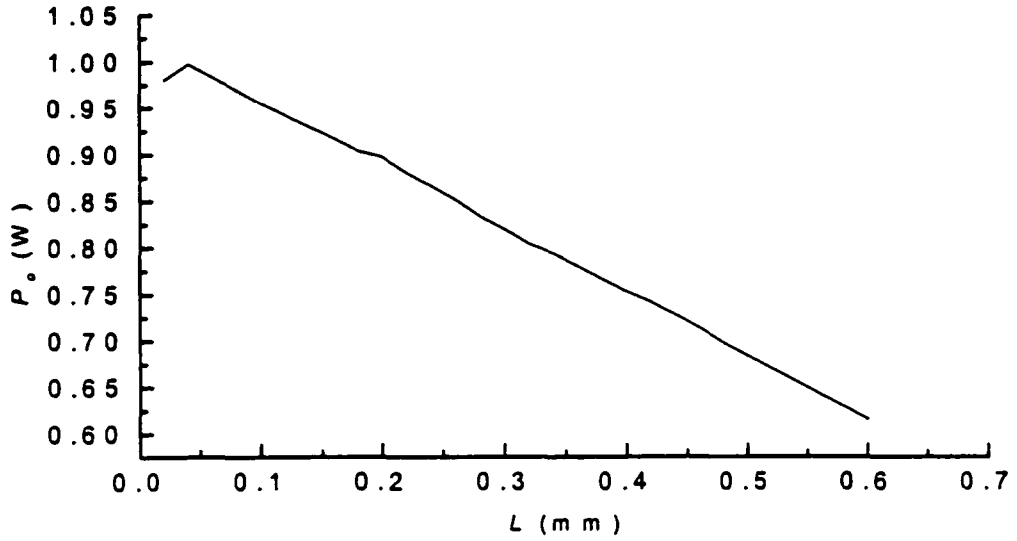

Figure 7-3 Optimum laser power (calculated from the model) as a function of rod length.

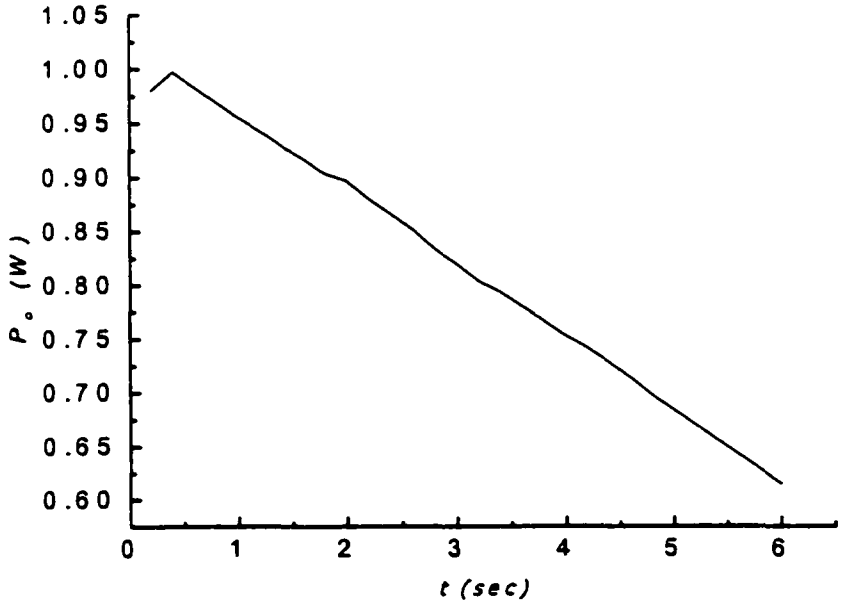

Figure 7-4 Optimum laser power (calculated from the model) as a function of the processing time.

The sum of squared deviations between required and calculated (based on the heat conduction equations) temperatures as a function of rod length is shown in Figure 7-5.

The data for this plot are presented in the appendix. It is seen from this figure that the errors are relatively high at the early stage of growth and decrease as the rod length increases up to a certain level after which the errors stabilize.

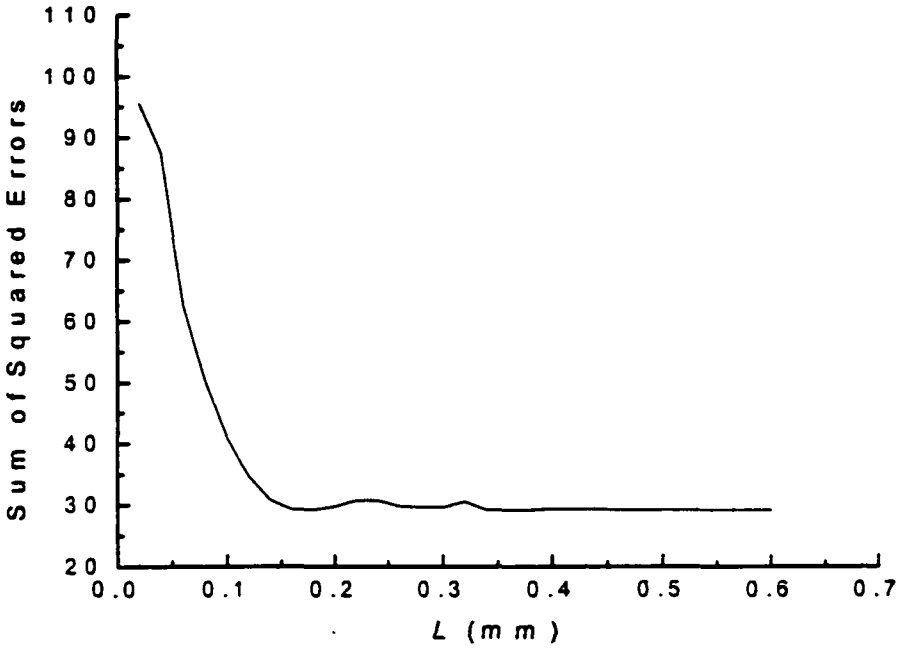

Figure 7-5 Sum of squared deviations between required and calculated temperature distributions as a function of rod length.

7.2 Experimental Results

In the experiments, the optimum laser power intensity P_o over time obtained from the model is input into the computer, and P_o is automatically adjusted by using the software LabView. The laser beam width is kept at 0.01 mm. Figure 7-6(a) shows the pre-specified geometry for cylindrical rods with different lengths, from 0.1 ~ 0.6 mm. Figure 7-6 (b) shows cylindrical rods with different lengths grown experimentally by using the optimum solution of P_o for each growth layer. It is seen that the experimental

results are close to the expected rod growth from the numerical model. Slight differences exist at the tip and at the bottom of the rod. The reason for the deviation at the tip is that the numerical model did not include gas diffusion (K_o is treated as a constant). From the experiments, it was found that the tip of the rod grows as a constant rate, while the edges grow at a kinetically limited rate. In the limit, when the concentration of precursor molecules cannot be replenished, the hottest region of the deposit (usually the tip) can be hindered in its growth while other portions are not, eventually leading to a crater deposit. The reason for the deviation at the bottom of the rod will be discussed later in this chapter.

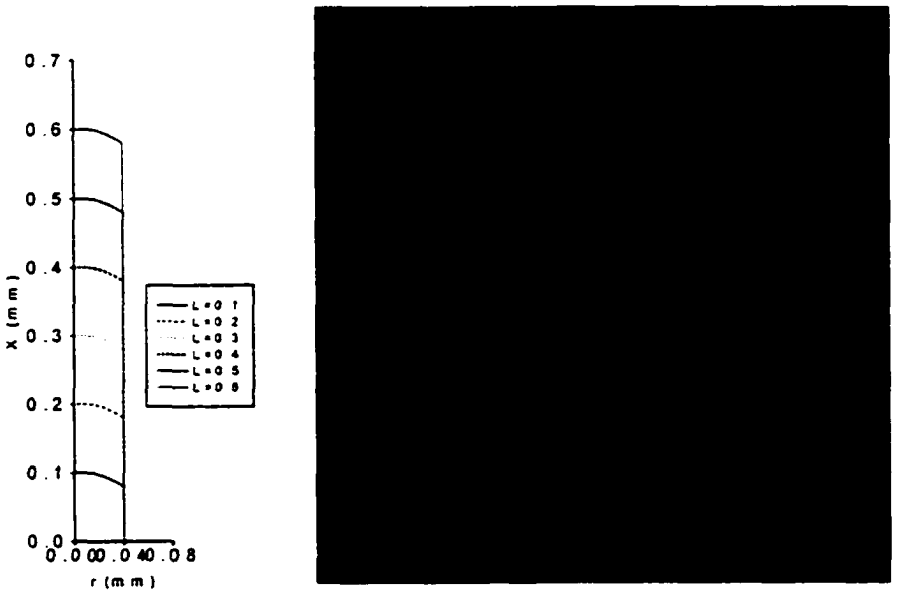

(a) (b)

Figure 7-6 Comparison between (a) the expected rod growth from the numerical model and (b) rod grown experimentally using optimum P_o.

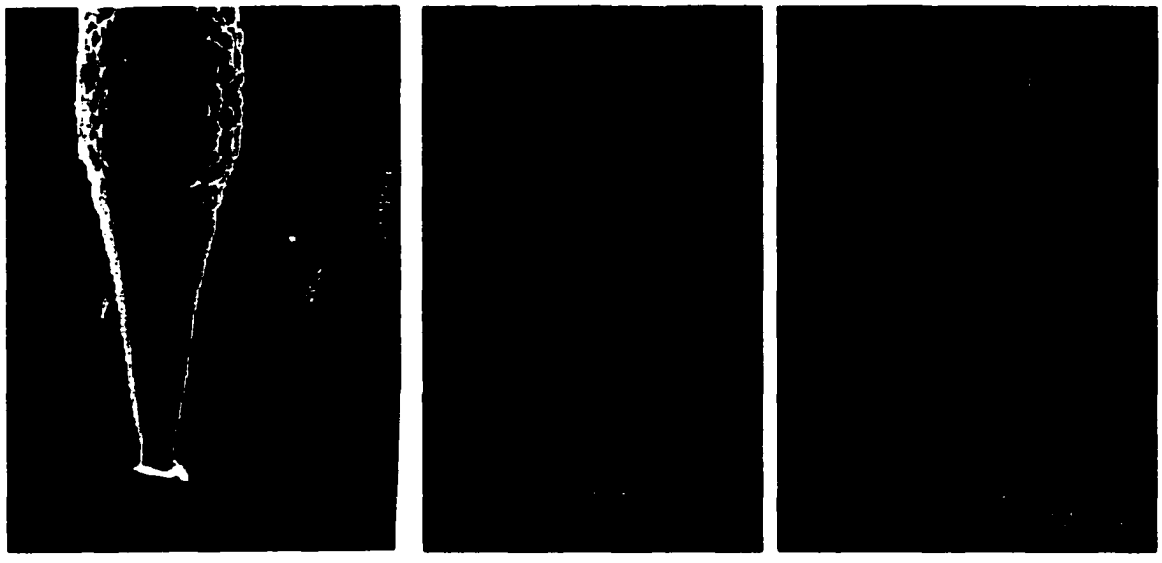

(a) (b) (c)

Figure 7-7 Rods grown with and without model optimization.
(a) A rod grow without model optimization, $P_o = 0.6$ W,
(b), (c) rods grown with model optimization.

Figure 7-7(a)~(b) show the comparison between rods grown without and with the benefit of the model: Figure 7-7(a) shows the shape of a rod grown under a constant laser power, $P_o = 0.6$ W, for each layer without the benefit of the model. On the other hand, Figure 7-7 (b,c) shows rod growth obtained by using the optimum P_o for each layer as obtained from the model. It is seen that a constant laser power, not adjusted for each layer, gave a cone shaped growth instead of the cylindrical shape that is intended. However, using the optimum laser powers from the model, the growth (Figure 7-7(b,c)) is close to being cylindrical in shape as planned.

Figure 7-8 gives the diameters of the rods in Figure 7-7(a), (b), (c) as a function of rod length. The rods in Figure 7-7(b), (c) (with diameter measurements in Figure 7-8) show some deviations from a cylindrical shape at the early stage of growth. These

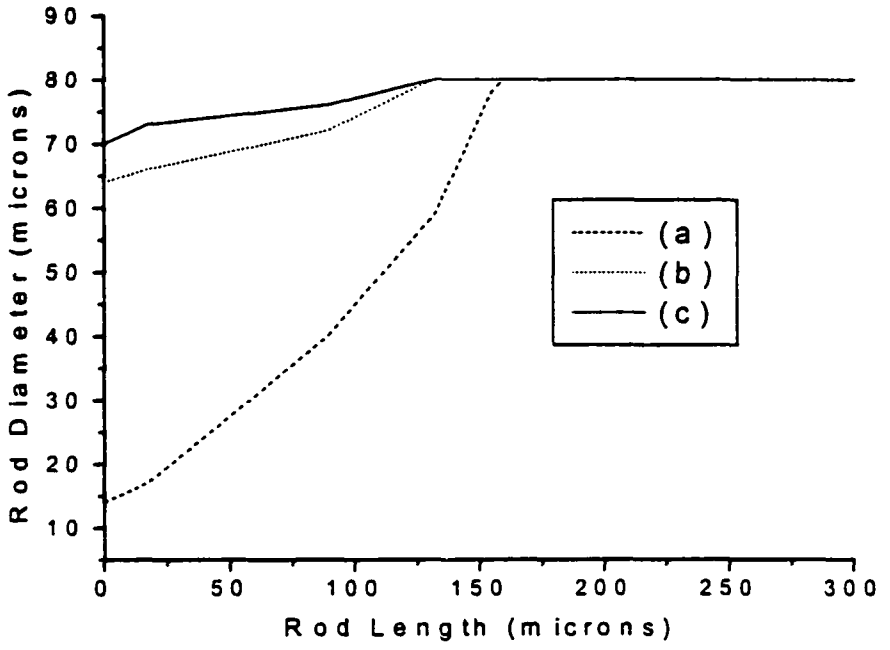

Figure 7-8 Rod diameter as a function of rod length for the three rods in Figure 7-7.

deviations are also reflected in Figure 7-1 (a)~(f) which present deviations between the temperature distribution T_d (calculated from the heat conduction equations) and the required temperature distribution T_d^r for various growth layers. Although the agreement between required and calculated (from the heat equations) temperatures is rather good, the discrepancy between the two is larger for the early growth than for later growth. This discrepancy is more readily seen when the sum of squared deviations between $(T_d)_i$ and $(T_d^r)_i$ is plotted as a function of rod length (Figure 7-5). It is seen from this figure that the sum of squared error is relatively large initially, then decreases and finally stabilizes as the rod length is longer than about 0.35 mm. These relatively large errors at the early stages of growth reflect the deviations from the cylindrical shape as shown in Figure 7-1 and 7-7. One reason for this deviation may be caused by the huge temperature gradient

from the substrate (about 300 K) to the top of the rod (1700 K ~ 1800 K) in the early growth of the rod. This huge temperature gradient makes it very difficult to match $(T_d)_i$ with $(T_d')_i$. The temperature gradient diminishes as the rod grows longer. This may explain why the sum of squares decreases as the rod grows. Figure 7-9 shows the comparison between $(T_d)_i$ and $(T_d')_i$ at the early stage of rod growth (L = 0.02 mm). It is seen that the deviation is much larger than in late growth of the rod (Figure 7-1 (a)~(f), L = 0.1 ~ 0.6 mm).

Another reason for the deviation may be caused by the fact that the temperature solution in Equation (3.16) was at steady state. This approximation may not be quite adequate at the beginning stage of growth.

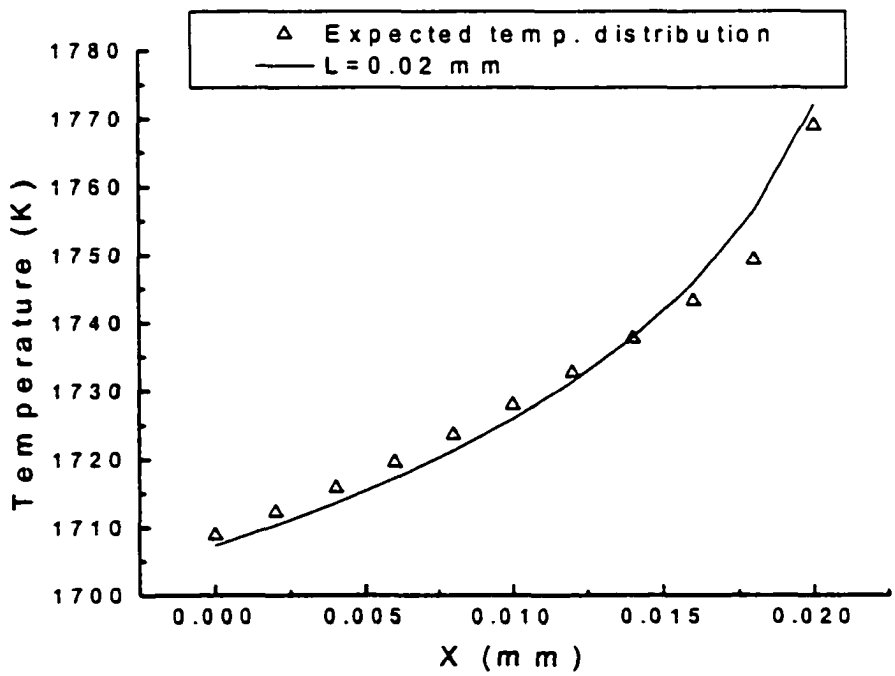

Figure 7-9 Deviation between $(T_d)_i$ and $(T_d')_i$ is much larger at the early growth stage than at the late growth stage(compare to Figure 7-1).

7.3 Conclusions

Conclusions drawn from this work can be stated as follows:

- An axis-symmetric numerical model for simulating cylindrical rod growth in three-dimensional kinetically-limited laser-induced chemical vapor deposition is developed using IHCP (inverse heat conduction problem) techniques.
- According to this model, two process parameters (power and beam width) can be predicted for growing a cylindrical rod. However, under current experimental conditions, only laser power can be controlled freely by the computer. Thus, laser power is the only parameter needed to be predicted over time to grow a cylindrical rod.
- The optimum laser power, P_o, over time as calculated by the model was used in the experiments to grow a cylindrical rod by depositing carbon from methane gas onto a graphite substrate.
- Experimental results showed that rod growth based on the optimum laser power over time was quite cylindrical in shape (Only a little deviation at the bottom of the rod). On the other hand, the rod was conical in shape when the laser power used was constant over time and not as predicted by the model.

7.4 Future Study

In order to improve this model and decrease deviations from the cylindrical shape, future studies need to address the following aspects:

- Using the unsteady state heat equation (instead of steady state) to calculate the rod surface temperature used in obtaining the optimum laser power over time.
- Optimizing both laser power and beam width, simultaneously.
- Heating the substrate before commencing deposition. This can efficiently decrease the temperature gradient from the bottom to the tip of the rod at the early stage of growth. Preliminary investigations with nickel deposits showed that heating the substrate, initially, before the commence of deposition reduced the errors at the early stages of growth.

APPENDIX

RESULTS FROM MODEL CALCULATION

AND SOURCE CODE

Table A.1 Temperature distributions for rods with different lengths (data for Figure 7-2, calculated from the heat equations).

x_i (mm)	$L = 0.1$ $(T_d)_i$ (K)	$L = 0.2$ $(T_d)_i$ (K)	$L = 0.3$ $(T_d)_i$ (K)	$L = 0.4$ $(T_d)_i$ (K)	$L = 0.5$ $(T_d)_i$ (K)	$L = 0.6$ $(T_d)_i$ (K)
0	1603.126	1488.791	1355.868	1233.805	1108.393	982.9142
0.002	1605.775	1491.258	1358.403	1236.319	1110.91	985.4336
0.004	1608.424	1493.725	1360.937	1238.833	1113.426	987.9530
0.006	1611.073	1496.191	1363.471	1241.346	1115.942	990.4723
0.008	1613.722	1498.658	1366.005	1243.86	1118.458	992.9916
0.010	1616.371	1501.125	1368.539	1246.374	1120.974	995.5108
0.012	1619.019	1503.592	1371.073	1248.887	1123.491	998.0299
0.014	1621.668	1506.058	1373.607	1251.401	1126.007	1000.549
0.016	1624.317	1508.525	1376.141	1253.915	1128.523	1003.068
0.018	1626.965	1510.991	1378.675	1256.428	1131.038	1005.587
0.02o	1629.614	1513.458	1381.209	1258.942	1133.554	1008.106
0.022	1632.262	1515.924	1383.743	1261.455	1136.070	1010.625
0.024	1634.911	1518.391	1386.276	1263.968	1138.586	1013.144
0.026	1637.559	1520.857	1388.810	1266.481	1141.101	1015.662
0.028	1640.207	1523.323	1391.344	1268.995	1143.617	1018.181
0.030	1642.855	1525.789	1393.877	1271.508	1146.133	1020.700
0.032	1645.504	1528.255	1396.410	1274.021	1148.648	1023.218
0.034	1648.152	1530.721	1398.944	1276.534	1151.163	1025.737
0.036	1650.800	1533.188	1401.477	1279.047	1153.679	1028.255
0.038	1653.448	1535.653	1404.010	1281.56	1156.194	1030.773
0.040	1656.096	1538.119	1406.544	1284.072	1158.709	1033.292
0.042	1658.743	1540.585	1409.077	1286.585	1161.225	1035.810
0.044	1661.391	1543.051	1411.610	1289.098	1163.740	1038.328
0.046	1664.039	1545.517	1414.143	1291.611	1166.255	1040.846
0.048	1666.686	1547.982	1416.676	1294.123	1168.770	1043.364
0.050	1669.334	1550.448	1419.209	1296.636	1171.285	1045.882
0.052	1671.982	1552.913	1421.742	1299.148	1173.800	1048.400
0.054	1674.629	1555.379	1424.274	1301.661	1176.314	1050.918
0.056	1677.276	1557.844	1426.807	1304.173	1178.829	1053.436
0.058	1679.924	1560.310	1429.340	1306.685	1181.344	1055.954
0.060	1682.571	1562.775	1431.872	1309.197	1183.859	1058.471
0.062	1685.218	1565.240	1434.405	1311.710	1186.373	1060.989
0.064	1687.865	1567.705	1436.937	1314.222	1188.888	1063.507
0.066	1690.512	1570.171	1439.470	1316.734	1191.402	1066.024
0.068	1693.159	1572.636	1442.002	1319.246	1193.916	1068.542
0.070	1695.806	1575.101	1444.535	1321.758	1196.431	1071.059
0.072	1698.453	1577.566	1447.067	1324.270	1198.945	1073.576
0.074	1701.100	1580.031	1449.599	1326.781	1201.459	1076.093
0.076	1703.747	1582.495	1452.131	1329.293	1203.973	1078.611
0.078	1706.394	1584.960	1454.663	1331.805	1206.487	1081.128

Table A.1 Continued.

0.080	1709.040	1587.425	1457.195	1334.316	1209.001	1083.645
0.082	1711.806	1589.889	1459.727	1336.828	1211.515	1086.162
0.084	1714.844	1592.354	1462.259	1339.339	1214.029	1088.679
0.086	1718.214	1594.819	1464.791	1341.851	1216.543	1091.196
0.088	1721.999	1597.283	1467.322	1344.362	1219.057	1093.712
0.090	1726.314	1599.747	1469.854	1346.873	1221.570	1096.229
0.092	1731.332	1602.212	1472.386	1349.385	1224.084	1098.746
0.094	1737.327	1604.676	1474.917	1351.896	1226.598	1101.262
0.096	1744.771	1607.140	1477.449	1354.407	1229.111	1103.779
0.098	1754.588	1609.604	1479.980	1356.918	1231.625	1106.295
0.100	1769.000	1612.069	1482.511	1359.429	1234.138	1108.812
0.102	--	1614.533	1485.043	1361.940	1236.651	1111.328
0.104		1616.997	1487.574	1364.451	1239.164	1113.844
0.106		1619.461	1490.105	1366.961	1241.678	1116.360
0.108		1621.924	1492.636	1369.472	1244.191	1118.877
0.110		1624.388	1495.167	1371.983	1246.704	1121.393
0.112		1626.852	1497.698	1374.493	1249.217	1123.909
0.114		1629.316	1500.229	1377.004	1251.730	1126.425
0.116		1631.779	1502.76	1379.514	1254.242	1128.940
0.118		1634.243	1505.291	1382.025	1256.755	1131.456
0.120		1636.706	1507.821	1384.535	1259.268	1133.972
0.122		1639.170	1510.352	1387.045	1261.781	1136.487
0.124		1641.633	1512.883	1389.555	1264.293	1139.003
0.126		1644.096	1515.413	1392.066	1266.806	1141.519
0.128		1646.559	1517.944	1394.576	1269.318	1144.034
0.130		1649.023	1520.474	1397.086	1271.830	1146.549
0.132		1651.486	1523.004	1399.595	1274.343	1149.065
0.134		1653.949	1525.534	1402.105	1276.855	1151.580
0.136		1656.412	1528.065	1404.615	1279.367	1154.095
0.138		1658.875	1530.595	1407.125	1281.879	1156.610
0.140		1661.338	1533.125	1409.634	1284.391	1159.125
0.142		1663.800	1535.655	1412.144	1286.903	1161.640
0.144		1666.263	1538.185	1414.654	1289.415	1164.155
0.146		1668.726	1540.714	1417.163	1291.927	1166.670
0.148		1671.188	1543.244	1419.672	1294.438	1169.184
0.150		1673.651	1545.774	1422.182	1296.950	1171.699
0.152		1676.113	1548.304	1424.691	1299.462	1174.213
0.154		1678.576	1550.833	1427.200	1301.973	1176.728
0.156		1681.038	1553.363	1429.709	1304.485	1179.242
0.158		1683.500	1555.892	1432.218	1306.996	1181.757
0.160		1685.962	1558.421	1434.727	1309.507	1184.271
0.162		1688.425	1560.951	1437.236	1312.019	1186.785
0.164		1690.887	1563.480	1439.745	1314.530	1189.299
0.166		1693.349	1566.009	1442.254	1317.041	1191.813

Table A.1 Continued.

0.168	1695.811	1568.538	1444.762	1319.552	1194.327
0.170	1698.273	1571.067	1447.271	1322.063	1196.841
0.172	1700.734	1573.596	1449.78	1324.574	1199.355
0.174	1703.196	1576.125	1452.288	1327.085	1201.869
0.176	1705.658	1578.654	1454.797	1329.595	1204.383
0.178	1708.119	1581.183	1457.305	1332.106	1206.896
0.180	1710.581	1583.711	1459.813	1334.617	1209.41
0.182	1713.153	1586.240	1462.321	1337.127	1211.923
0.184	1715.979	1588.769	1464.829	1339.638	1214.436
0.186	1719.113	1591.297	1467.338	1342.148	1216.95
0.188	1722.634	1593.825	1469.846	1344.658	1219.463
0.190	1726.647	1596.354	1472.353	1347.168	1221.976
0.192	1731.314	1598.882	1474.861	1349.679	1224.489
0.194	1736.889	1601.41	1477.369	1352.189	1227.002
0.196	1743.813	1603.938	1479.877	1354.699	1229.515
0.198	1752.943	1606.466	1482.384	1357.209	1232.028
0.200	1766.347	1608.994	1484.892	1359.718	1234.541
0.202	--	1611.522	1487.399	1362.228	1237.053
0.204		1614.050	1489.907	1364.738	1239.566
0.206		1616.578	1492.414	1367.248	1242.079
0.208		1619.105	1494.921	1369.757	1244.591
0.210		1621.633	1497.429	1372.267	1247.103
0.212		1624.161	1499.936	1374.776	1249.616
0.214		1626.688	1502.443	1377.285	1252.128
0.216		1629.216	1504.950	1379.795	1254.640
0.218		1631.743	1507.457	1382.304	1257.152
0.220		1634.270	1509.964	1384.813	1259.664
0.222		1636.797	1512.470	1387.322	1262.176
0.224		1639.324	1514.977	1389.831	1264.688
0.226		1641.851	1517.484	1392.340	1267.199
0.228		1644.378	1519.990	1394.849	1269.711
0.230		1646.905	1522.497	1397.357	1272.223
0.232		1649.432	1525.003	1399.866	1274.734
0.234		1651.959	1527.509	1402.375	1277.246
0.236		1654.486	1530.016	1404.883	1279.757
0.238		1657.012	1532.522	1407.391	1282.268
0.240		1659.539	1535.028	1409.900	1284.779
0.242		1662.065	1537.534	1412.408	1287.290
0.244		1664.592	1540.040	1414.916	1289.801
0.246		1667.118	1542.546	1417.424	1292.312
0.248		1669.644	1545.051	1419.932	1294.823
0.250		1672.170	1547.557	1422.440	1297.334
0.252		1674.696	1550.063	1424.948	1299.844
0.254		1677.222	1552.568	1427.456	1302.355

Table A.1 Continued.

0.256	1679.748	1555.074	1429.964	1304.866
0.258	1682.274	1557.579	1432.471	1307.376
0.260	1684.800	1560.085	1434.979	1309.886
0.262	1687.326	1562.590	1437.486	1312.397
0.264	1689.851	1565.095	1439.994	1314.907
0.266	1692.377	1567.600	1442.501	1317.417
0.268	1694.902	1570.105	1445.008	1319.927
0.270	1697.428	1572.610	1447.515	1322.437
0.272	1699.953	1575.115	1450.022	1324.947
0.274	1702.478	1577.620	1452.529	1327.456
0.276	1705.004	1580.124	1455.036	1329.966
0.278	1707.529	1582.629	1457.543	1332.475
0.280	1710.054	1585.134	1460.050	1334.985
0.282	1712.692	1587.638	1462.556	1337.494
0.284	1715.590	1590.143	1465.063	1340.004
0.286	1718.806	1592.647	1467.570	1342.513
0.288	1722.417	1595.151	1470.076	1345.022
0.290	1726.534	1597.655	1472.582	1347.531
0.292	1731.321	1600.159	1475.089	1350.040
0.294	1737.040	1602.663	1477.595	1352.549
0.296	1744.142	1605.167	1480.101	1355.058
0.298	1753.507	1607.671	1482.607	1357.566
0.300	1767.256	1610.175	1485.113	1360.075
0.302	--	1612.679	1487.619	1362.584
0.304		1615.182	1490.124	1365.092
0.306		1617.686	1492.630	1367.600
0.308		1620.189	1495.136	1370.109
0.310		1622.693	1497.641	1372.617
0.312		1625.196	1500.146	1375.125
0.314		1627.699	1502.652	1377.633
0.316		1630.202	1505.157	1380.141
0.318		1632.705	1507.662	1382.648
0.320		1635.208	1510.167	1385.156
0.322		1637.711	1512.672	1387.664
0.324		1640.214	1515.177	1390.171
0.326		1642.717	1517.682	1392.679
0.328		1645.219	1520.187	1395.186
0.330		1647.722	1522.691	1397.693
0.332		1650.224	1525.196	1400.201
0.334		1652.727	1527.700	1402.708
0.336		1655.229	1530.205	1405.215
0.338		1657.731	1532.709	1407.722
0.340		1660.233	1535.213	1410.228
0.342		1662.735	1537.717	1412.735

Table A.1 Continued.

0.344	1665.237	1540.221	1415.242
0.346	1667.739	1542.725	1417.748
0.348	1670.241	1545.229	1420.255
0.350	1672.743	1547.733	1422.761
0.352	1675.245	1550.237	1425.267
0.354	1677.746	1552.740	1427.773
0.356	1680.248	1555.244	1430.279
0.358	1682.749	1557.747	1432.785
0.360	1685.250	1560.251	1435.291
0.362	1687.752	1562.754	1437.797
0.364	1690.253	1565.257	1440.303
0.366	1692.754	1567.760	1442.808
0.368	1695.255	1570.263	1445.314
0.370	1697.756	1572.766	1447.819
0.372	1700.256	1575.269	1450.324
0.374	1702.757	1577.772	1452.830
0.376	1705.258	1580.274	1455.335
0.378	1707.758	1582.777	1457.840
0.380	1710.259	1585.279	1460.345
0.382	1712.871	1587.782	1462.850
0.384	1715.742	1590.284	1465.354
0.386	1718.926	1592.786	1467.859
0.388	1722.502	1595.288	1470.363
0.390	1726.578	1597.790	1472.868
0.392	1731.319	1600.292	1475.372
0.394	1736.982	1602.794	1477.876
0.396	1744.015	1605.295	1480.38
0.398	1753.289	1607.797	1482.885
0.400	1766.903	1610.299	1485.388
0.402		1612.800	1487.892
0.404		1615.301	1490.396
0.406		1617.803	1492.900
0.408		1620.304	1495.403
0.410		1622.805	1497.907
0.412		1625.306	1500.410
0.414		1627.807	1502.913
0.416		1630.308	1505.416
0.418		1632.808	1507.919
0.420		1635.309	1510.422
0.422		1637.809	1512.925
0.424		1640.310	1515.428
0.426		1642.810	1517.931
0.428		1645.310	1520.433
0.430		1647.811	1522.936

Table A.1 Continued.

0.432	1650.311	1525.438
0.434	1652.810	1527.940
0.436	1655.310	1530.442
0.438	1657.810	1532.944
0.440	1660.310	1535.446
0.442	1662.809	1537.948
0.444	1665.309	1540.450
0.446	1667.808	1542.951
0.448	1670.307	1545.453
0.450	1672.807	1547.954
0.452	1675.306	1550.456
0.454	1677.805	1552.957
0.456	1680.304	1555.458
0.458	1682.802	1557.959
0.460	1685.301	1560.460
0.462	1687.800	1562.960
0.464	1690.298	1565.461
0.466	1692.797	1567.962
0.468	1695.295	1570.462
0.470	1697.793	1572.963
0.472	1700.291	1575.463
0.474	1702.789	1577.963
0.476	1705.287	1580.463
0.478	1707.785	1582.963
0.480	1710.283	1585.463
0.482	1712.892	1587.962
0.484	1715.759	1590.462
0.486	1718.940	1592.962
0.488	1722.512	1595.461
0.490	1726.584	1597.960
0.492	1731.319	1600.459
0.494	1736.976	1602.958
0.496	1744.000	1605.457
0.498	1753.264	1607.956
0.500	1766.863	1610.455
0.502	--	1612.954
0.504		1615.452
0.506		1617.951
0.508		1620.449
0.510		1622.947
0.512		1625.445
0.514		1627.943
0.516		1630.441
0.518		1632.939

Table A.1 Continued.

0.520	1635.436
0.522	1637.934
0.524	1640.431
0.526	1642.929
0.528	1645.426
0.530	1647.923
0.532	1650.420
0.534	1652.917
0.536	1655.413
0.538	1657.910
0.540	1660.407
0.542	1662.903
0.544	1665.399
0.546	1667.895
0.548	1670.392
0.550	1672.887
0.552	1675.383
0.554	1677.879
0.556	1680.375
0.558	1682.870
0.560	1685.366
0.562	1687.861
0.564	1690.356
0.566	1692.851
0.568	1695.346
0.570	1697.841
0.572	1700.335
0.574	1702.830
0.576	1705.324
0.578	1707.819
0.580	1710.313
0.582	1712.919
0.584	1715.782
0.586	1718.958
0.588	1722.525
0.590	1726.591
0.592	1731.319
0.594	1736.968
0.596	1743.982
0.598	1753.232
0.600	1766.811

Table A.2 Optimum laser power P_o over length L and time t (data for Figure 7-3 and Figure 7-4).

L (mm)	P_o (W)	t (sec)	P_o (W)
0.02	0.9799	0.02	0.9799
0.04	0.9972	0.04	0.9972
0.06	0.9828	0.06	0.9828
0.08	0.9687	0.08	0.9687
0.10	0.9551	0.10	0.9551
0.12	0.9420	0.12	0.9420
0.14	0.9293	0.14	0.9293
0.16	0.9171	0.16	0.9171
0.18	0.9034	0.18	0.9034
0.20	0.8971	0.20	0.8971
0.22	0.8796	0.22	0.8796
0.24	0.8662	0.24	0.8662
0.26	0.8514	0.26	0.8514
0.28	0.8331	0.28	0.8331
0.30	0.8193	0.30	0.8193
0.32	0.8035	0.32	0.8035
0.34	0.7935	0.34	0.7935
0.36	0.7798	0.36	0.7798
0.38	0.7661	0.38	0.7661
0.40	0.7524	0.40	0.7524
0.42	0.7411	0.42	0.7411
0.44	0.7275	0.44	0.7275
0.46	0.7139	0.46	0.7139
0.48	0.6975	0.48	0.6975
0.50	0.6838	0.50	0.6838
0.60	0.6153	0.60	0.6153

Table A.3 Sum of squared errors S_e Vs. rod length L (data for Figure 7-5).

L	S_e
0.02	95.64
0.04	87.57
0.06	62.49
0.08	50.16
0.10	40.97
0.12	34.61
0.14	30.78
0.16	29.24
0.18	29.24
0.20	29.78
0.22	30.77
0.24	30.79
0.26	29.82
0.28	29.65
0.30	29.64
0.32	30.56
0.34	29.21
0.36	29.20
0.38	29.20
0.40	29.34
0.42	29.35
0.44	29.36
0.46	29.18
0.48	29.19
0.50	29.19
0.60	29.18

Table A.4 Program I: Source code for solving optimum laser power P_o, given a rod length L.

```
/*************************************************************************************************
This program calculates the optimum laser powers at different rod lengths. The user input a rod length, the
program generates corresponding laser power. Then input another rod length, run the program again to get
its laser power. Finally, the user can get the relationship, optimum laser power over rod length. The user
input L by setting L (at the sixth line of the program) to the desired value. Also the N (at the fourth line) is
reset to: N = 500*L for different L.
-------------------------------------------------------------------------------------------------*/

#include <math.h>
#include <iomanip.h>
#include <fstream.h>

const int  N=300, M=10, Iter_Num=4;
const long double L = 0.6, R = 0.04, tip_r = 0.015, hight=0.02, a = 0.002, Ea = 182004.0, Rgas = 8.314,
                  K0 = 237000.0, delta_t = 0.002, w = 0.01;

void SolveTrid (long double [N+1], long double [N+1], long double [N+1], long double [N+1],
                long double  [N+1]);
void TempDistr(long double, long double, long double, long double [N+1]);
void GetTgrowth(long double [M+1]);
long double growth (long double, long double, long double, long double);
void One_iterat (long double, long double &);

void main()
{
        long double P0[Iter_Num];
        P0[0]=1.48;       // initial guess for P_o

        for (int i=0; i<Iter_Num; i++)
        {
                One_iterat(P0[i], P0[i+1]);
                cout<<"After "<<i+1<<" iteration(s), P0 is: "<<setiosflags(ios::showpoint)
                        <<setprecision(20)<<P0[i+1]<<endl;
        }
}

/*-------------------------------------------------------------------------------------------------
This following subroutine is going through one cycle from step 1 to step 7 in section 5.6 of chapter five,
calculating P_o^k from P_o^{k-1}.
-------------------------------------------------------------------------------------------------*/
void One_iterat (long double P0, long double &new_P)
{
        long double T[M+1]={0}, Pdelta_T[M+1]={0}, X[M+1]={0}, XXtX[M+1],
                                T_Tgrow[M+1], Tgrow[M+1];
        long double delta_P0, temp1=0.0, XXt=0.0, S=0.0, Uk=2;

        delta_P0 = P0/1000;

        GetTgrowth(Tgrow);

        TempDistr(L, P0, w, T);
```

Table A.4 Continued.

```
/*-----------------------------------------------------------------------------------------------------------------*/
        TempDistr(L, P0+delta_P0, w, Pdelta_T);
        for (int n=0; n<M+1; n++)
                X[n]=(Pdelta_T[n]-T[n])/delta_P0;

        for (int i=0; i<M+1; i++)
                XXt=XXt+X[i]*X[i];
        for (i=0; i<M+1; i++)
                XXtX[i]=X[i]/XXt;

        for (i=0; i<M+1; i++){
                T_Tgrow[i] = T[i] - Tgrow[i];
                S = S + (T_Tgrow[i]*T_Tgrow[i]);
        }
        cout<<endl<<"The least square norm at this iteration is : "<<S<<endl;
        temp1=0.0;
        for (i=0; i<M+1; i++)
                temp1 = temp1 + XXtX[i]*T_Tgrow[i];
        new_P = P0 + temp1;
}

/*-----------------------------------------------------------------------------------------------------------------
The following subroutine calculates the temperature distribution on the whole surface of the rod.
-----------------------------------------------------------------------------------------------------------------*/
void TempDistr(long double L, long double P0, long double w, long double Temp[M+1])
{
        long double L1, c, h, Lumda;
        long double Ks = 0.0017,  absor = 1.0, f, kgas = 0.001, Kd=1.65, Nu = 0.36, pai = 3.1415926;
        long double x[N+1], r[N+1], O[N+1], x_half[N+1], sq_r_half[N+1], h_conv[N+1], Qin[N+1],
                b[N+1], slope[N+1];
        long double U[N+1]={0}, l[N+1]={0}, d[N+1]={0};

        long double y = R*R-tip_r*tip_r;
        L1 = L-hight;
        c = sqrt(y/hight);
        h = L/N;
        Lumda = 2*absor/(pai*w*w);

        cout<<endl;
        for (int i=0; i<N+1; i++)
        {
                x[i] = i*h;
                if (x[i]<=L1)
                        r[i] = R;
                else
                {
                        r[i] = c*sqrt(L+tip_r*tip_r/(c*c)-x[i]);
                        slope[i] = c*c/(2*r[i]);
                }
                h_conv[i] = Nu*kgas/(2*r[i]);
        }
```

Table A.4 Continued.

```
/*-------------------------------------------------------------------------------------------------------------------*/
        for (i=1; i<N+1; i++)
        {x_half[i] = i*h - h/2;
                if (x_half[i]<=L1)
                        sq_r_half[i] = R*R;
                else
                        sq_r_half[i] = c*sqrt(L+tip_r*tip_r/(c*c)-x_half[i])*c*sqrt(L+tip_r*tip_r/(c*c)
                                                                                -x_half[i]);
        }

        d[0] = 3*Ks/(8*Kd*r[0]*r[0]*r[0]) + 1/h;
        U[0] = -1/h;
        l[N] = -1/h;
        d[N] = h_conv[N]/(pai*Kd*tip_r*tip_r) + 1/h;

        for (i=1; i<N; i++)
        {
                l[i] = -(Kd*sq_r_half[i]/h)/h;
                d[i] = -r[i]*h_conv[i] + Kd*(sq_r_half[i] + sq_r_half[i+1])/(h*h);
                U[i] = -(Kd*sq_r_half[i+1]/h)/h;
        }

        for(i=1; i<N; i++)
        {
                if (x[i]<=L1)
                        Qin[i] = 0.0;
                else
                        Qin[i] = 2*P0*absor*(x[i]/sqrt(slope[i]*slope[i]+1))*
                                                                exp(-2*r[i]*r[i]/(w*w))/(pai*w*w);
        }

        b[0] = 0.0;
        b[N] = Lumda*P0*exp(-2*tip_r*tip_r/(w*w))/(pai*Kd*tip_r*tip_r);

        for (i=1; i<N; i++)
                b[i]=r[i]*Qin[i];

        SolveTrid (O, b, l, U, d);

        for (i=0; i<N+1; i++)
                O[i] = O[i] + 300;

        for (i=0; i<M+1; i++)
                Temp[i] = O[N+i-M];
}

/*-------------------------------------------------------------------------------------------------------------------
The following subroutine solves the linear system by Thomas Algorithm.
-------------------------------------------------------------------------------------------------------------------*/

void SolveTrid (long double O[N+1], long double b[N+1], long double l[N+1], long double U[N+1],
                long double d[N+1])
{
        long double b1[N+1], d1[N+1];
```

Table A.4 Continued.

```
/*-----------------------------------------------------------------------------------------------------------------*/
        d1[0]=d[0];
        b1[0]=b[0];
        for (int i=1; i<N+1; i++)
        {
                d1[i] = d[i] - l[i]*U[i-1]/d1[i-1];
                b1[i] = b[i] - l[i]*b1[i-1]/d1[i-1];
        }
        O[N] = b1[N]/d1[N];

        for (i=N-1; i>=0; i--)
                O[i] = (b1[i] - U[i]*O[i+1])/d1[i];
}

/*-----------------------------------------------------------------------------------------------------------------
The following subroutine calculates the required temperature distribution T_d^r on the parabolic portion of
the rod.
-----------------------------------------------------------------------------------------------------------------*/

void GetTgrowth(long double Td[M+1])
{
        long double L1, e, f, c, h;
        long double x[M+1], r[M+1], slope[M+1], x_new1[M+1], r_new1[M+1], x_new2[M+1],
                r_new2[M+1],  delta_x[M+1];

        long double y = R*R-tip_r*tip_r;

        L1 = L-hight;
        c = sqrt(y/hight);
        h = hight/M;

        cout<<endl;
        for (int i=0; i<M+1; i++)
        {
                x[i] = L1+i*h;

                r[i] = c*sqrt(L+tip_r*tip_r/(c*c)-x[i]);
                slope[i] = c*c/(2*r[i]);
        }

  delta_x[0] = 0;
  delta_x[M] = a;

  for ( int j=1; j<M; j++)
        {
                r_new1[j] = R;
                x_new1[j] = slope[j]*(R-r[j]) + x[j];
                if (x_new1[j] <= (L1+a) )
                        delta_x[j] = growth (r[j], x[j], r_new1[j], x_new1[j]);
                else break;
        }
```

Table A.4 Continued.

```
/*-----------------------------------------------------------------------------------------------------------------*/
        for (int k=j; k<M; k++)
        {
                e=(x[k]-slope[k]*r[k]-L-a-tip_r*tip_r/(c*c))/(c*c); f=sqrt(slope[k]*slope[k]-4*e);
                r_new2[k] = c*c*(f - slope[k])/2;
                x_new2[k] = slope[k]*(r_new2[k]-r[k]) + x[k];
                delta_x[k] = growth (r[k], x[k], r_new2[k], x_new2[k]);
        }

        for (int p=0; p<M+1; p++)
                Td[p] = - Ea / (Rgas * log(delta_x[p]/(K0*delta_t)));
        Td[0]=Td[1]-(Td[2]-Td[1])*(Td[2]-Td[1])/(Td[3]-Td[2]);
}
/*-----------------------------------------------------------------------------------------------------------------
The following subroutine calculates the growth of each grid point from current layer to the next layer.
-----------------------------------------------------------------------------------------------------------------*/

long double growth (long double a1, long double b1, long double a2, long double b2)
{
        long double d;
        d = (a2-a1)*(a2-a1) + (b2-b1)*(b2-b1);
        return sqrt (d);
}
```

Table A.5 Program II: source code for the calculation of $(T_d\hat{})_i$ and $(T_d)_i$ under optimum laser power P_o, $i = 1, \ldots, 10$.

```
/*****************************************************************************************
This program calculates the required temperature distribution and calculated temperature distribution (Td^)i
and (Td)i, on the parabolic portion of the rod at a certain rod length, under the optimum laser power.
Actually, program II is a part of program I. Program I uses a number of iterations to get final value of Po.
Program II only involves one iteration, and it shows the calculations step by step. The intermediate results
are displayed at each step.

So after running the program I, the user obtains Po at a certain rod length L, then input Po and L into
program II to obtain (Td^)i and (Td)i at that rod length, under that laser power. The user input Po by setting
P0 (at the seventh line of the program) to the desired value, and input L by setting L (at the sixth line of the
program) to the value. Also the N (at the fourth line) is reset to: N = 500*L for different L.
-----------------------------------------------------------------------------------------------------------------*/

#include <math.h>
#include <iomanip.h>
#include <fstream.h>

const int N=300, M=10;
const long double L = 0.6, R = 0.04, tip_r = 0.015, hight=0.02, a = 0.002, Ea = 182004.0, Rgas = 8.314,
                  K0 = 237000.0, delta_t = 0.002,  P0 =0.848450997052465, w=0.01, absor = 1.0,
                  kgas = 0.001, Nu = 0.36, pai = 3.1415926;

void SolveTrid (long double [N+1], long double [N+1], long double [N+1], long double [N+1],
                long double [N+1]);
```

Table A.5 Continued.

```
/*-------------------------------------------------------------------------------------------------------------------*/
void TempDistr(long double, long double, long double, long double [N+1]);
void GetTgrowth(long double [M+1]);
long double growth (long double, long double, long double, long double);
void print (long double []);

void main()
{
        long double T[M+1]={0}, Pdelta_T[M+1]={0}, X[M+1]={0}, XXtX[M+1], T_Tgrow[M+1],
                Tgrow[M+1];
        long double delta_P0, temp1=0.0, new_P=0.0, XXt=0.0;
        delta_P0=P0/1000;

        GetTgrowth(Tgrow);
        print(Tgrow);

        TempDistr(L, P0, w, T);
        print(T);

        TempDistr(L, P0+delta_P0, w, Pdelta_T);
        print(Pdelta_T);

        for (int n=0; n<M+1; n++)
                X[n]=(Pdelta_T[n]-T[n])/delta_P0;

        cout<<"X: "<<endl;
        print(X);

        for (int i=0; i<M+1; i++)
                XXt=XXt+X[i]*X[i];
        for (i=0; i<M+1; i++)
                XXtX[i]=X[i]/XXt;

        cout<<endl<<"The T_Tgrow is:  "<<endl;
        for (i=0; i<M+1; i++){
                T_Tgrow[i] = T[i] - Tgrow[i]; cout<<T_Tgrow[i]<<"  ";}
        temp1=0.0;
        for (i=0; i<M+1; i++)
                temp1 = temp1 + XXtX[i]*T_Tgrow[i];

        new_P = P0 + temp1;
        cout<<endl<<"New P is: "<<new_P<<endl;
}

void TempDistr(long double L, long double P0, long double w, long double Temp[M+1])
{
        long double L1, c, h, Lumda, f, Ks = 0.0017, Kd = 1.65;
        long double x[N+1], r[N+1], O[N+1], x_half[N+1], sq_r_half[N+1], h_conv[N+1], Qin[N+1],
                b[N+1], slope[N+1];
        long double l[N+1], U[N+1], d[N+1]={0};
        long double y = R*R-tip_r*tip_r;

        L1 = L-hight;
        c = sqrt(y/hight);
```

Table A.5 Continued.

```
/*-----------------------------------------------------------------------------------------------------------------------*/
        h = L/N;
        Lumda = 2*absor/(pai*w*w);

        cout<<endl;
        for (int i=0; i<N+1; i++)
        {
                x[i] = i*h;
                if (x[i]<=L1)
                        r[i] = R;
                else
                {
                        r[i] = c*sqrt(L+tip_r*tip_r/(c*c)-x[i]);
                        slope[i] = c*c/(2*r[i]);
                }
                h_conv[i] = Nu*kgas/(2*r[i]);
        }

        for (i=1; i<N+1; i++)
        {
                x_half[i] = i*h - h/2;
                if (x_half[i]<=L1)
                        sq_r_half[i] = R*R;
                else
                        sq_r_half[i] = c*sqrt(L+tip_r*tip_r/(c*c)-x_half[i])*c*sqrt(L+tip_r*tip_r/(c*c)
                                        -x_half[i]);
        }

        d[0] = 3*Ks/(8*Kd*r[0]*r[0]*r[0]) + 1/h;
        U[0] = -1/h;
        l[N] = -1/h;
        d[N] = h_conv[N]/(pai*Kd*tip_r*tip_r) + 1/h;

        for (i=1; i<N; i++)
        {
                l[i] = -(Kd*sq_r_half[i]/h)/h;
                d[i] = -r[i]*h_conv[i] + Kd*(sq_r_half[i] + sq_r_half[i+1])/(h*h);
                U[i] = -(Kd*sq_r_half[i+1]/h)/h;
        }

        for(i=1; i<N; i++)
        {
                if (x[i]<=L1)
                        Qin[i] = 0.0;
                else
                        Qin[i] = 2*P0*absor*(x[i]/sqrt(slope[i]*slope[i]+1))*
                                                                exp(-2*r[i]*r[i]/(w*w))/(pai*w*w);
        }

        b[0] = 0.0;
        b[N] = Lumda*P0*exp(-2*tip_r*tip_r/(w*w))/(pai*Kd*tip_r*tip_r);
```

Table A.5 Continued.

```
/*-----------------------------------------------------------------------------------------------------------------------*/
        for (i=1; i<N; i++)
                b[i]=r[i]*Qin[i];

        SolveTrid (O, b, l, U, d);

        for (i=0; i<N+1; i++)
                O[i] = O[i] + 300;

        for (i=0; i<M+1; i++)
                Temp[i] = O[N+i-M];
}

void SolveTrid (long double O[N+1], long double b[N+1], long double l[N+1], long double U[N+1],
                long double d[N+1])
{
        long double b1[N+1], d1[N+1];
        d1[0]=d[0];
        b1[0]=b[0];

        for (int i=1; i<N+1; i++)
        {
                d1[i] = d[i] - l[i]*U[i-1]/d1[i-1];
                b1[i] = b[i] - l[i]*b1[i-1]/d1[i-1];
        }
        O[N] = b1[N]/d1[N];

        for (i=N-1; i>=0; i--)
                O[i] = (b1[i] - U[i]*O[i+1])/d1[i];

}

void GetTgrowth(long double Td[M+1])
{
        long double L1, e, f, c, h;
        long double x[M+1], r[M+1], slope[M+1], x_new1[M+1], r_new1[M+1], x_new2[M+1],
                r_new2[M+1], delta_x[M+1];

        long double y = R*R-tip_r*tip_r;

        L1 = L-hight;
        c = sqrt(y/hight);
        h = hight/M;

        cout<<endl;
        for (int i=0; i<M+1; i++)
        {
                x[i] = L1+i*h;

                r[i] = c*sqrt(L+tip_r*tip_r/(c*c)-x[i]);
                slope[i] = c*c/(2*r[i]);
        }
```

Table A.5 Continued.

```
/*-------------------------------------------------------------------------------------------------------------------------------------------------*/
  delta_x[0] = 0;
  delta_x[M] = a;
  for ( int j=1; j<M; j++)
        {
              r_new1[j] = R;
              x_new1[j] = slope[j]*(R-r[j]) + x[j];
              if (x_new1[j] <= (L1+a) )
                    delta_x[j] = growth (r[j], x[j], r_new1[j], x_new1[j]);
              else break;
        }

        for (int k=j; k<M; k++)
        {
              e=(x[k]-slope[k]*r[k]-L-a-tip_r*tip_r/(c*c))/(c*c); f=sqrt(slope[k]*slope[k]-4*e);
              r_new2[k] = c*c*(f - slope[k])/2;
              x_new2[k] = slope[k]*(r_new2[k]-r[k]) + x[k];
              delta_x[k] = growth (r[k], x[k], r_new2[k], x_new2[k]);
        }

        for (int p=0; p<M+1; p++)
              Td[p] = - Ea / (Rgas * log(delta_x[p]/(K0*delta_t)));

        Td[0]=Td[1]-(Td[2]-Td[1])*(Td[2]-Td[1])/(Td[3]-Td[2]);
}

long double growth (long double a1, long double b1, long double a2, long double b2)
{
        long double d;
        d = (a2-a1)*(a2-a1) + (b2-b1)*(b2-b1);
        return sqrt (d);
}

void print (long double B[M+1])
{
        char z;
        for (int i=0; i<M+1; i++)
              cout<<setiosflags(ios::showpoint)<<setprecision(20)<<B[i]<<"  "<<endl;
        cout<<endl<<"enter a leter: ";
        cin>>z;
}
```

Table A.6 Program III: source code for calculating the temperature distribution on the whole surface of the rod, given P_o and L.

```
/*****************************************************************************************
This program calculates the temperature distribution (T_d)_i, i = 1, ..., N, on the whole surface of the rod at a
certain rod length and laser power. This program also shows the calculations step by step. The
intermediate results are displayed at each step. The user input P_o by setting P0 (at the seventh line of the
program) to the desired value, and input L by setting L (at the sixth line of the program) to the value. Also
the N (at the fourth line) is reset to: N = 500*L for different L.
-----------------------------------------------------------------------------------------------*/

#include <math.h>
#include <iomanip.h>
#include <fstream.h>

const int N=130;
const long double L = 0.26, R = 0.04, tip_r = 0.015, hight=0.02, a = 0.002, Ea = 182004.0, Rgas = 8.314,
                  K0 = 237000.0, delta_t = 0.002, P0 = 0.848450997052465, w=0.01, absor = 1.0,
                  kgas = 0.001, Nu = 0.36, pai = 3.1415926;
void SolveTrid (long double [N+1], long double [N+1], long double [N+1], long double [N+1],
                long double [N+1]);
void main()
{
        long double L1, c, h, Lumda, f, Ks = 0.0017, Kd = 1.65;
        long double x[N+1], r[N+1], O[N+1]={0}, x_half[N+1], sq_r_half[N+1], h_conv[N+1],
                    Qin[N+1], b[N+1], slope[N+1];
        long double l[N+1], U[N+1], d[N+1]={0};
        long double y = R*R-tip_r*tip_r;
        char z;

        L1 = L-hight;
        c = sqrt(y/hight);
        h = L/N;
        Lumda = 2*absor/(pai*w*w);

        cout<<endl;
        for (int i=0; i<N+1; i++)
        {
                x[i] = i*h;
                if (x[i]<=L1)
                        r[i] = R;
                else
                {
                        r[i] = c*sqrt(L+tip_r*tip_r/(c*c)-x[i]);
                        slope[i] = c*c/(2*r[i]);
                }
                h_conv[i] = Nu*kgas/(2*r[i]);
        }

        cout<<endl<<" x[i] "<<"   r[i] "<<"      slope[i] "<<" h_conv[i] "<<endl;
        for (int j=0; j<N+1; j++)
        {
        cout<<setiosflags(ios::showpoint)<<x[j]<<" "<<r[j]<<" "<<slope[j]<<" "<<h_conv[j]<<endl;
        }
```

Table A.6 Continued.

```
/*-------------------------------------------------------------------------------------------------------------------------*/
        cout<<endl<<"Please enter a letter to continue: ";
        cin>>z;

        for (i=1; i<N+1; i++)
        {
                x_half[i] = i*h - h/2;
                if (x_half[i]<=L1)
                        sq_r_half[i] = R*R;
                else
                        sq_r_half[i] = c*c*(L+tip_r*tip_r/(c*c)-x_half[i]);
        }

        cout<<endl<<"x_half[i]  "<<"square of r_half[i]"<<endl;

        for (int m=1; m<N+1; m++)
        {
                cout<<x_half[m]<<"   "<<sq_r_half[m]<<"   "<<endl;
        }
        cout<<endl<<"Please enter a letter to continue: ";
        cin>>z;

        d[0] = 3*Ks/(8*Kd*r[0]*r[0]*r[0]) + 1/h;
        U[0] = -1/h;
        l[N] = -1/h;
        d[N] = h_conv[N]/(pai*Kd*tip_r*tip_r) + 1/h;

        for (i=1; i<N; i++)
        {
                l[i] = -(Kd*sq_r_half[i]/h)/h;
                d[i] = -r[i]*h_conv[i] + Kd*(sq_r_half[i] + sq_r_half[i+1])/(h*h);
                U[i] = -(Kd*sq_r_half[i+1]/h)/h;
        }

        for(i=1; i<N; i++)
        {
                if (x[i]<=L1)
                        Qin[i] = 0.0;
                else
                        Qin[i] = Lumda*P0*exp(-2*r[i]*r[i]/(w*w))*(x[i]*slope[i]/sqrt(slope[i]*
                                                                                slope[i]+1));
        }

        b[0] = 0.0;
        b[N] = Lumda*P0*exp(-2*tip_r*tip_r/(w*w))/(pai*Kd*tip_r*tip_r);

        for (i=1; i<N; i++)
                b[i]=r[i]*Qin[i];
        cout<<endl<<"The inhomogenious terms b[i]: "<<endl;

        for (i=0; i<N+1; i++)
        {
                cout<<b[i]<<"  ";
        }
```

Table A.6 Continued.

```
/*-------------------------------------------------------------------------------------------------------------------------*/
        cout<<endl<<endl;

        SolveTrid (O, b, l, U, d);
        cout<<"The temperature distribution on the surface of the rod: "<<endl;

        for (i=0; i<N+1; i++)
        {
                cout<<O[i]+300<<"  ";
                file<<setiosflags(ios::showpoint)<<setprecision(20)<<O[i]+300<<endl;
        }
        cout<<endl;
        }

void SolveTrid (long double O[N+1], long double b[N+1], long double l[N+1], long double U[N+1],
                long double d[N+1])
{
        long double b1[N+1], d1[N+1];
        d1[0]=d[0];
        b1[0]=b[0];

        for (int i=1; i<N+1; i++)
        {
                d1[i] = d[i] - l[i]*U[i-1]/d1[i-1];
                b1[i] = b[i] - l[i]*b1[i-1]/d1[i-1];
        }
        O[N] = b1[N]/d1[N];

        for (i=N-1; i>=0; i--)
                O[i] = (b1[i] - U[i]*O[i+1])/d1[i];

}
```

REFERENCES

1. Bauerle, D. "Laser induced Chemical Vapor Deposition," *Springer Series in ChemicalPhysics,* Springer Verlag Edition, 1984.

2. Wallenberger, F., and P. Nordine. "Strong, Pure, and Uniform Carbon Fibers Obtained Directly from the Vapor Phase," *Science*, v. 260, 1993, pp.66-68.

3. Baum, T., and P. Comita. "Laser-induced Chemical Vapor Deposition of Metals for Microelectronics Technology," *Thin Solid Films,* v. 218, 1992, pp.80-94.

4. Maxwell, J., Pegna, J., "Experimental Developments Towards Multi-Material Micron Scale Rapid Prototyping," *ASME Design Automation Conference*, Boston, MA, Dec.,1995.

5. Marcus, H. L., and K. Jakubenas. "Selective Area Laser Deposition from Titanium Tetrachloride," *SFF Symposium*, 1995, pp.381-388.

6. Westberg, H., Boman, M., "Truly Three Dimensional Structures Microfabricated by Laser Chemical Processing," *IEEE, 91CH2817-5,* 1991, pp.516-519.

7. Hanabusa, M., Kiduchi, H., Iwanga, T., and Sugai, K., "IR Laser Photo-Assisted Deposition of Silicon Films," *Springer Series in Chemical Physics* 39, Laser Processing and Diagnostics, pp.197-204, 1984.

8. Pegna, J., Messia, D., Lee, W.H. "Trussed Structures: Freeform Fabrication without the Layer," *Proc. Solid Freeform Fabrication Symposium*. Austin Texas, Aug., 1997.

9. Messia, D., Pegna, J., Lee, W.H., "Layered Micro-Wall Structures from Gas Phase," *Proc. Solid Freeform Fabrication Symposium*. Austin Texas, Aug. 1997.

10. Maxwell, J., K. Williams, M. Boman, and K. Larsson. "Freeform Fabrication of Functional Microsolenoids, Electromagnets and Helical Springs Using High Pressure Laser Chemical Vapor Deposition," *IEEE*, 1999, pp.232-237.

11. Wallenberger, F.T. , Nordine, P.C., "Inorganic Fibers and Microstructures By Laser Assisted Chemical Vapor Deposition," *Material Technology* 8(9/10), 1983, pp.198-202.

12. Boman, M., Westverg, H., Johansson, S, Schwitz, J., "Helical Microstructures Grown By Laser Assisted Chemical Vapor Deposition," *Micro Electro Mechanical Systems*, 1992.

13. Cline, H. E., and T. R. Anthony, *J. Appl. Phys.* v48, 3895, 1977.

14. Calder, D. and R. Sue, *J. Appl. Phys.* v53, 1982, pp7545.

15. El-Adawi, M. K. and E. F. Elshehawey, *J. Appl. Phys.* v60, 1986, pp2250.

16. Brugger, K., "Exact Solution for the Temperature Rise in a Laser-Heated Slab," *J. Appl. Phys.*, v43, No. 2, 1972, pp577-583.

17. Bauerle, D., Piglmayer, K., "On the Reaction Kinetics in Laser-induced Pyrolytic Chemical Processing," *J. Appl. Phys. A*, v50, No. 2, 1990, pp385-396.

18. Bauerle, D. "Laser Processing and Diagnostics," *Springer Series in Chemical Physics*, Springer Verlag Edition, 1984, pp166.

19. Arnold, N. and D. Bauerle. "Simulation of Growth in Pyrolytic Laser-CVD of Microstructures – II. Two-dimensional Approach," *Microelectron. Eng.*, v20, pp. 43-54, 1993.

20. Arnold, N., R. Kullmer and D. Bauerle. "Simulation of Growth in Pyrolytic Laser-CVD of Microstructures – I. One-dimensional Approach," *Microelectron. Eng.*, v20, pp. 31-41, 1993.

21. Allen, S. D. and J. A. Goldstone, J. P. Stone, and R. Y. Jan. *J. Appl. Phys.* v59, pp. 1653, 1986.

22. Tonnear, D. and G. Auvert, "Computer Simulation of Laser Induced Temperatures for the Laser Direct Writing Techniques, Laser and Particle-Beam Chemical Processing for Microelectronics," *Mater. Res. Symp. Proc.*, v101, pp. 131-136, 1988.

23. Leon, B., M. Perez-Amor and C. Garrido, "A Model to Calculate the Temperature Induced by a Laser," *J. Appl. Phys.* v63, pp. 1133-1140, 1991.

24. Weissman, E. M. and M. B. Hsu, "A Finite Element Model of Multi-Layered Laser Sintered Parts," *Solid Freeform Fabrication Symposium*, pp. 86-94, 1991.

25. Zeiri, Y., Atzmony, U., and Bloch, J., "Monte Carlo Simulation of Laser-induced Chemical Vapor Deposition," *J. Appl. Phys.* v69, pp. 4110-5, 1991.

26. Maxwell, J., "Three-dimensional Laser Induced Pyrolytic Modeling, Growth Rate Control, and Application to Micro-Scale Prototyping," Ph.D. thesis, Rensselaer

Polytechnical Institute, Troy, New York, 1996.

27. Dai, W., R. Nassar, C. Zhang, and S. Shabanian, "A Numerical Model for Simulating Axisymmetric Rod Growth in 3D-LCVD," *Numerical Heat Transfer*, Part A, v36, pp. 251-262, 1999.

28. Gao, F., "Three-dimensional Laser Induced Pyrolytic Modeling, Growth Rate Control, and Application to Micro-Scale Prototyping," Ph.D. thesis, Louisiana Tech University, Ruston, 2000.

29. Zhang, C., "Mathematical Modeling for Fabricating a Microstructure with a Pre-specified Geometry Using Laser Chemical Vapor Deposition," Ph.D. thesis, Louisiana Tech University, Ruston, 2001.

30. Hecht, E., "Physics," *Brooks/cole Publishing Company*, 2nd Edition, 1997.

31. Churchill, S. W., Chu, H. H. S., "Correlating Equations for Laminar and Turbulent Free Convection from a Horizontal Cylinder," *Int. J. Heat Mass Transfer*, v18, pp. 1049, 1975.

32. Carslaw, H. S. and J. C. Jaeger, "Conduction of Heat in Solids," 2nd ed., pp. 246, Clarendon Press, Oxford, 1959.

33. Beck, V. and Blackwell, B., "Inverse Heat Conduction," *Wiley*, New York, 1985.

34. Alifanov, O. M., "An Introduction to the Theory of Inverse Heat Transfer Problems," *Mashinestroenie Publishing Agency*, Moscow, 1991.

35. Langford, D., *Q. Appl. Math.*, v24, pp. 315-342, 1967.

36. Powell, W. B. and Price, T. W., *ISA Trans.*, v3, pp. 246-254, 1964.

37. Blackwell, B., Num. Heat Transfer, v4, pp. 229-239, 1981.

38. Hensel, E., "Inverse Theory and Applications for Engineers," *Prentice Hall*, Englewood Cliffs, N.J., 1991.

39. Tikhonov, A. N., and Arsenin, Y., "Solutions of Ill-Posed Problems," *Winston & Sons*, Washington, DC, 1977.

40. Scott, E. and Beck, J.V., *ASME paper*, No. 85-WA/HT-43, 1985.

41. Busby, H. R. and Trujillo, D. M., *int. J. Num. Meth. Eng.* v21, 1985, pp 349-59.

42. Beck, J.V. and Arnold, K. J., "Parameter Estimation in Engineering and Science," *Wiley*, New York, 1977.

43. Ozisik, M. N., "Heat Conduction," *Dover*, New York, 1993. pp595-7.

44. Nassar, R., Dai, W., and Chen, Q., "An Axisymmetric Numerical Model for Simulating Kinetically-limited Growth of a Cylindrical Rod in 3D-LCVD," to be published.

45. Hoffman, J. D., "Numerical Methods for Engineers and Scientists", *McGraw-Hill*, New York, 1992.

46. Doppelbauer, J. and Bauerle, D., "Kinetics of Laser-Induced Pyrolytic Chemical Processes and the Problem of Temperature Measurements", *Angewandte Physik*, Johannes-Kepler-Universitat Linz, Austria, 1988, pp 277-297.

47. Ozisik, M. N., "Boundary Value Problems of Heat Conduction," *Dove*, New York, 1989.

48. Huang, C. H. and Ozisik, M. N., *Num. Heat Transfer*, Part A. v21, 101-116, 1992.

49. Farebrother, R. W., "Linear Least Squares Computations," *Marcel Dekker*, New York, 1988.

50. Beck, F. S., "The Solution of Linear Equations of Conjugate Gradient Method," *Mathematical Method for Digital Computer*, A.Ralston and H. S. Wilf (Eds), Chapter four, *Wiley*, New York, 1960.

51. Pierson, H. O., "Handbook of Chemical Vapor Deposition-Principles, Technology, and Applications," *Noyes Publications*, 1992.

52. Incropera F. P., and Dewitt, D. P., "Fundamentals of Heat and Mass Transfer," 2nd Edition, *John Wiley & Sons*, 1985.

53. Kar, A. and Mazumder, J., "Three-dimensional Transient Thermal Analysis for Laser Chemical Vapor Deposition on Uniformly Moving Finite Slab," *J. Appl. Phys.* v65, No. 8, 1989.